Kinetic Simulations of Spacecraft Charging and Plasma Interactions in the Solar Wind

Hyunju Jeong

Dissertation submitted to the Faculty of the
Virginia Polytechnic Institute and State University
in partial fulfillment of the requirements for the degree of

Doctor of Philosophy
in
Aerospace Engineering

Joseph J. Wang, Chair
Christopher Roy
Adrian Sandu
Wayne A. Scales
Danesh K. Tafti

September 1^{th}, 2008
Blacksburg, Virginia

Keywords: Particle-In-Cell, Charging, Sheath, Plasma flow

Kinetic Simulations of Spacecraft Charging and Plasma Interactions in the Solar Wind

Hyunju Jeong

(ABSTRACT)

Analytical and numerical studies are carried out to investigate spacecraft charging and plasma interactions in the solar wind. The physics of spacecraft charging in solar wind is determined by the mesothermal flow and the photoelectron sheath. In order to properly resolve both plasma flow and the photoelectron sheath, a 3-D full particle PIC model is applied. In this model, all plasma species (ambient ions and electrons, and photoelectrons) are modeled as macro-particles so the detailed dynamics of each species can be resolved around a charged spacecraft. In order to correctly resolve the mesothermal velocity ratio, PIC simulations are carried out using the real ion to electron mass ratio. A charging model based on the capacitance matrix method is integrated into the PIC model so the floating potential can be calculated self-consistently with the PIC code from charges deposited on the surface.

We first investigate the photoelectron sheath in the solar wind. Previous analytical studies of monotonic and non-monotonic sheath profiles in stationary electrons have suggested that there can exist two solutions of the sheath profiles when photoelectron emissions are significant. We extend the previous analytical study to include the effects of drifting electrons. Full particle PIC simulations suggest that the non-monotonic sheath profile is the stable solution under solar wind conditions. We found that the current balance calculation is not an accurate method to predict the floating potential when photoelectron emissions are significant.

We next apply the simulation model to study spacecraft charging under various solar wind conditions. Due to photoelectron emissions, spacecraft charging is typically not a serious problem. The floating potential is $\sim 2.5V$ under the mean solar wind condition. We also investigate the plasma interactions of a multi-body system consisting of a large platform

($6\lambda_d \times 6\lambda_d$) and a small free flyer ($1.2\lambda_d \times 1.2\lambda_d \times 0.6\lambda_d$) in the absence of photoelectron emissions where we set a free flyer at $2\lambda_d$ behind the platform in the wake. For the particular system studied in this dissertation, the simulation shows that wake charging is not severe under both the mean solar wind condition and severe magnetosheath charging condition.

Acknowledgments

First, I want to thank Jesus Christ who gave me strength and encouragement to complete this dissertation.

I would like to thank my advisor Dr. Joseph Wang for his guidance and direction for the last 5 years. Without his direction and support, I would not have completed this dissertation.

I would like to express my deep gratitude to my committee members. I would like to thank Dr. Wayne A Scales for valuable directions and comments on my dissertation. I want to express my gratitude to Dr. Danesh Tafti for his encouragement and help. I want to thank Dr. Adrian Sandu for his encouragement and support. I would like to thank Dr. Christopher Roy for his comments and directions which helped to improve so much.

I would like to thank Dr. Cho of Kyushu Institute of Technology (KIT) for many discussions on spacecraft charging and the capacitance matrix approach. I would like to express my deep gratitude to my advisor for master thesis, Prof. Dongsu Ryu and my committee, Prof. Kwangtae Kim in Chungnam National University.

I would like to thank my fellow graduate students of Dr. Wang's research group: Pu Wang, Ouliang Chang, Sam Sawyer, and Ning Ding, . I would like to express my gratitude to Steve, computer administrator for his efforts to maintain our computing system. I want to express sincere appreciation to my Korea colleagues: Namheui Jeong, Seongsub Lee, Hyunsun Do, Deawon Kim, and Jinwon Park. Special thanks should go to my good friends. First, I would to express my deep gratitude to my friends: Hwajeong Lee, Heesook Lee, Kyoungna Kim, Juhyun Lee, Hikyung Kim, and Jihyun Park for their encouragement and prayer. Many

credits should go to my friend in Korea: Hyesook Lee, Inok Song, hyunsuk Jeong, and Kyungsun Park for their friendship.
I would like to express especial thanks to my parents and my sisters. I am so thankful for their love and patience. I realized that the language of human beings is so limited to express our heart.

This research is supported partially by contracts from National Institute of Aerospace (NIA) and NASA Jet Propulsion Laboratory (JPL).

Contents

List of Figures

List of Tables

Chapter 1

Introduction

Spacecraft charging is an important issue in spacecraft design and operation. The charging effects have been attributed to operational anomalies, component failures, and even total failure of a spacecraft [83, 77, 58]. The objective of this study is to develop a fully kinetic simulation model to study spacecraft charging and plasma interaction in the solar wind.

There have been extensive studies in spacecraft charing. In many aspects, the physics underlying spacecraft charging is similar to that of an electrostatic probe immersed in plasma. The work of Langmuir [49] provides the fundamental knowledge and basic understanding of current collection by an electrostatic probe. Some early studies relevant to probe theory and spacecraft charging include the following: Berstein and Rabinowitz [3] studied particle trajectories around a probe by using the time-dependent Vlasov's equation and Poisson's equation in self-consistent manners; Beard and Johne [1] discussed the effects of electric fields generated by a satellite at the earth's magnetic fields and investigated the effect of emitting charged particles on a spacecraft in the ionosphere; Davis and Harries [12] studied the shielding of a moving sphere in the ionosphere; Whipple [97] investigated the charging effects by solving the Poisson-Vlasov equations. In recent years, numerical modeling has been increasingly used in predicting spacecraft charging and investigating spacecraft-plasma interactions. For instance, the NASA Charging Analyzer Program (NASCAP) [52, 53, 54, 55, 56] has been

used extensively in US and Spacecraft Plasma Interaction System (SPIS) [33, 79, 34, 17], used in Europe. A review of spacecraft charging can be found in Garrett [19] and Whipple [95].

However, most studies on charging have focused on geosynchronous (GEO) orbit. In GEO, the ambient plasma relative to spacecraft is stationary and the plasma Debye length is much larger than the spacecraft dimension. Hence, the interaction in GEO may be characterized as "thick sheath" in stationary plasma. This study focuses on spacecraft charging and plasma interactions in the solar wind. The solar wind is a tenuous, high speed plasma which flows radially outward from the sun. Its parameters may undergo substantial variation but mean observed values of plasma parameters at 1 AU are given by the values shown in Table 1.1 [24]. The solar wind plasma flow is mesothermal, $v_{ti} << V_{sw} << v_{te}$, where v_{ti} and v_{te} are the solar wind ion and electron thermal velocity, respectively. The plasma Debye length in the solar wind is smaller than or comparable with typical spacecraft dimension. Hence, in contrast to GEO, the spacecraft-plasma interaction in solar wind may be characterized as "thin sheath" in a flowing plasma. Additionally, the photoelectrons may dominate the plasma sheath under sunlight. A number of studies have combined surface charging calculations with photoelectron sheath calculations for conditions relevant to spacecraft charging in solar wind. For instance, Fu developed an analytical model for a photoelectron emitting planar surface in stationary electrons and showed that there can exist two types of steady state solutions of the potential profile in the photoelectron sheath: the monotonic profile and non-monotonic profile. It has been suggested that the non-monotonic profile is a more stable solution if the photoelectrons are significant [18]. Nitter et al. further developed a numerical solution of the photoelectron sheath [69]. The non-monotonic sheath has also been studied recently for surfaces with active plasma emissions. For instance, Wang and Lai [91] developed a full particle PIC model of the plasma sheath for an ion beam emitting surface and Marrese et al. [57] developed a full particle PIC model of the plasma sheath for an electron emitting surface. In both studies, particle simulations showed that the current emission will lead to a non-monotonic potential profile and even a virtual anode or cathode

if the emitted current far exceeds the ambient plasma current. A number of studies have also investigated the interactions between mesothermal plasma flow and a large object under "thin sheath" limit (see Wang and Hasting [89, 90] and references therein). For example, Wang and Hasting [89, 90] developed a PIC model to study the plasma flow around a large thin negatively charged platform in ionosphere. Wang and Garrett [22] further developed a PIC model to simulate solar wind plasma flow over a positively charged solar sail. However, in both studies, the electrons are modeled as an isothermal fluid and the object charging potential in the simulation is not calculated self-consistently.

Table 1.1: Parameters corresponding to typical solar wind condition.

Parameter	Electron	Ion
Density (ρ), cm^{-3}	8.7	8.7
Temperature (T), eV	12	10
Drifting Velocity (v_d), km/s	468	468
Thermal Velocity (v_t), km/s	2.05×10^3	43.8
Debye length (λ_d), m	8.7	7.97
Gyro frequency (Ω), rad/s	1.8×10^3	0.96
Plasma frequency (ω), rad/s	1.66×10^5	3.9×10^3
gyroradius ($r = v/\Omega$),km	1.1	489

Table 1.2: Various solar wind conditions used in charging simulations.

	$n_e, n_i(cm^{-3})$	$V_{sw}(km/s)$	$T_e(eV)$	$T_i(eV)$
Solar wind mean flux density	8.7	468	12	10
Solar wind 5% flux density	3	500	12	10
Solar wind 95% flux density	100	900	12	50
Magnetosheath	100	900	1000	1000

1.1 Approach

In this dissertation, we first investigate the photoelectron sheath. We then study plasma flow effects and spacecraft charging.

1.1.1 Analytical Approach

When a spacecraft is immersed in solar wind plasma and is exposed to the solar radiation, the dominating current sources are the solar wind protons and electrons, and photoelectrons. As the photoelectron current is typically much larger than that of the solar wind protons and electrons, the sunlit surface of a spacecraft is typically charged positively with respect to ambient solar wind plasma. We shall refer a plasma sheath dominated by the photoelectrons as the photoelectron sheath. An analytical approach is first developed to predict surface floating potential and the photoelectron sheath profile under solar wind conditions.In most analytical studies, the floating potential is calculated using the 1-D current balance calculation where the currents are obtained by assuming a monotonic sheath profile. However, it is well known that the potential profile near an electron-emitting plate can become non-monotonic if the photoelectron emissions are sufficiently large. The photoelectron sheath has been studied extensively (see, for example, Ref. [84, 28, 18, 69, 98, 85] and references therein). Fu [28, 18] developed a detail analytical approach to calculate the non-monotonic potential profile in the photoelectron sheath for a plate immersed in a stationary plasma. In this dissertation, we extend the analytical approach developed by Fu [28, 18] and Nitter [69] to include the effects of drifting electrons.

1.1.2 Numerical Approach

The basic characteristics of solar wind plasma around a spacecraft is similar to that of unmagnetized, collisionless, mesothermal plasma flow around an object. Previously, Wang and

Hastings [89, 90] and Wang and Garrett [22] developed a particle simulation model to study mesothermal plasma flow around a large object. In those studies, the kinetic behavior of electrons were ignored. Wang and Lai [91] and Marrese et al. [57] further developed full particle models to study the sheath near an electron emitting surface. The research presented in this dissertation extends the previous work of Wang and Hastings [89, 90], Wang and Garrett [22], and Wang and Lai [91] to model the photoelectron sheath and charging under solar wind conditions. In this dissertation, a full particle simulation model is developed where the model resolves electron kinetic behavior. This model can be used to model plasma interactions for both negatively and positively charged objects. The PIC model is further integrated with a charging model based on a capacitance matrix method [7, 8] so the floating potential can be obtained directly in PIC simulations from charges deposited on an object surface.

In the PIC model presented here, all plasma species (ambient ions and electrons, and photoelectrons) are modeled as macro-particles so the detailed dynamics of each species can be resolved. Full PIC models require sophisticated schemes for the loading and injection of particles at the simulation domain boundaries because any inaccuracy in handling the transient of fast moving electrons at the simulation domain can quickly result in numerical problems and/or wrong results. In this work, the particle injection scheme from [4, 5, 11] is applied to determine the particle injection number and corresponding velocities at all domain boundaries. In order to maintain the correct velocity ratio of mesothermal flow ($v_{ti} \ll v_d \ll v_{te}$), PIC simulations were performed using the real ion to electron mass ratio. The potential on a spacecraft was calculated directly using the deposited charges on each node obtained from PIC simulations. The charge re-distribution on the conductive materials was calculated using the classical capacitance matrix technique [7, 8, 2, 32]. A numerical model is applied to a spacecraft charging under various solar wind conditions including the mean solar wind flux, 5% solar wind flux, 95% solar wind flux, and severe magnetosheath charging conditions.

Chapter 2

Analytical Approach

2.1 Introduction

The surface floating potential in space is determined by the current balance condition:

$$I_{net}(\phi_0) = I_e(\phi_0) - I_i(\phi_0) - I_{se}(\phi_0) - I_{si}(\phi_0) - I_b(\phi_0) - I_{ph}(\phi_0) = 0 \tag{2.1}$$

where ϕ_0 is the surface floating potential, I_{net}, the total current, I_e, the electron current, I_i, the ion current, I_{se}, the secondary electron current due to I_e, I_{si}, the secondary electron current due to I_i, I_b, the backscattered electron current due to I_e, I_{ph}, the photoelectron current. Fig. 2.1 illustrates surface charging in eclipse and under sunlight. In this work, we shall only consider the ambient electron current, ambient ion current, and photoelectron current in the above equation.

The essence of the problem is to determine the current as a function of the surface potential. In order to calculate the current on the surface, one first needs to solve for the plasma sheath surrounding the surface. When the photoelectrons are present, the potential profile in the sheath can be significantly more complex than the regular plasma sheath. We typically refer the sheath dominated by the photoelectrons as the photoelectron sheath. There can exist two types of steady state solutions for the photoelectron sheath [18]. One is the monotonic

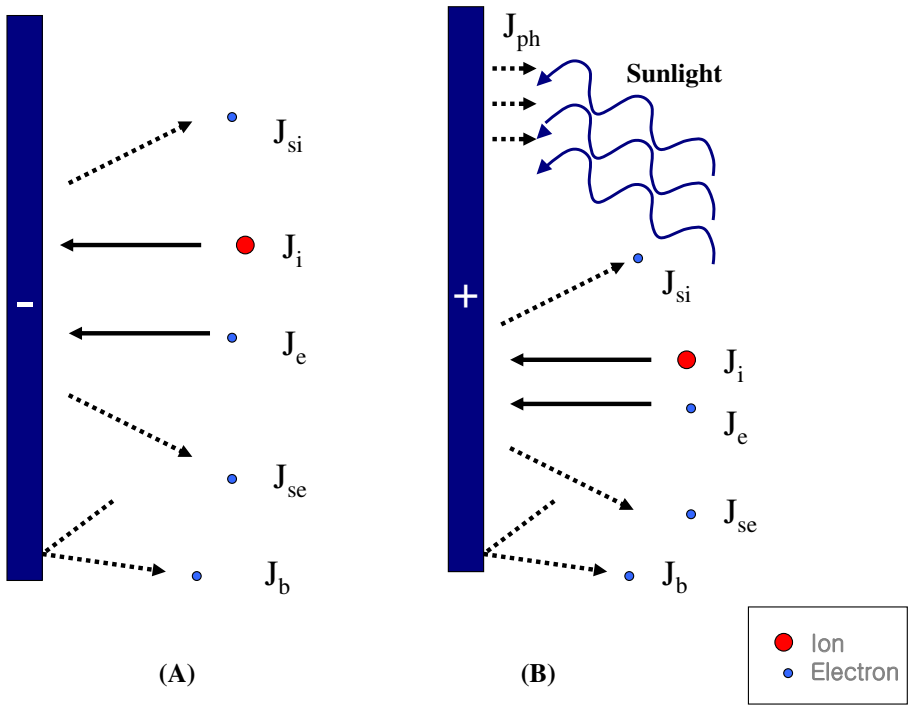

Figure 2.1: Schematic for charging effect (A) in eclipse and (B) under sunlight.

sheath profile where the potential changes from the surface potential to ambient potential monotonically. The other is the non-monotonic sheath profile where the potential decreases to a negative minimum potential before increasing to the ambient potential. It was suggested that the non-monotonic sheath profile is the more stable solution when the photoelectron density dominates that of the ambient plasma [18]. Fig. 2.2 illustrates the regular plasma sheath and photoelectron sheath around a charged plate. In this chapter, we apply two methods to calculate the floating potential. In Section 2.2, we assume a monotonic potential profile for the plasma sheath and apply the 1-D current balance calculation using current obtained from the monotonic potential profile. As the non-monotonic sheath profile is expected when photoelectrons dominate the ambient plasma, the results presented in Section 2.2 are not expected to represent the real physics. These results are only for the purpose of comparison. In Section 2.3, we introduce the photoelectron sheath theory. The analytical

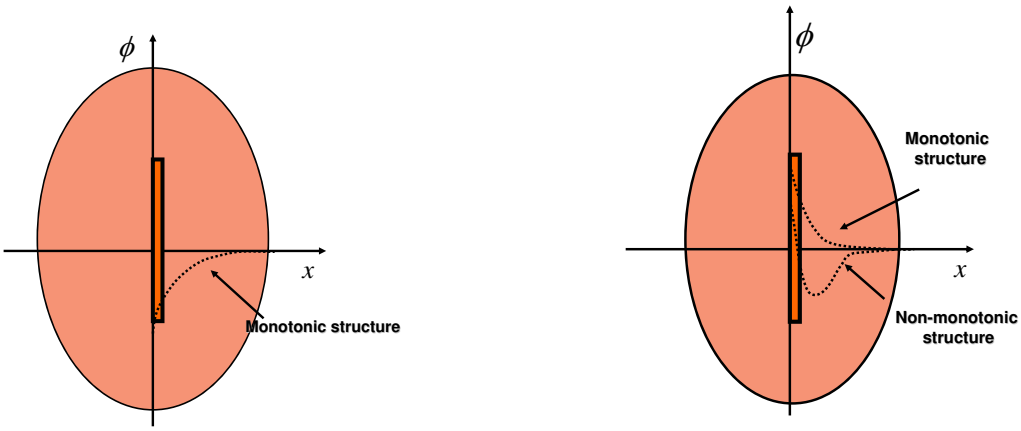

Figure 2.2: Schematic for regular plasma sheath (left) and photoelectron sheath (right) around a charged object.

approach presented here follows the previous studies by Fu [18] and Nitter [69]. The basic procedure of this approach is to first obtain the surface potential and minimum potential using boundary conditions and then solve the Poisson's equation.

In the previous studies of Fu [18] and Nitter [69], the electron drifting effect was ignored. In this chapter, we include the drifting electrons in solving the Poisson's equation. As the solar wind is mesothermal ($v_{ti} \ll v_d \ll v_{te}$) plasma flow, we model the solar wind ions as a mono-energetic beam and the solar wind electrons as a drifting Maxwellian distribution (see Fig. 2.3). The photoelectrons are assumed to be emitted from the surface as a stationary Maxwellian distribution. Fig. 2.4 illustrates the stationary and drifting Maxwellian distribution functions. Here, v_m is the minimum velocity for electrons to reach an object. Those electrons with an initial kinetic energy smaller than minimum velocity $v_{m,0} = \sqrt{\frac{2e(-\phi_m)}{m}}$ will be reflected by the potential barrier. Obviously. the drifting velocity will increase the current from the free electrons which overcome the potential barrier.

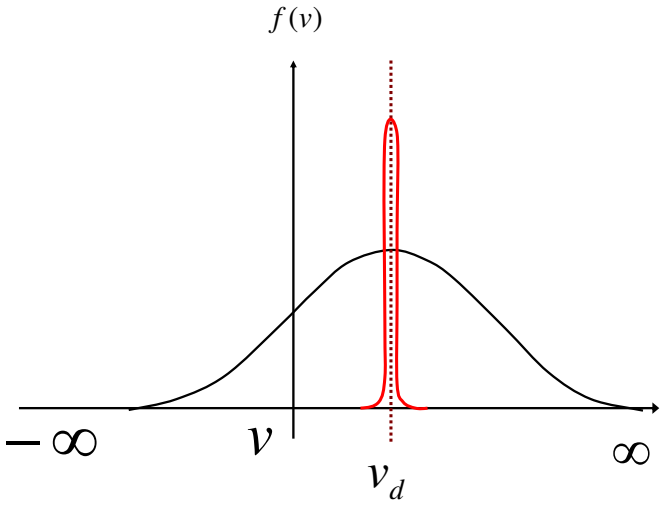

Figure 2.3: Illustration of the Maxwellian distribution function for electrons (black) and cold beam for ions (red).

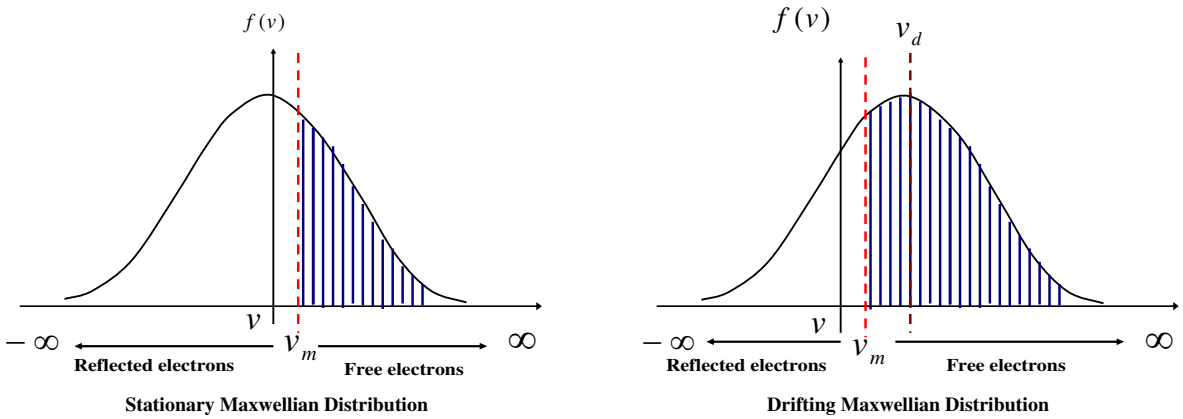

Figure 2.4: Illustration of the stationary and drifting Maxwellian distribution functions.

2.2 Current Balance Calculation

The Maxwellian distribution function for a stationary plasma in the absence of an external electric field is given by:

$$f_j(x,v) = n_j(\frac{m}{2\pi kT_j})^{3/2}\exp(-\frac{m(v_x^2+v_y^2+v_z^2)}{2kT_j}) \tag{2.2}$$

The one-sided current density on a planar object is given by:

$$J_j = J_{j0} = q_j\int_{-\infty}^{\infty}\int_{-\infty}^{\infty}\int_{0}^{\infty}\overrightarrow{v}\cdot\overrightarrow{n}\,f_j(v)dv_zdv_ydv_x = q_jn_j\sqrt{\frac{kT_j}{2\pi m_j}} \tag{2.3}$$

In the presence of a charged plate with surface potential ϕ_0, the current density for the attracted species to the plate is:

$$J_j = J_{j0} = q_jn_j\sqrt{\frac{kT_j}{2\pi m_j}} \tag{2.4}$$

and that for the repelled species

$$J_j = J_{j0}\exp(\frac{-e\phi_0}{kT_j}) = q_jn_j\sqrt{\frac{kT_j}{2\pi m_j}}\exp(-\frac{e\phi_0}{kT_j}) \tag{2.5}$$

where ϕ_0 is the surface floating potential. The Maxwellian distribution function for drifting plasma in the absence of an external electric field is:

$$f_j(x,v) = n_j(\frac{m}{2\pi kT_j})^{3/2}\exp(-\frac{m(v_x^2+v_y^2+(v_z-v_d)^2)}{2kT_j}) \tag{2.6}$$

The one-sided current density on a planar object is given by:

$$\begin{aligned} J_j = J_{j0} &= q_j\int_{-\infty}^{\infty}\int_{-\infty}^{\infty}\int_{0}^{\infty}\overrightarrow{v}\cdot\overrightarrow{n}\,f_j(v)dv_zdv_ydv_x \\ &= q_jn_j\frac{1}{2}(\frac{v_t}{\sqrt{\pi}}\exp(-(\frac{v_d}{v_t})^2) + v_d(1+erf(\frac{v_d}{v_t}))) \end{aligned} \tag{2.7}$$

In the presence of a charged plate with surface potential ϕ_0, the current density for the attracted species is:

$$J_j = J_{j0} = q_j n_j \frac{1}{2}\left(\frac{v_t}{\sqrt{\pi}} \exp(-(\frac{v_d}{v_t})^2) + v_d(1 + erf(\frac{v_d}{v_t}))\right) \tag{2.8}$$

and that for the repelled species:

$$J_j = J_{j0} \exp(\frac{-e\phi_0}{kT_j}) \quad = \quad q_j n_j \frac{1}{2}\left(\frac{v_t}{\sqrt{\pi}} \exp(-(\frac{v_d}{v_t})^2) + v_d(1 + erf(\frac{v_d}{v_t}))\right) \exp(-\frac{e\phi_0}{kT_j}) \tag{2.9}$$

In this dissertation, the ambient electrons are modeled as a drifting Maxwellian distribution while photoelectrons on the surface are modeled as a stationary Maxwellian distribution. The ambient ions are modeled as a cold beam. Hence, when the surface floating potential is positive, the current balance equation can be written as

$$J_{net}(\phi_0) = J_{e0} - J_{i0} - J_{ph0} \exp(-\frac{e\phi_0}{kT_{ph}}) = 0 \qquad \phi_0 > 0 \tag{2.10}$$

Here, the ion current is:

$$J_{i0} = en_i v_i = en_i \sqrt{v_d^2 - \frac{2e\phi_0}{m}} \tag{2.11}$$

where we have assumed a normal impingement of ion flow:

$$\frac{1}{2}mv_d^2 = \frac{1}{2}mv_i^2 - e\phi_0 \tag{2.12}$$

When the surface potential is negative, the current balance equation is

$$J_{net}(\phi_s) = J_{e0} \exp(\frac{e\phi_0}{kT_e}) - J_{i0} - J_{ph0} = 0 \qquad \phi_0 < 0 \tag{2.13}$$

where

$$J_{i0} = en_i v_i = en_i v_d \tag{2.14}$$

2.3 Photoelectron Sheath Theory

2.3.1 Photoelectron Sheath

In this section, we introduce the analytical approach of solving the photoelectron sheath in the presence of a drifting plasma. The approach presented here is based on the previous studies by Guernsey [28], Fu [18], and Nitter [69]. In the previous study, it was assumed that the ambient plasma consists of cold and drifting ions and stationary Maxwellian electrons. A detailed photoelectron theory for stationary electrons is included in Appendix A. In this work, we extend their approach by further considering a drifting Maxwellian distribution for the ambient electrons. In the presence of photoelectron emissions, there can exist three types of sheath profiles depending on the relative magnitude of incident emitting current. It has been suggested that for stationary electrons, a non-monotonic potential profile exists only under the condition of $n_{ph}/n_e > T_e/T_{ph} > 1$ where T denotes temperature and n_e and n_{ph} are the density of plasma electrons and photoelectrons, respectively [18]. Figure 2.5 illustrates the three different types of potential profiles. Here, ϕ_m and ϕ_0 are the potential minimum and the surface floating potential, respectively. Type A shows that the potential first decreases from a positive or negative surface potential to a negative minimum potential and then increases to zero non-monotonically. Type B shows a monotonic profile in which the potential decreases from the positive surface potential to zero. Type C shows a monotonic profile in which the potential increases from a negative surface potential to zero. Depending on the sheath type and electron energy, the electrons can be classified into four populations: captured photoelectrons, free photoelectrons, reflected electrons, and free electrons, respectively. The energy conservation equation for the electrons can be written as

$$\frac{1}{2}mv^2(x) - e\phi(x) = \frac{1}{2}mv_k^2 - e\phi_k \tag{2.15}$$

where $k = 0$ for photoelectrons and $k = \infty$ for plasma electrons. Those photoelectrons

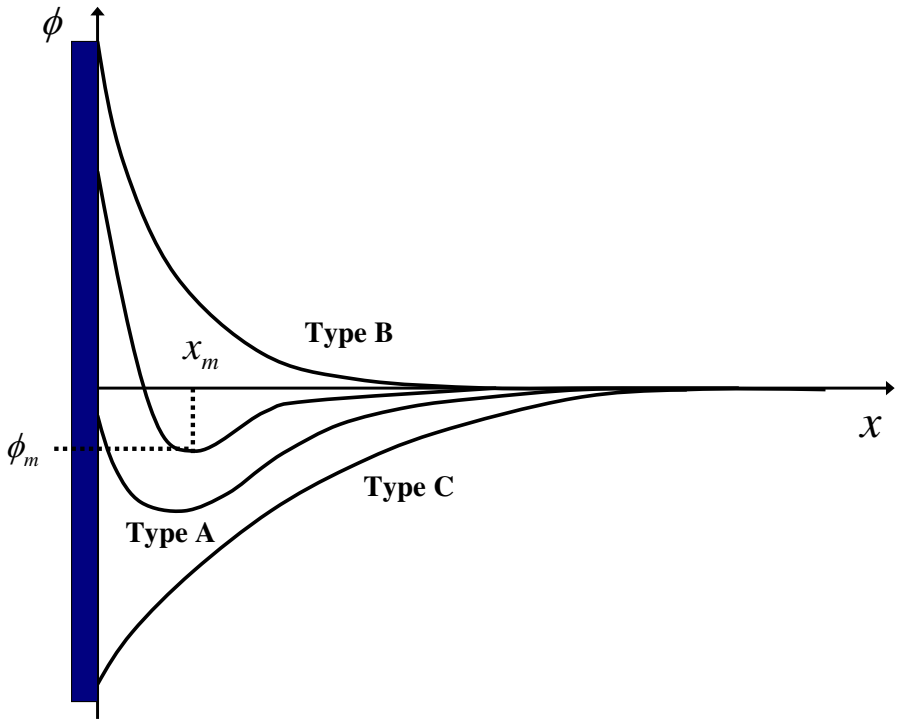

Figure 2.5: Schematic for the potential distribution surrounding an object.

with a velocity in the range of $-v_{m,0} < v < v_{m,0}$, where $v_{m,0} = \sqrt{\frac{2e(\phi_0 - \phi_m)}{m}}$ is the minimum velocity needed to overcome the potential barrier, will be trapped at $0 < x < x_m$ and hence will be called captured photoelectrons. Those photoelectrons with velocity in the range of $v_{m,0} < v < \infty$ will escape to infinity and hence will called free photoelectrons. Similarly, those ambient electron with a velocity in the range of $v > v_{m,\infty} = \sqrt{\frac{2e(\phi_\infty - \phi_m)}{m}}$ will be able to reach the object surface, and hence will be called free electrons. Those electrons with velocity in the range of $0 < v < v_{m,\infty}$ will be reflected by the potential barrier and will be called reflected electrons. All four populations can exist in the type A sheath. The type B sheath has three populations: free electrons, captured photoelectrons, and free photoelectrons. The type C sheath also has three populations: free electrons, reflected electrons, and free photoelectrons. Fig. 2.6 - 2.8 show the different electron populations for for the three types of sheath.

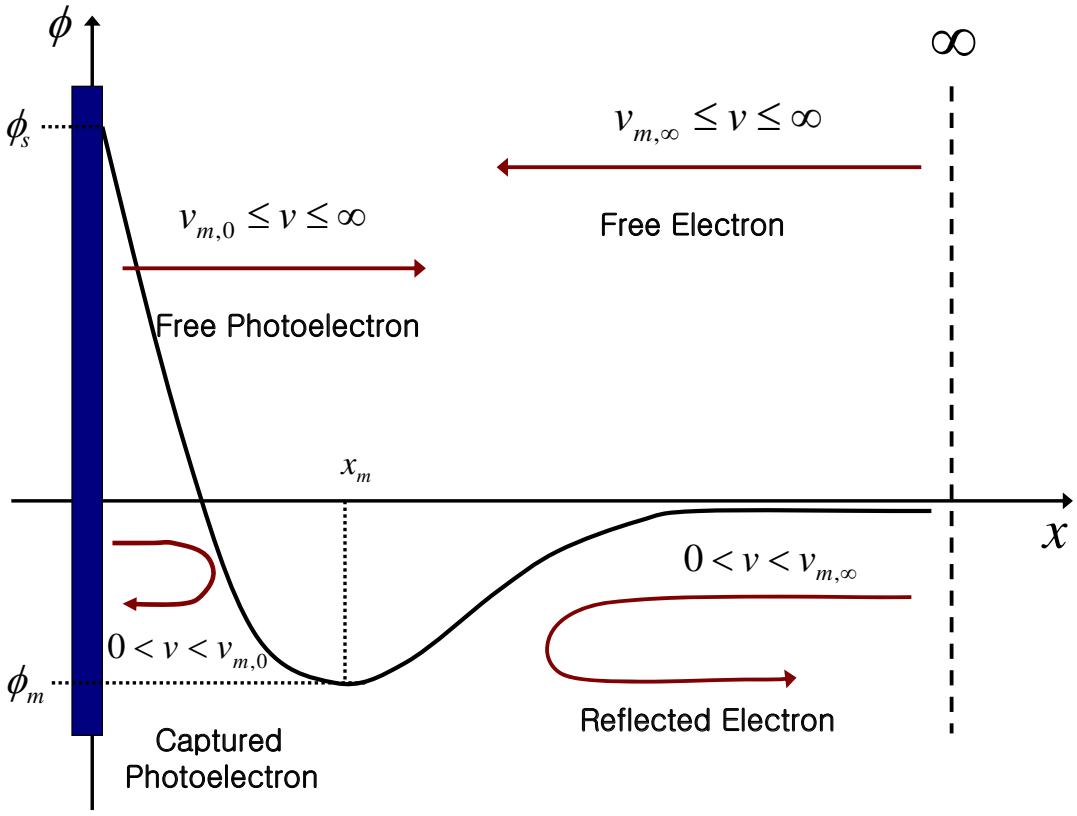

Figure 2.6: Schematic for four electron populations in a non-monotonic sheath profile.

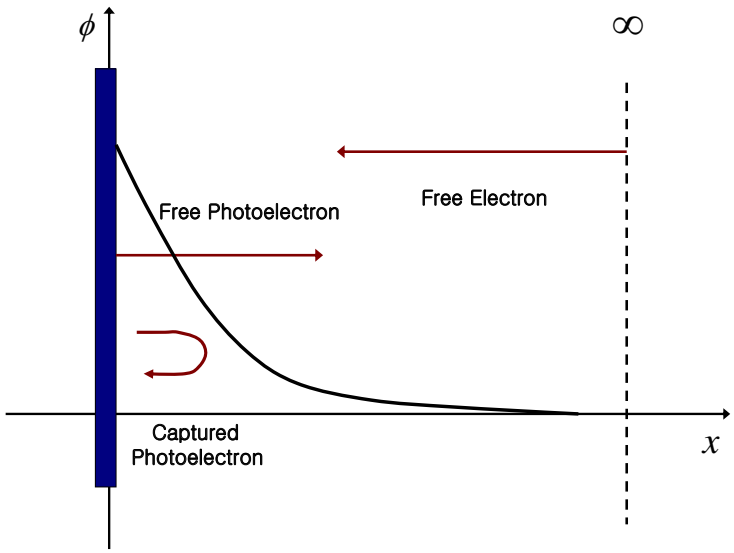

Figure 2.7: Schematic for three electron populations in a monotonic sheath profile of type B.

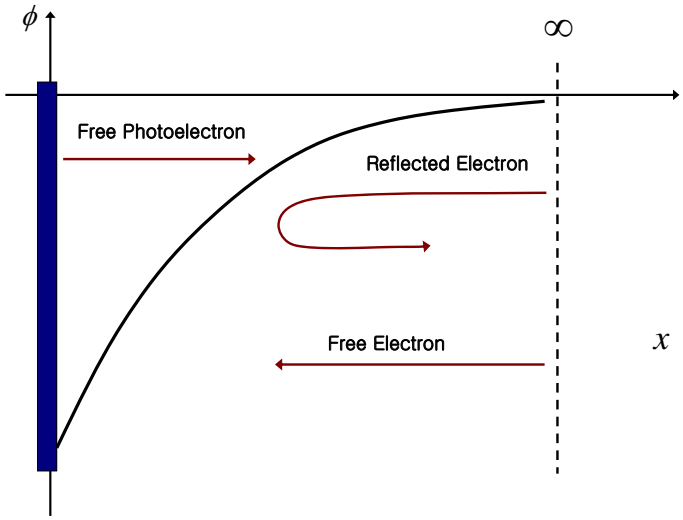

Figure 2.8: Schematic for three electron populations in a monotonic sheath profile of type C.

2.3.2 Non-monotonic Sheath Profile: Type A

The drifting Maxwellian distribution function for ambient electrons is given by

$$f_e(x,v) = n_e(\frac{m}{2\pi kT_e})^{3/2}\exp(-\frac{m(v_x^2+v_y^2+(v_z-v_d)^2)}{2kT_e}+\frac{e(\phi(x)-\phi_\infty)}{kT_e}) \tag{2.16}$$

where v_d is the drifting velocity for z-direction.

For the type A sheath, the density distribution functions for ambient free electrons $n_{e,f}$ and reflected electrons $n_{e,r}$ can be obtained as

$$\begin{aligned} n_{e,f}(x) &= \int_{-\infty}^{\infty}\int_{-\infty}^{\infty}\int_{v_m}^{\infty} f_e(v)d^3v = \frac{n_e}{2}\exp(\frac{e(\phi(x)-\phi_\infty)}{kT_e})(1-erf\sqrt{\frac{e(\phi(x)-\phi_m)}{kT_e}}-\frac{v_d}{v_t}) \quad (2.17)\\ n_{e,r}(x) &= 2\int_{-\infty}^{\infty}\int_{-\infty}^{\infty}\int_{0}^{v_m} f_e(v)d^3v = n_e\exp(\frac{e(\phi(x)-\phi_\infty)}{kT_e})[erf(\frac{v_d}{v_t})+erf(\sqrt{\frac{e(\phi(x)-\phi_m)}{kT_e}}-\frac{v_d}{v_t})] \end{aligned}$$

where $v_m(x)=\sqrt{\frac{2e(\phi(x)-\phi_m)}{m_e}}$ is minimum velocity required to overcome the potential barrier, $v_t=\sqrt{\frac{2kT_e}{m_e}}$ the thermal velocity, and $\phi_\infty = 0$ the potential at infinity. The density distribution functions for free photoelectrons $n_{p,f}$ and captured photoelectrons $n_{p,c}$ are given by

$$n_{p,f}(x) = \int_{-\infty}^{\infty}\int_{-\infty}^{\infty}\int_{v_m}^{\infty} f_p(v)d^3v = \frac{n_p}{2}\exp(\frac{e(\phi(x)-\phi_0)}{kT_p})(1-erf\sqrt{\frac{e(\phi(x)-\phi_m)}{kT_p}}) \tag{2.18}$$

$$n_{p,c}(x) = 2\int_{-\infty}^{\infty}\int_{-\infty}^{\infty}\int_{0}^{v_m} f_p(v)d^3v = n_p\exp(\frac{e(\phi(x)-\phi_0)}{kT_p})(erf\sqrt{\frac{e(\phi(x)-\phi_m)}{kT_p}}) \tag{2.19}$$

where $f_p(v)$ is the stationary Maxwellian distribution for photoelectrons and ϕ_0 is surface floating potential. The ion density distribution is given by

$$n_i(x) = n_\infty\frac{v_\infty}{v_i(x)} = n_\infty(1-\frac{2e\phi(x)}{v_\infty^2 m})^{-\frac{1}{2}} \tag{2.20}$$

The Poisson's equation is

$$\frac{d^2\phi}{dx^2} = -\frac{e}{\varepsilon_0}(n_i - n_{e,f} - n_{e,r} - n_{p,f} - n_{p,c}) \tag{2.21}$$

where the equation is normalized using $\hat{x} = \frac{x}{\lambda_p}$, $\hat{\phi} = \frac{e\phi}{kT_p}$, and $\hat{n} = \frac{n}{n_p}$. Then, it can be simplified using

$$\frac{d}{dx}(\frac{d\hat{\phi}}{d\hat{x}})^2 = 2(\frac{d\hat{\phi}}{d\hat{x}})\frac{d^2\hat{\phi}}{d\hat{x}^2}, \tag{2.22}$$

The Poisson's equation can be rewritten as

$$(\frac{d\hat{\phi}}{d\hat{x}})^2 = 2\int_{\hat{\phi_m}}^{\hat{\phi_x}}(\hat{n}_{e,f} + \hat{n}_{e,r} + \hat{n}_{p,f} + \hat{n}_{p,c} - \hat{n}_i)d\hat{\phi} \tag{2.23}$$

The electric field generated by the free electrons $E_{e,f}$ and reflected electrons $E_{e,c}$ are given by

$$\begin{aligned} E_{e,f} &= 2\int_{\hat{\phi_m}}^{\hat{\phi_x}} \hat{n}_{e,f}d\hat{\phi} = \hat{n}_{e,\infty}\beta\{\exp(\frac{\hat{\phi_x} - \hat{\phi_\infty}}{\beta})[erfc(\sqrt{\frac{\hat{\phi_x} - \hat{\phi_m}}{\beta}} - \frac{v_d}{v_t})] \\ &+ \exp(\frac{\hat{\phi_m} - \hat{\phi_\infty}}{\beta})[erfc(\frac{v_d}{v_t} - 2)] + \frac{1}{\sqrt{\pi}}(\frac{v_d}{v_t})^{-1}\exp(\frac{\hat{\phi_m} - \hat{\phi_\infty}}{\beta} - \frac{{v_d}^2}{{v_t}^2}) \\ &\times [\exp(2\frac{v_d}{v_t}\sqrt{\frac{\hat{\phi_x} - \hat{\phi_m}}{\beta}}) - 1]\} \end{aligned} \tag{2.24}$$

$$\begin{aligned} E_{e,r} &= 2\int_{\hat{\phi_m}}^{\hat{\phi_x}} \hat{n}_{e,r}d\hat{\phi} = 2\hat{n}_{e,\infty}\beta\{\exp(\frac{\hat{\phi_x} - \hat{\phi_\infty}}{\beta})[erf(\sqrt{\frac{\hat{\phi_x} - \hat{\phi_m}}{\beta}} - \frac{v_d}{v_t}) + erf(\frac{v_d}{v_t})] \\ &+ \frac{1}{\sqrt{\pi}}(\frac{v_d}{v_t})^{-1}\exp(\frac{\hat{\phi_m} - \hat{\phi_\infty}}{\beta} - \frac{{v_d}^2}{{v_t}^2})[1 - \exp(2\frac{v_d}{v_t}\sqrt{\frac{\hat{\phi_x} - \hat{\phi_m}}{\beta}})]\} \end{aligned} \tag{2.25}$$

where $\hat{\phi_\infty} = 0$ since plasma is neutralized at infinity. The electric field generated by the free photoelectrons $E_{p,f}$ and captured photoelectrons $E_{p,c}$ are:

$$\begin{aligned} E_{p,f} &= 2\int_{\hat{\phi_m}}^{\hat{\phi_x}} \hat{n}_{p,f}d\hat{\phi} = 2\int_{\hat{\phi_m}}^{\hat{\phi_x}} \frac{\hat{n}_{p,0}}{2}\exp(\hat{\phi} - \hat{\phi_m})[1 - erf(\sqrt{\hat{\phi} - \hat{\phi_m}})]d\hat{\phi} \\ &= \hat{n}_{p,0}\{\exp(\hat{\phi_x} - \hat{\phi_m})[1 - erf(\sqrt{\hat{\phi_x} - \hat{\phi_m}})] + \exp(\hat{\phi_m} - \hat{\phi_m})[\frac{2}{\sqrt{\pi}}\sqrt{\hat{\phi_x} - \hat{\phi_m}} - 1]\} \end{aligned} \tag{2.26}$$

$$\begin{aligned} E_{p,c} &= 2\int_{\hat{\phi_m}}^{\hat{\phi_x}} \hat{n}_{p,c}d\hat{\phi} = 2\int_{\hat{\phi_m}}^{\hat{\phi_x}} \hat{n}_{p,0}\exp(\hat{\phi} - \hat{\phi_m})erf(\sqrt{\hat{\phi} - \hat{\phi_m}})d\hat{\phi} \\ &= 2\hat{n}_{p,0}\{\exp(\hat{\phi_x} - \hat{\phi_m})erf(\sqrt{\hat{\phi_x} - \hat{\phi_m}}) - \frac{2}{\sqrt{\pi}}\exp(\hat{\phi_m} - \hat{\phi_m})\sqrt{\hat{\phi_x} - \hat{\phi_m}}\} \end{aligned} \tag{2.27}$$

The electric field generated by ions is

$$E_i = -2\int_{\hat{\phi_m}}^{\hat{\phi_x}} n_i d\hat{\phi} = \frac{2\hat{n}_{i,\infty}}{n}\beta M^2[\sqrt{1-\frac{2\hat{\phi_x}}{\beta M^2}} - \sqrt{1-\frac{2\hat{\phi_m}}{\beta M^2}}] \tag{2.28}$$

where c_s is the ion acoustic velocity, $M = v_\infty/c_s$, and $\beta = \frac{T_e}{T_p}$.

To determine the potential minimum ϕ_m, the surface floating potential ϕ_0, and the electron density n_e at infinity, the following boundary conditions are used: 1) quasi-neutral condition at infinity, 2) zero electric field at infinity, and 3) zero total current. The neutrality condition at infinity can be obtained through the equations (2.17) and (2.19):

$$\begin{aligned} n_e(\infty) + n_p(\infty) - n_i(\infty) &= n_{e,f}(\infty) + n_{e,r}(\infty) + n_{p,f}(\infty) - n_i(\infty) \\ &= \frac{n_{e,\infty}}{2}[1 + 2erf(\frac{v_d}{v_t}) + erf(\sqrt{-\frac{\hat{\phi_m}}{\beta}} - \frac{v_d}{v_t})] \\ &+ \frac{n_{p,0}}{2}\exp(-\hat{\phi_0})(1 - erf\sqrt{-\hat{\phi_m}}) - n_{i,\infty} = 0 \end{aligned} \tag{2.29}$$

The condition for zero total electric field at infinity can be written as

$$E(\infty) = E_{e,f}(\infty) + E_{e,r}(\infty) + E_{p,f}(\infty) + E_i(\infty) = 0 \tag{2.30}$$

where

$$\begin{aligned} E_{e,f}(\infty) &= n_{e,\infty}\beta\{[erfc(\sqrt{\frac{-\hat{\phi_m}}{\beta}} - \frac{v_d}{v_t})] + \exp(\frac{\hat{\phi_m}}{\beta})[erfc(\frac{v_d}{v_t} - 2)] \\ &+ \frac{1}{\sqrt{\pi}}(\frac{v_d}{v_t})^{-1}\exp(\frac{\hat{\phi_m}}{\beta} - \frac{{v_d}^2}{{v_t}^2})[\exp(2\frac{v_d}{v_t}\sqrt{\frac{-\hat{\phi_m}}{\beta}}) - 1]\} \end{aligned} \tag{2.31}$$

$$E_{e,r}(\infty) = n_{e,\infty}\beta\{[erf(\sqrt{\frac{-\hat{\phi_m}}{\beta}} - \frac{v_d}{v_t}) + erf(\frac{v_d}{v_t})] + \frac{1}{\sqrt{\pi}}(\frac{v_d}{v_t})^{-1}\exp(\frac{\hat{\phi_m}}{\beta} - \frac{{v_d}^2}{{v_t}^2})[\exp(2\frac{v_d}{v_t}\sqrt{\frac{-\hat{\phi_m}}{\beta}}) - 1]\}$$

$$E_{p,f}(\infty) = n_{p,0}\exp(-\hat{\phi_0})[1 - erf(\sqrt{-\hat{\phi_m}})] + \exp(\hat{\phi_m} - \hat{\phi_0})[\frac{2}{\sqrt{\pi}}\sqrt{-\hat{\phi_m}} - 1]$$

$$E_i(\infty) = 2n_{i,\infty}\beta M^2(1 - \sqrt{1 - \frac{2\hat{\phi_x}}{\beta M^2}})$$

The total current is zero at steady state where the captured photoelectrons and the reflected electrons do not contribute to the total current. Hence, the zero total current condition can be written as

$$J_{e,f}(\infty) + J_{p,f}(0) - J_i(\infty) = \int_{-\infty}^{\infty}\int_{-\infty}^{\infty}\int_{v_m(0)}^{\infty} v_x f_p(0,v) dv_x dv_y dv_z + \int_{-\infty}^{\infty}\int_{-\infty}^{\infty}\int_{-\infty}^{-v_m(\infty)} v_x f_e(\infty,v) dv_x dv_y dv_z + n_i(\infty) v_i(\infty) = 0 \tag{2.32}$$

where $v_m(x) = \sqrt{\frac{2e(\phi(x)-\phi_m)}{m_e}}$ and $\phi_\infty = 0$. Equation (2.32) can be simplified as:

$$n_{p,0}\exp(\hat{\phi_m} - \hat{\phi_0}) - n_{e,\infty}\sqrt{\beta}\{\exp[-(\sqrt{\frac{-\hat{\phi_m}}{\beta}} + \frac{v_d}{v_t})^2] - \frac{v_d}{v_t}\sqrt{\pi} erfc(\frac{v_d}{v_t} + \sqrt{\frac{-\hat{\phi_m}}{\beta}})\} + n_{i,\infty}\sqrt{2\pi\beta m_e/m_i} M = 0 \tag{2.33}$$

Then, the Poisson's equation can be re-written as

$$\frac{d\hat{\phi}}{d\hat{x}} = \sqrt{E_{e,f} + E_{e,r} + E_{p,f} + E_{p,c} + E_i} = \sqrt{E_{tot}(\hat{\phi})} \tag{2.34}$$

When $\hat{x} \le \hat{x_m}$, the non-monotonic sheath profile can be found by integrating $\hat{\phi}$ from $\hat{\phi_0}$ to an arbitrary $\hat{\phi_x}$ for $\hat{\phi_0} < \hat{\phi_x} \le \hat{\phi_m}$:

$$\hat{x} = \int_{\hat{\phi_x}}^{\hat{\phi_0}} \frac{1}{\sqrt{E_{tot}(\hat{\phi})}} d\hat{\phi} \qquad \hat{x} \le \hat{x_m} \tag{2.35}$$

When $\hat{x} > \hat{x_m}$, the sheath profile can be obtained by

$$\hat{x} = \int_{\hat{\phi_x}}^{\hat{\phi_\infty}} \frac{1}{\sqrt{E_{tot}(\hat{\phi})}} d\hat{\phi} \qquad \hat{x} > \hat{x_m} \tag{2.36}$$

where $\hat{\phi_m} < \hat{\phi_x} \le \hat{\phi_\infty}$. Here, the location $\hat{x_m}$ of minimum potential can be found by integrating using the obtained surface floating potential $\hat{\phi_0}$ and $\hat{\phi_m}$. It is given by

$$\hat{x_m} = \int_0^{\hat{x_m}} d\hat{x} = \int_0^{\hat{x_m}} \frac{d\hat{x}}{d\hat{\phi}}\frac{d\hat{\phi}}{d\hat{x}} d\hat{x} = \int_{\hat{\phi_m}}^{\hat{\phi_0}} \frac{1}{\sqrt{E_{tot}(\hat{\phi})}} d\hat{\phi} \tag{2.37}$$

2.3.3 Monotonic Sheath Profile: Type B

The type B sheath profile does not contain reflected electrons. For this case, the Poisson's equation can be re-written by using electric field:

$$\frac{d\hat{\phi}}{d\hat{x}} = \sqrt{E_{e,f} + E_{p,f} + E_{p,c} + E_i} = \sqrt{E_{tot}(\hat{\phi})} \tag{2.38}$$

where the electric field generated by each population are shown in Equations (2.24)-(2.28). To calculate two unknown variables of the surface floating potential $\hat{\phi_0}$ and electron density at infinity n_e, two boundary conditions can be applied: 1) neutrality at infinity and 2) zero total current at steady state. Neutrality at infinity is

$$n_e(\infty) + n_p(\infty) - n_i(\infty) = n_{e,f}(\infty) + n_{p,f}(\infty) - n_i(\infty) = 0$$

The zero total current at steady state can be written as

$$n_{p,0}\exp(\hat{\phi_m} - \hat{\phi_0}) - n_{e,\infty}\sqrt{\beta}\{\exp[-(\sqrt{\frac{-\hat{\phi_m}}{\beta}} + \frac{v_d}{v_t})^2] \tag{2.39}$$

$$-\frac{v_d}{v_t}\sqrt{\pi}erfc(\frac{v_d}{v_t} + \sqrt{\frac{-\hat{\phi_m}}{\beta}})\} + n_{i,\infty}\sqrt{2\pi\beta m_e/m_i}M = 0$$

Finally, the monotonic potential distribution corresponding to $\hat{x}$ can be determined by integrating $\hat{\phi}$ from $\hat{\phi_0}$ to an arbitrary $\hat{\phi_x}$ as follows:

$$\hat{x} = \int_{\hat{\phi_x}}^{\hat{\phi_0}} \frac{1}{\sqrt{E_{tot}(\hat{\phi})}} d\hat{\phi} \tag{2.40}$$

where $\hat{\phi_0} < \hat{\phi_x} \leq \hat{\phi_\infty}$

2.3.4 Monotonic Sheath Profile: Type C

In type C, there are no captured photoelectrons and $\hat{\phi_m} = \hat{\phi_0}$. To obtain the potential distribution, the electric field is found by integrating the Poisson's equation from $\hat{\phi_0} = 0$ to

an arbitrary $\hat{\phi_x}$. The electric field generated by free electrons $E_{e,f}$ and reflected electrons $E_{e,r}$ are

$$\begin{aligned} E_{e,f} &= 2\int_0^{\hat{\phi_x}} \hat{n}_{e,f} d\hat{\phi} = \hat{n}_{e,\infty}\beta\{\exp(\frac{\hat{\phi_x}-\hat{\phi_\infty}}{\beta})[erfc(\sqrt{\frac{\hat{\phi_x}-\hat{\phi_0}}{\beta}} - \frac{v_d}{v_t})] \\ &+ [erf(\sqrt{\frac{-\hat{\phi_0}}{\beta}} - \frac{v_d}{v_t}) - 1] + \frac{1}{\sqrt{\pi}}(\frac{v_d}{v_t})^{-1}\exp(\frac{\hat{\phi_0}-\hat{\phi_\infty}}{\beta} - \frac{{v_d}^2}{{v_t}^2}) \\ &\quad [\exp(2\frac{v_d}{v_t}\sqrt{\frac{\hat{\phi_x}-\hat{\phi_0}}{\beta}}) - \exp(2\frac{v_d}{v_t}\sqrt{\frac{-\hat{\phi_0}}{\beta}})]\} \end{aligned} \tag{2.41}$$

$$\begin{aligned} E_{e,r} &= 2\int_0^{\hat{\phi_x}} \hat{n}_{e,r} d\hat{\phi} = 2\hat{n}_{e,\infty}\beta\{\exp(\frac{\hat{\phi_x}-\hat{\phi_\infty}}{\beta})[erf(\sqrt{\frac{\hat{\phi_x}-\hat{\phi_0}}{\beta}} - \frac{v_d}{v_t}) + erf(\frac{v_d}{v_t})] \\ &- \exp(\frac{-\hat{\phi_\infty}}{\beta})[erf(\sqrt{\frac{-\hat{\phi_0}}{\beta}} - \frac{v_d}{v_t}) + erf(\frac{v_d}{v_t})] \\ &+ \frac{1}{\sqrt{\pi}}(\frac{v_d}{v_t})^{-1}\exp(\frac{\hat{\phi_0}-\hat{\phi_\infty}}{\beta} - \frac{{v_d}^2}{{v_t}^2})[\exp(2\frac{v_d}{v_t}\sqrt{\frac{-\hat{\phi_0}}{\beta}}) - \exp(2\frac{v_d}{v_t}\sqrt{\frac{\hat{\phi_x}-\hat{\phi_0}}{\beta}})]\} \end{aligned} \tag{2.42}$$

The electric field generated by free photoelectrons is

$$\begin{aligned} E_{p,f} &= 2\int_0^{\hat{\phi_x}} \hat{n}_{p,f} d\hat{\phi} = 2\int_0^{\hat{\phi_x}} \frac{\hat{n}_{p,0}}{2}\exp(\hat{\phi}-\hat{\phi_m})[1-erf(\sqrt{\hat{\phi}-\hat{\phi_m}})]d\hat{\phi} \\ &= \hat{n}_{p,0}\exp(-\hat{\phi_m})\{\exp(\hat{\phi_x})[erfc(\sqrt{\hat{\phi_x}-\hat{\phi_0}}\,)] - erfc(\sqrt{-\hat{\phi_0}}\,) \\ &+ \frac{2}{\sqrt{\pi}}\exp(\hat{\phi_0})[\sqrt{\hat{\phi_x}-\hat{\phi_0}} - \sqrt{-\hat{\phi_0}}\,]\} \end{aligned} \tag{2.43}$$

The electric field generated by ions is

$$E_i = -2\int_{\hat{\phi_m}}^{\hat{\phi_x}} n_i d\hat{\phi} = \frac{2\hat{n}_{i,\infty}}{n}\beta M^2[\sqrt{1-\frac{2\hat{\phi_x}}{\beta M^2}} - 1] \tag{2.44}$$

The unknown variables $\hat{\phi_0}$ and n_e are simply calculated from 1) neutrality at infinity and 2) zero total current at steady state. Neutrality condition at infinity can be obtained by

$$\begin{aligned} n_e(\infty) + n_p(\infty) - n_i(\infty) = n_{e,f}(\infty) + n_{e,r}(\infty) + n_{p,f}(\infty) - n_i(\infty) \\ = \frac{n_{e,\infty}}{2}[1 + 2erf(\frac{v_d}{v_t}) + erf(\sqrt{-\frac{\hat{\phi_0}}{\beta}} - \frac{v_d}{v_t})] + \frac{n_{p,0}}{2}\exp(-\hat{\phi_0})(1 - erf\sqrt{-\hat{\phi_0}}) - n_{i,\infty} = 0 \end{aligned} \tag{2.45}$$

Zero total current at steady state can be written as

$$n_{p,0} - n_{e,\infty}\sqrt{\beta}\{\exp[-(\sqrt{\frac{-\hat{\phi}_0}{\beta}} + \frac{v_d}{v_t})^2] \tag{2.46}$$

$$-\frac{v_d}{v_t}\sqrt{\pi}erfc(\frac{v_d}{v_t} + \sqrt{\frac{-\hat{\phi}_0}{\beta}})\} + n_{i,\infty}\sqrt{2\pi\beta m_e/m_i}M = 0$$

Then, the sheath profile can be obtained from

$$\hat{x} = \int_{\hat{\phi}_x}^{\hat{\phi_\infty}} \frac{1}{\sqrt{E_{tot}(\hat{\phi})}} d\hat{\phi} \tag{2.47}$$

where $\hat{\phi}_0 < \hat{\phi}_x \leq \hat{\phi_\infty}$

2.4 Results

In this section, the results from the analytical approach are presented. We consider a surface under sunlit condition and typical solar wind plasma condition. Both the solar wind flow and the solar radiation direction is assumed to be normal to the surface. The parameters for photoelectron emissions and the ambient solar wind are listed in Table 2.1. Laboratory experiments show that photoelectrons emitted from surface may be modeled by a stationary Maxwellian distribution with energy in the range of 0 to $\sim 5eV$. The average energy is $\sim 1.5eV$ [27]. Here, we take the photoelectron temperature to be $T_{ph} = 1, 2$, and 4 to examine the effect of photoelectron energy.

Fig. 2.9 presents comparison of the photoelectron sheath obtained for stationary electrons (solid line) and drifting electrons (dashed line). The photoelectron temperature is assumed to be $T_{ph} = 2eV$. As mentioned previously, there are two solutions in the photoelectron sheath when photoelectron emissions are significant. The figure shows two types of the sheath determined by using the analytical method: non-monotonic (top) and monotonic (bottom) sheath profiles. Fig. 2.10 shows the density distributions related to electron populations in

the vicinity of photoelectron sheath: non-monotonic (top) and monotonic (bottom) sheath profiles. The dashed and solid lines are the distributions from drifting electrons and stationary electrons, respectively. Fig. 2.11 shows the density distributions related to photoelectron populations. Fig. 2.12 compares the sheath profile between stationary and drifting electrons. The results obtained from the analytical solution for drifting ambient electrons are shown in the bottom panel. For comparison, we also include the solution from Ref.[18, 69] obtained for stationary ambient electron in the top panel. As expected, when the effect of drifting electrons is included, the solution shows that the surface floating potential becomes lower due to increased electron current collection. Moreover, the minimum potential in the non-monotonic sheath profile also becomes more negative.

Table 2.2 shows the quantitative comparison of the surface floating potential ϕ_0, the minimum potential in the sheath ϕ_m, and distance between minimum potential and the plate r_m for two solutions presented in Ref.[18, 69] and the current balance calculation. Here, N and M indicate non-monotonic potential profile (type A) and monotonic potential profile (type B), respectively. Similarly, Table 2.3 shows comparison of the surface floating potential ϕ_0, the minimum potential in the sheath ϕ_m, and distance between minimum potential and the plate r_m for two solutions and the current balance calculation for drifting electrons. Not surprisingly, the surface floating potentials obtained from current balance calculation agree with type B solution (monotonic sheath) because the current balance calculation assumes a monotonic sheath. However, there are significant differences between the type A (non-monotonic solution) and the type B (non-monotonic solution).

Table 2.1: Parameters used in analytical method.

Parameter	Solarwind	Photoelectron
Density, cm^{-3}	$n \sim 3.5$	$n \sim 35$
Temperature, eV	$T_e \sim 15$,$T_i \sim 10$	$T_{ph} \sim 1, 2, 4$
Drifting Velocity , km/s	$v_d \sim 400$	–

We next consider the situation for non-normal solar wind incidence as shown in Fig. 2.13. We

Table 2.2: Comparison of surface floating potential ϕ_0, potential minimum ϕ_m, and distance between minimum potential and a plate r_m for stationary electrons. N and M indicate non-monotonic potential profile (Type A) and monotonic potential profile (Type B).

	Stationary electrons						Current balance		
	$1eV$		$2eV$		$4eV$		$1eV$	$2eV$	$4eV$
	N	M	N	M	N	M			
ϕ_0, V	0.42	2.09	3.47	4.56	9.22	9.75	1.91	4.52	10.37
ϕ_m, V	-1.52	–	-0.88	–	-0.26	–	–	–	–
r_m, m	5.55	–	9.61	–	19.04	–	–	–	–

assume that the directions of ambient solar wind and solar radiation are identical. Fig. 2.14 represents the comparison of the sheath profiles obtained using the stationary Maxwellian electrons (solid line) and drifting Maxwellian electrons (dashed line) for solar wind parameters given in Table 1.1. Here, blue, red, and green lines indicate $\alpha = 6^o$, 8^o, and 10^o, respectively. As expected, the sheath profile obtained using drifting Maxwellian electrons has a more negative surface floating potential. It is obvious that surface potential is more negative at smaller incident angles due to reduced photoelectron emissions and reduced incident ion current. Table 2.4 shows the quantitative comparison of the surface floating potential through different incident angles between the current balance calculation and photoelectron sheath theory for the parameters shown in Table 2.1 ($T_{ph} = 2eV$). Fig. 2.15 shows comparison of the surface floating potentials between current balance calculation (point) and photoelectron sheath theory for type C (blue circle), type B (red circle), and type A (black diamond). Table 2.4 shows quantitative comparisons between current balance calculation and photoelectron sheath theory. We found that the surface floating potentials from current balance calculation agree with those of the monotonic potential profile (type B or type C). There is obvious discrepancy starting at α 15^o between current balance calculation and non-monotonic potential profile. However, a non-monotonic potential profile would be a

Table 2.3: Comparison of surface floating potential ϕ_0, potential minimum ϕ_m, and distance between minimum potential and a plate r_m for drifting electrons. N and M indicate non-monotonic potential profile (Type A) and monotonic potential profile (Type B).

	Drifting electrons						Current balance		
	$1eV$		$2eV$		$4eV$		$1eV$	$2eV$	$4eV$
	N	M	N	M	N	M			
ϕ_0, V	-2.24	1.92	0.77	3.97	6.36	8.2	1.27	3.24	7.86
ϕ_m, V	-3.71	–	-2.70	–	-1.49	–	–	–	–
r_m, m	5.94	–	10.0	–	17.0	–	–	–	–

stable solution under certain conditions [18]. The potential barrier generated by the minimum potential will modify not only the photoelectron current but also the incident ambient current. Since the current balance calculation does not include the modification of current sources caused by the minimum potential, it may not be used to properly predict the surface floating potential for the situations where the photoelectron current is the dominant current source. The results in this dissertation suggest that when there are significant photoelectron emissions, the commonly used current balance calculation may predict a floating potential vary different from the non-monotonic potential of the photoelectron sheath theory. For instance, the difference between the current balance calculation and the non-monotonic sheath solution can be 76% for normal incidence.

Table 2.4: Comparison of the surface floating potential between the 1-D current balance calculation and photoelectron sheath theory.

α (^{o})	5	8	10	15	20	40	60	90
Current balance (ϕ_0, V)	-15.24	-8.45	-5.3	0.3	0.7	2.11	2.9	3.2
Type C (ϕ_0, V)	-15.55	-8.5	-4.69	-	-	-	-	-
Type B (ϕ_0, V)	-	-	-	0.74	1.33	2.69	3.36	3.7
Type A (ϕ_0, V)	-	-	-	-2.72	-1.88	-0.22	0.47	0.77

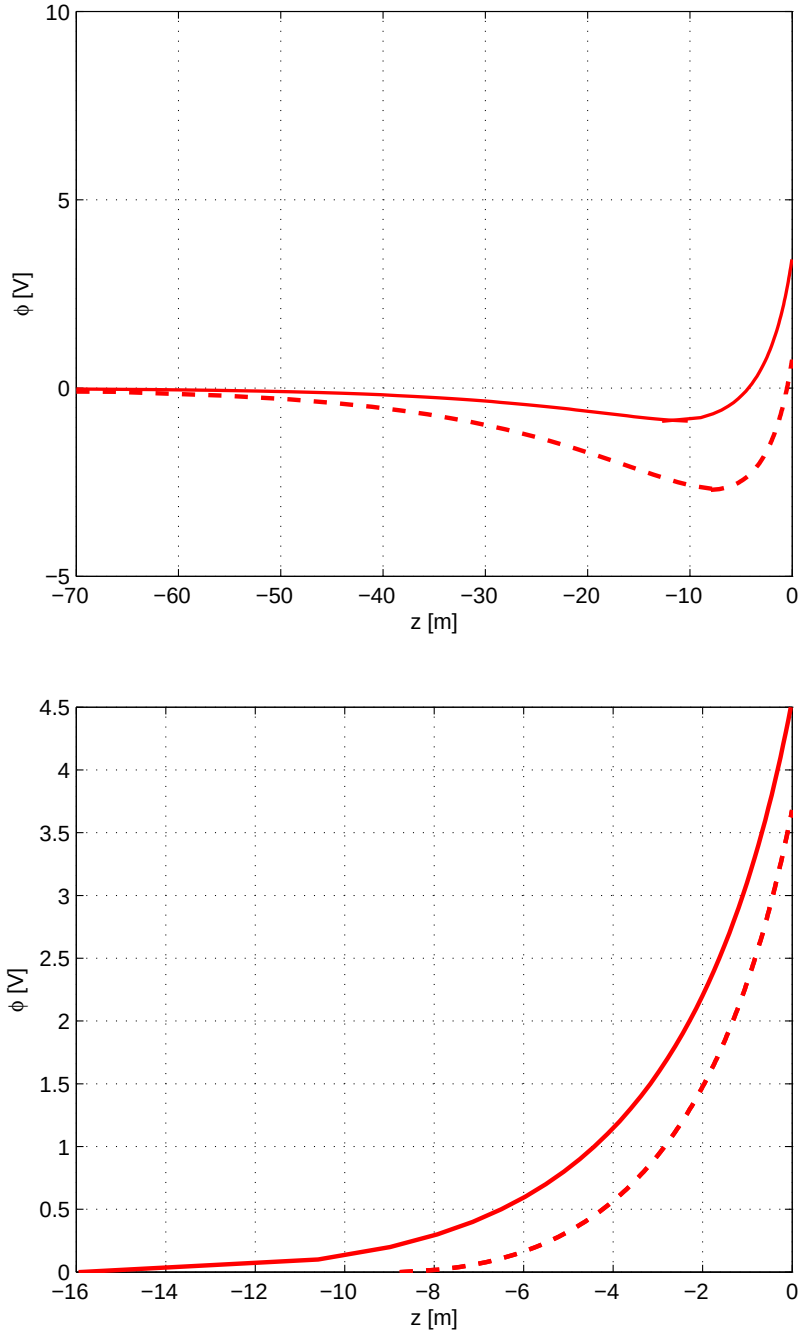

Figure 2.9: Comparison of the photoelectron sheath obtained from stationary (solid line) and drifting (dashed line) electrons at $T_{ph} = 2eV$: non-monotonic (top) and monotonic (bottom) sheath profiles.

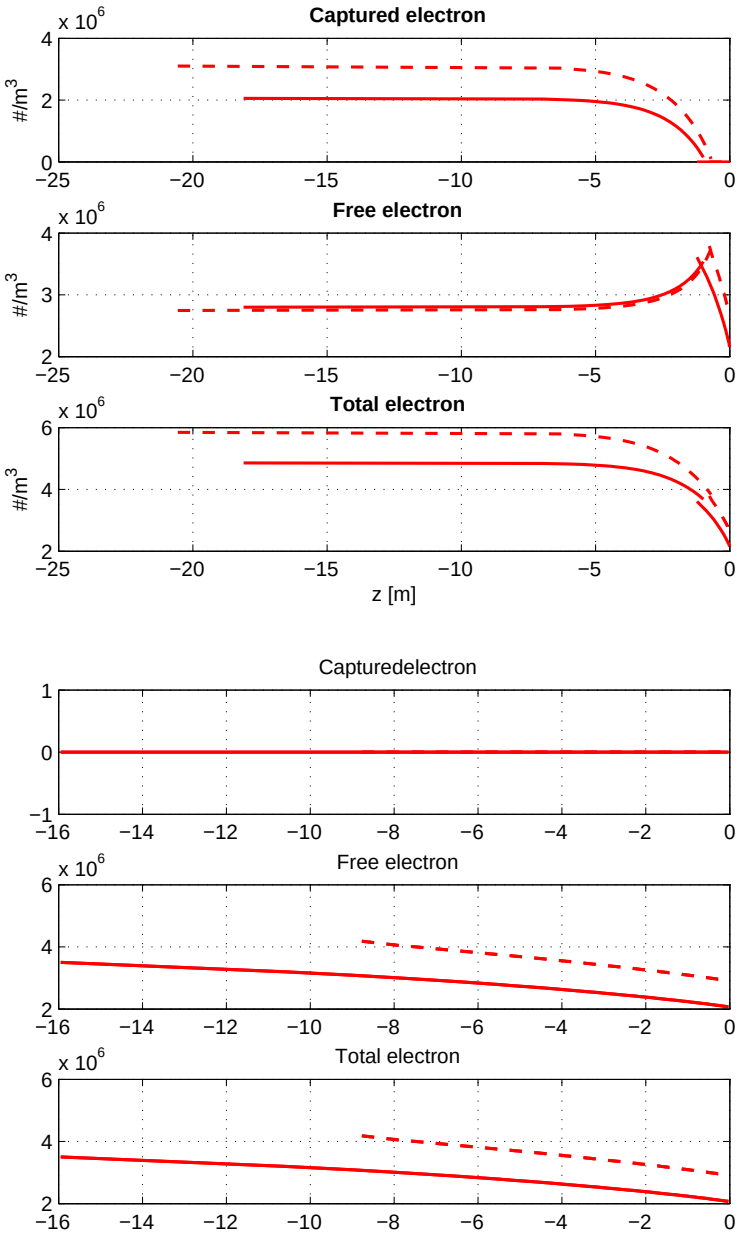

Figure 2.10: Comparison of electron density distributions obtained from stationary (solid line) and drifting (dashed line) electrons at $T_{ph} = 2eV$: non-monotonic (top) and monotonic (bottom) sheath profiles.

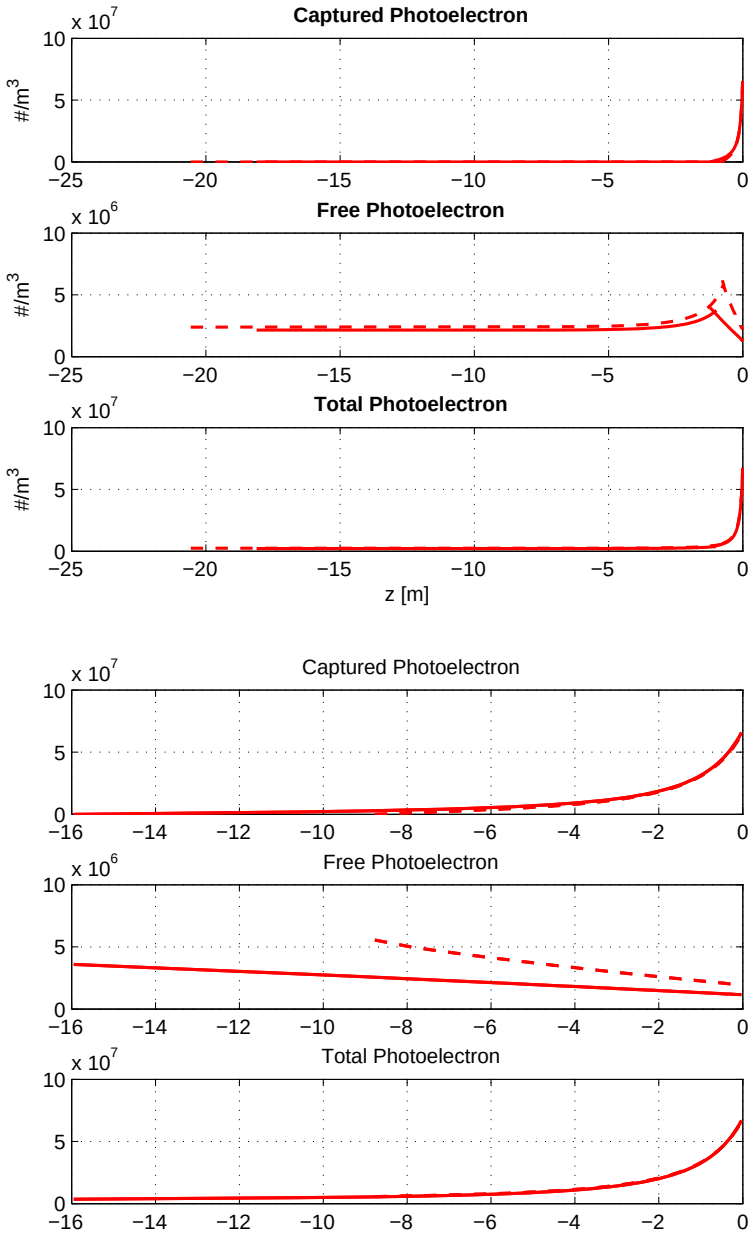

Figure 2.11: Comparison of photoelectron density distributions obtained from stationary (solid line) and drifting (dashed line) electrons at $T_{ph} = 2eV$: non-monotonic (top) and monotonic (bottom) sheath profile.

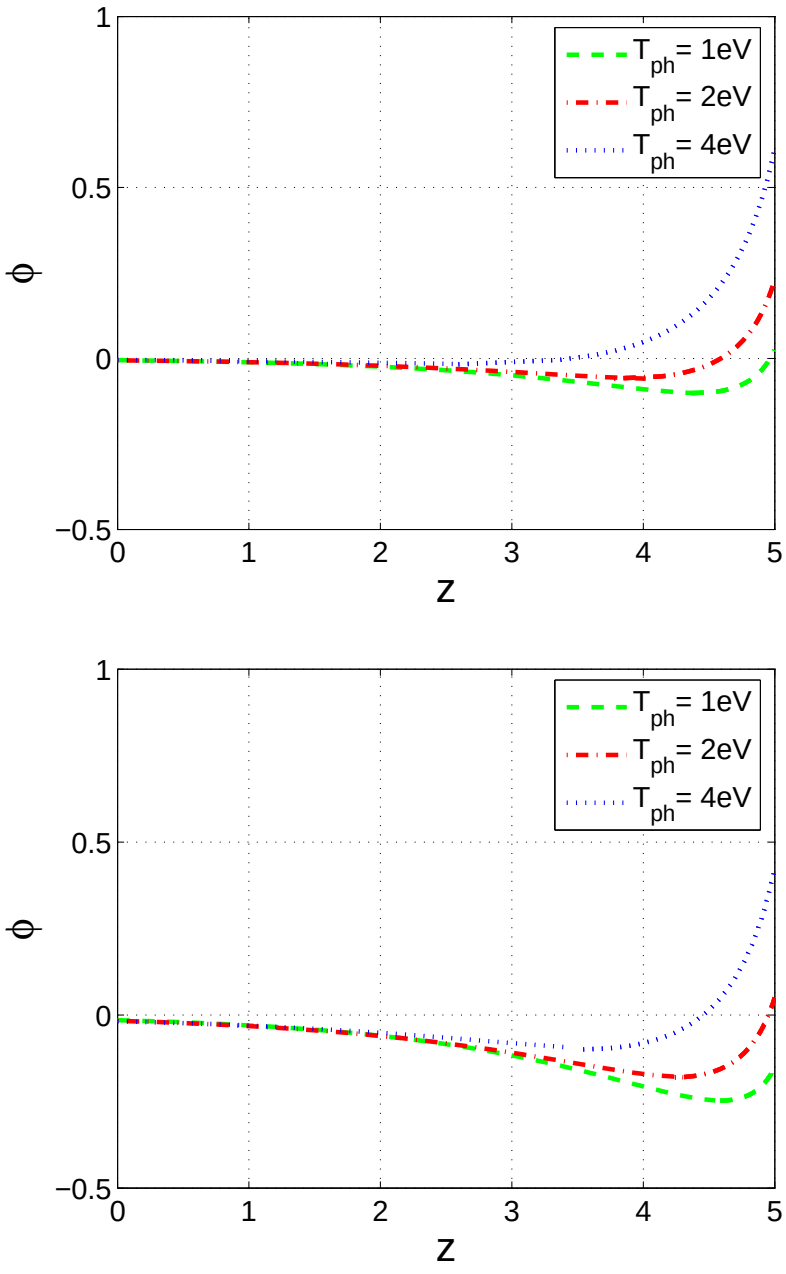

Figure 2.12: Comparison of the sheath profiles of the stationary electrons (top) with drifting electrons (bottom) where potential is normalized by T_e and z is normalized by λ_d.

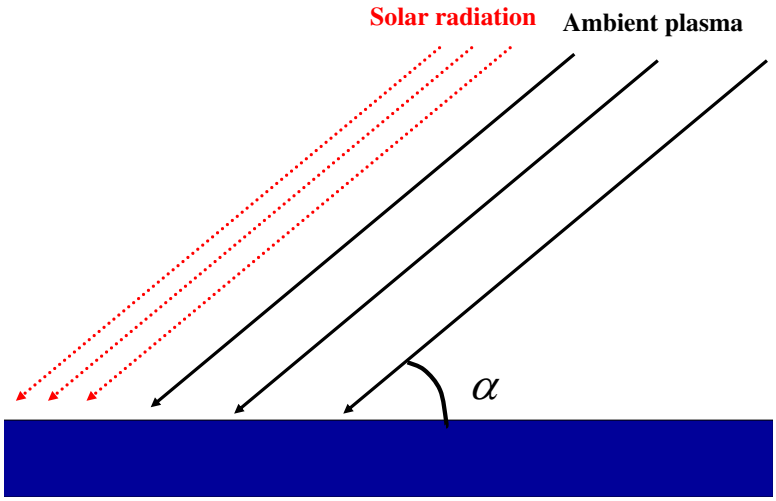

Figure 2.13: Schematic view for solar wind current with an angle α where the direction of ambient plasma is identical to that of solar wind.

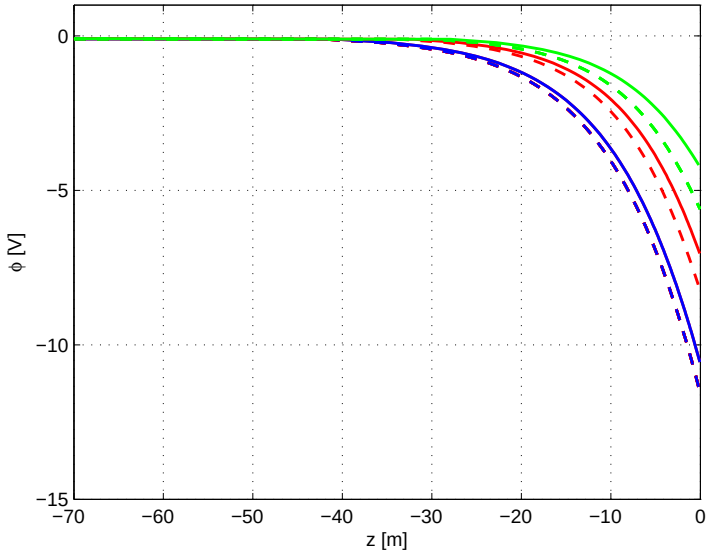

Figure 2.14: Comparison of the sheath profiles obtained using the stationary Maxwellian electrons (solid line) and drifting Maxwellian electrons (dashed line) where blue, red, and green lines are $\alpha = 6^o$, 8^o, and 10^o, respectively.

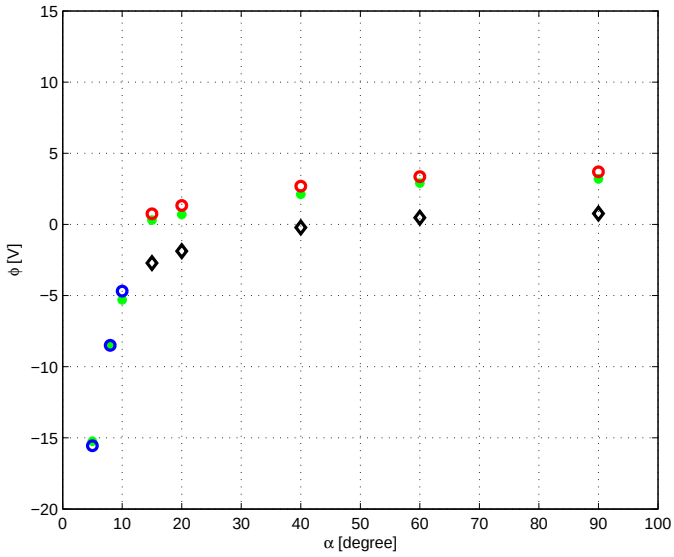

Figure 2.15: Comparison of the surface floating potentials between current balance calculation (point) and photoelectron sheath theory for Type C (blue circle), Type B (red circle), and Type A (black diamond).

Chapter 3

Numerical Simulation Model

3.1 Simulation Model

A 3-D full Particle In Cell (PIC) code is implemented to model spacecraft charging and plasma interactions in solar wind. This code originates from a 3-dimensional PIC code that was previously developed for modeling electron beam emissions [91] and electron propulsion plume interactions [92]. The particle trajectories and the electric fields are solved self-consistently from

$$\nabla \cdot (\varepsilon \nabla \phi) = -(\rho_i - \rho_e - \rho_{ph}) \tag{3.1}$$

$$\frac{d(mV)}{dt} = q\overrightarrow{E} \tag{3.2}$$

where ρ_i, ρ_e, and ρ_{ph} are the charge density for the ambient proton, ambient electron, and photoelectron, respectively. The simulation setup used in this dissertation is shown in Figure 3.1. We model the ambient solar wind protons and electrons as drifting Maxwellian distributions. The photoelectrons are emitted from the sunlit face of an object as a stationary Maxwellian distribution. Considering geometric symmetry, the simulations are performed

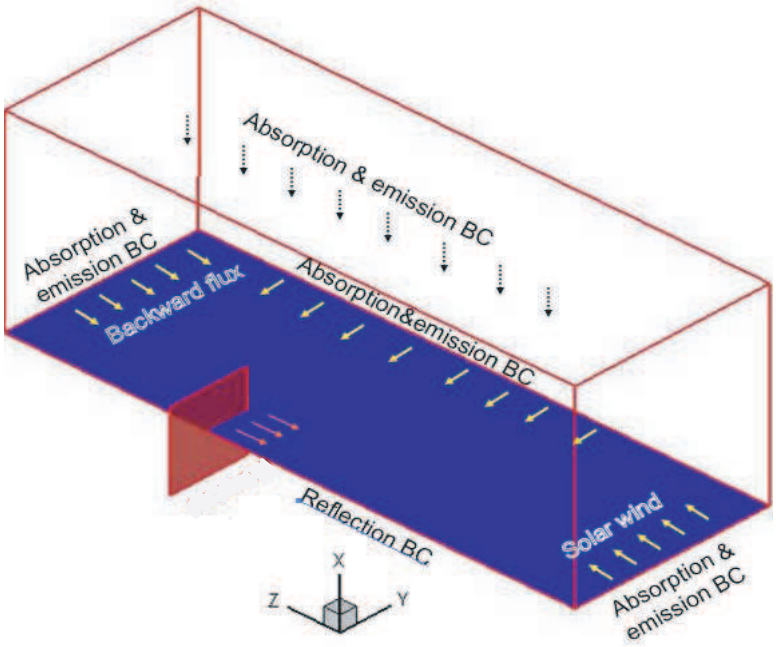

Figure 3.1: Schematic for simulation setup.

only for a quarter of the platform. The boundaries for $x = 0$ and $y = 0$ are symmetric surfaces while all other boundaries are open boundaries. The absorption and emission boundary conditions for particles are implemented on all open boundaries. The Dirichlet boundary condition for the electric field is applied at the upstream domain boundary while the open boundary condition for the electric field is imposed on all other boundaries. Macro-particles representing the solar wind protons and electrons are injected into the simulation domain as a drifting Maxwellian distribution along the z-axis at every time step. The direction of solar radiation is taken to be the same as that of the solar wind. Photoelectrons are emitted from the sunlit side of the surface as a one-sided stationary Maxwellian distribution. The time step is calculated dynamically from the cell size and the maximum velocity for particles at each time step. The number of macro-particles is typically about 50 per cell for each species. The simulation is performed using the real ion to electron mass ratio $m_i/m_e = 1836$ in order to maintain the correct mesothermal velocity ratio.

3.2 Initial and Boundary Conditions for Particles

In this section, the concept and methodology associated with the boundary condition for particle loading and injection are introduced. Full particle PIC models require sophisticated schemes for the loading and injection of particles at the simulation domain boundaries because any inaccuracy in handling the transient of fast moving electrons at the simulation domain can quickly result in numerical problems and/or wrong results. Macro-particles representing the ambient plasma are loaded in the simulation domain at the start of the simulation and injected into the simulation domain from the domain boundary at each time step. The Maxwellian distribution functions with drifting velocity v_d along the z-direction are given by

$$f(v_x, v_y, v_z) = n(\frac{m}{2\pi kT})^{3/2} \exp(-\frac{m(v_x^2 + v_y^2 + (v_z - v_d)^2)}{2kT}) \tag{3.3}$$

The cumulative distribution function is adopted in order to obtain the corresponding velocities for loaded particles in the domain at the initial condition. The cumulative distribution function for particle loading is given by

$$R = F(v) = \frac{\int_{-\infty}^{\infty}\int_{-\infty}^{\infty}\int_{-\infty}^{v} f(v')d^3v'}{\int_{-\infty}^{\infty}\int_{-\infty}^{\infty}\int_{-\infty}^{\infty} f(v')d^3v'} = \frac{1}{2}erfc(\frac{v_d - v}{v_t}) \tag{3.4}$$

where R is a random number, $0 < R < 1$. The velocity v for each loaded particle can be obtained by numerical inversion for each particle. In order to calculate the particle number and corresponding velocities for injected particles at each time step, the cumulative flux distribution function is applied [4, 5, 11]. When the ambient plasma is a drifting plasma, the particle numbers and the corresponding velocities for injected particles are different between the upstream and the downstream boundaries. Figure 3.2 shows the schematics for the drifting Maxwellian distribution at upstream and downstream boundaries. Figure 3.3 shows the Maxwellian distribution function corresponding to particle injection. At the upstream domain boundary, the mean velocity $\langle v \rangle$ associated with the inward flux from the drifting Maxwellian distribution is given by

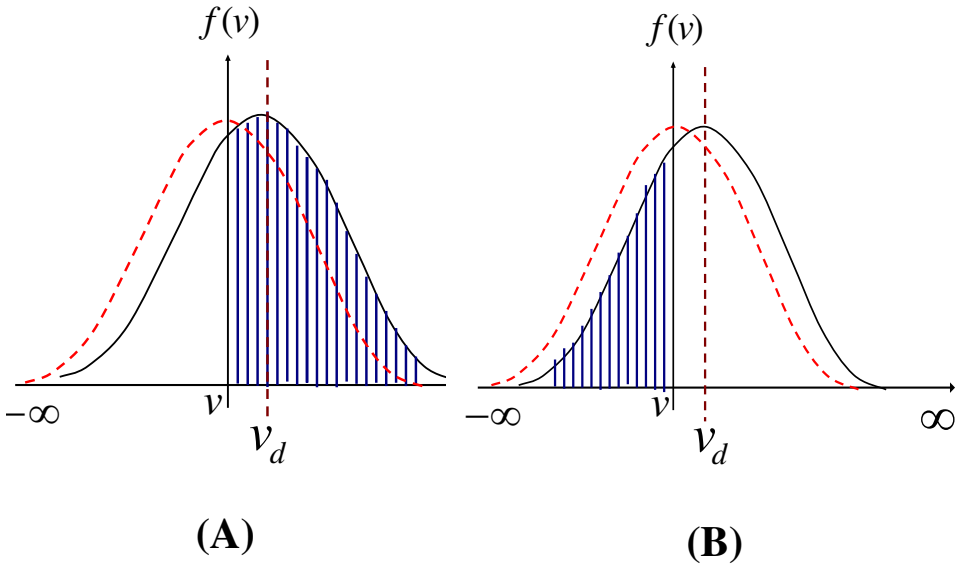

Figure 3.2: Drifting Maxwellian distribution for the particle injection at the upstream (A) and downstream (B) boundaries where a dashed line indicates the stationary Maxwellian distribution.

$$\langle v \rangle = \int_{-\infty}^{\infty}\int_{-\infty}^{\infty}\int_{0}^{\infty} v f(v) d^3v = \frac{1}{2}(\frac{v_t}{\sqrt{\pi}}\exp(-(\frac{v_d}{v_t})^2) + v_d(1 + erf(\frac{v_d}{v_t}))) \tag{3.5}$$

where $v_t = \sqrt{\frac{2kT}{m}}$ is defined as the thermal velocity and erf is the error function. Similarly, at the downstream domain boundary, the mean velocity associated with the backward flux of particles coming into the domain from the downstream is given by

$$\langle v \rangle = \int_{-\infty}^{\infty}\int_{-\infty}^{\infty}\int_{-\infty}^{0} v f(v) d^3v = \frac{1}{2}(v_d erfc(\frac{v_d}{v_t}) - \frac{v_t}{\sqrt{\pi}}\exp(-(\frac{v_d}{v_t})^2) \tag{3.6}$$

where $erfc$ is the complementary error function. Hence, the number of total particles to be injected at each boundary is

$$N_{inject} = n\Delta_{xy}\langle v \rangle dt \tag{3.7}$$

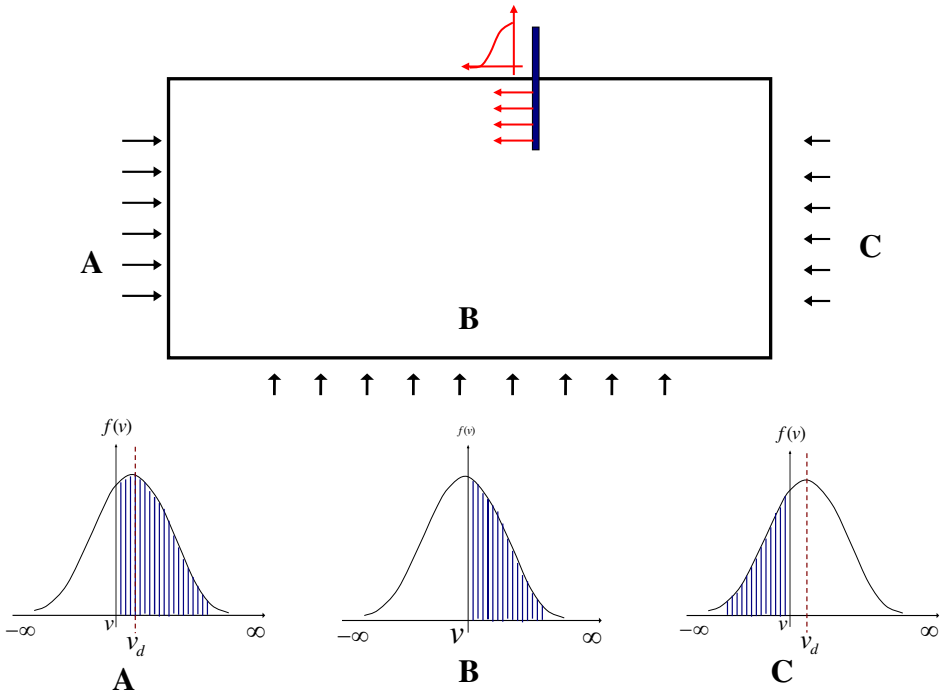

Figure 3.3: Schematics for the particle injection and corresponding distribution function.

where n and $\Delta_{xy}\langle v\rangle dt$ are the number density for macro-particle and the total volume obtained from the transverse width $\langle v\rangle dt$, respectively. The normal velocity corresponding to the flux at each boundary is calculated using the cumulative flux distribution function while the transverse velocity is obtained by the cumulative distribution function of Equation (3.4). The cumulative flux distribution function associated with the inward flow at the upstream boundary is given by

$$\begin{aligned} R &= F(v) = \frac{\int_{-\infty}^{\infty}\int_{-\infty}^{\infty}\int_{0}^{v} v' f(v') d^3v'}{\int_{-\infty}^{\infty}\int_{-\infty}^{\infty}\int_{0}^{\infty} v' f(v') d^3v'} = [v_t(\exp(-\frac{v_d^2}{v_t^2}) - \exp(-\frac{(v-v_d)^2}{v_t^2})) \\ &+ \sqrt{\pi} v_d (erf(\frac{v_d}{v_t}) + erf(\frac{v-v_d}{v_t}))]/(v_t \exp(-\frac{v_d^2}{v_t^2}) + \sqrt{\pi} v_d (1 + erf(\frac{v_d}{v_t}))) \end{aligned} \tag{3.8}$$

The cumulative flux distribution function associated with the backward flow at the downstream boundary is given by

$$R = F(v) = \frac{\int_{-\infty}^{\infty}\int_{-\infty}^{\infty}\int_{-\infty}^{v} v' f(v') d^3v'}{\int_{-\infty}^{\infty}\int_{-\infty}^{\infty}\int_{-\infty}^{0} v' f(v') d^3v'} \tag{3.9}$$

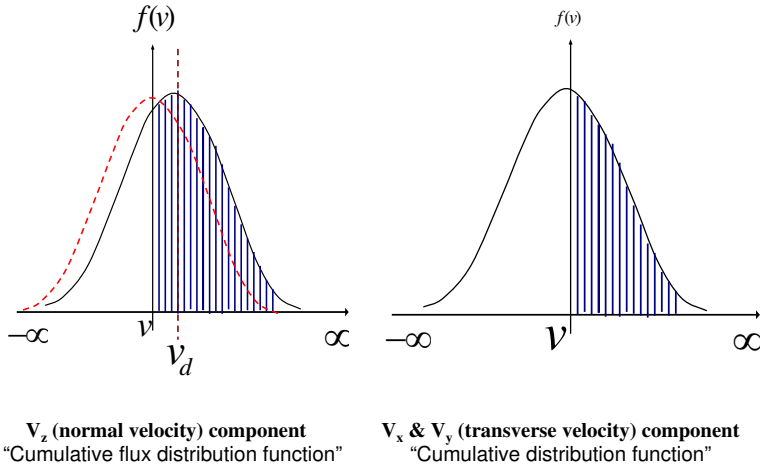

Figure 3.4: Schematic of Maxwellian distribution function to obtain a normal component and transverse components at the upstream boundary.

$$= [v_t \exp(-\frac{(v-v_d)^2}{v_t^2}) - \sqrt{\pi} v_d erfc(\frac{v_d - v}{v_t})]/(v_t \exp(-\frac{v_d^2}{v_t^2}) - \sqrt{\pi} v_d erfc(\frac{v_d}{v_t}))$$

Figures 3.4-3.6 show the distribution functions to obtain the normal and transverse velocities at each boundary. The velocities for each particle are then determined by using numerical inversion.

3.3 PIC Model Analysis

3.3.1 Sensitivity Analysis

This section describes a sensitivity analysis on mesh size and domain size for the parameters given in Table 2.1. Simulation setup used in the analysis is shown in Fig. 3.1. First, the sensitivity analysis are performed for various domain sizes. In order to properly model the open boundary, the domain size needs to be sufficiently large. In the simulations discussed

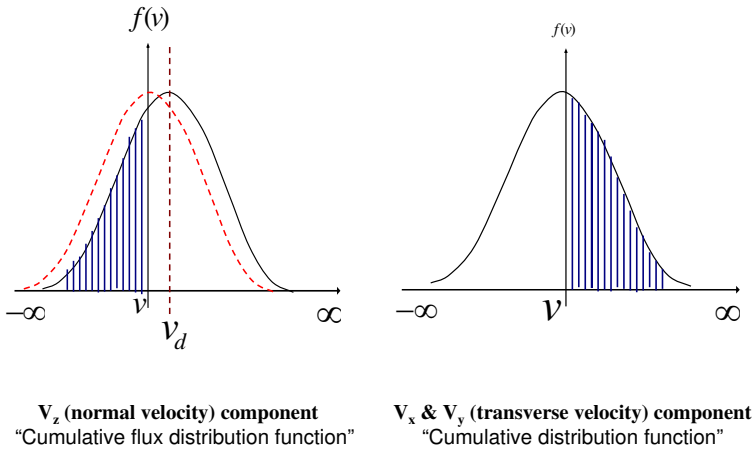

Figure 3.5: Schematic of Maxwellian distribution function to obtain a normal component and transverse components at the downstream boundary.

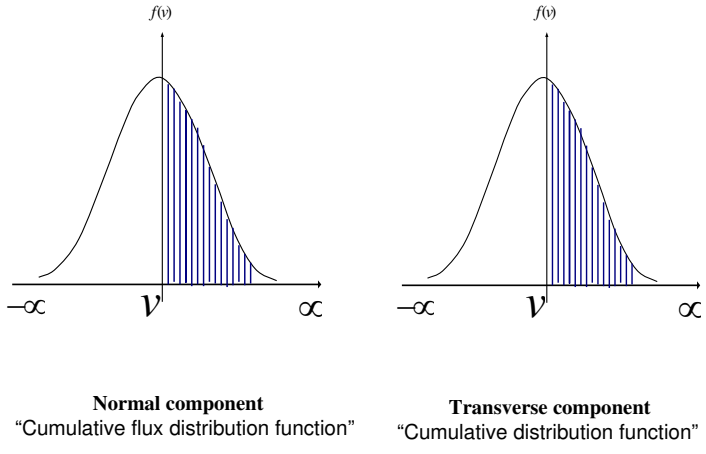

Figure 3.6: Schematic of Maxwellian distribution function to obtain a normal component and transverse components at other boundaries.

in this dissertation, we determined the minimum domain size z_{min} for z-axis by estimating the sheath thickness using the analytical method discussed in Chapter 2. For the minimum domain size of x-axis and y-axis, empirical way based on the plate size and photoelectron emission is applied. Figures 3.7 - 3.9 show the potential profiles for the domain size where the domain sizes start from the minimum domain to reduce boundary effects. As shown in the figures, the domain size selected here gives consistent solutions. We next investigate the effects of the mesh size to investigate the effect of mesh size. When we consider typical solar wind conditions in the presence of photoelectron emissions, the dominant current source in the vicinity of a charged spacecraft is the photoelectrons. Hence, in order to resolve the photoelectron sheath, the mesh size needs to be smaller than the Debye length of photoelectrons. The Debye length of photolectron and electron Debye length for the parameters used in the analysis are $\lambda_{ph} = 1.7m$ and $\lambda_d = 15.4m$, respectively. Obviously, simulations using $dx = \lambda_{ph}$ can be computationally expensive. The primary objective for sensitivity analysis of different mesh sizes is to find proper mesh size to reduce the computational cost. In the present simulation, $\Delta x = \Delta y = \Delta z = 0.1\lambda_d$ is mesh size resolving photoelectron Debye length. Fig. 3.10 shows the analysis associated with mesh size. It is found that the simulation results will not be affected by mesh size if $\Delta x = \Delta y = \Delta z \leq 0.2\lambda_d$. Thus, the simulations presented in Chapter 4 are performed in the range of the mesh size.

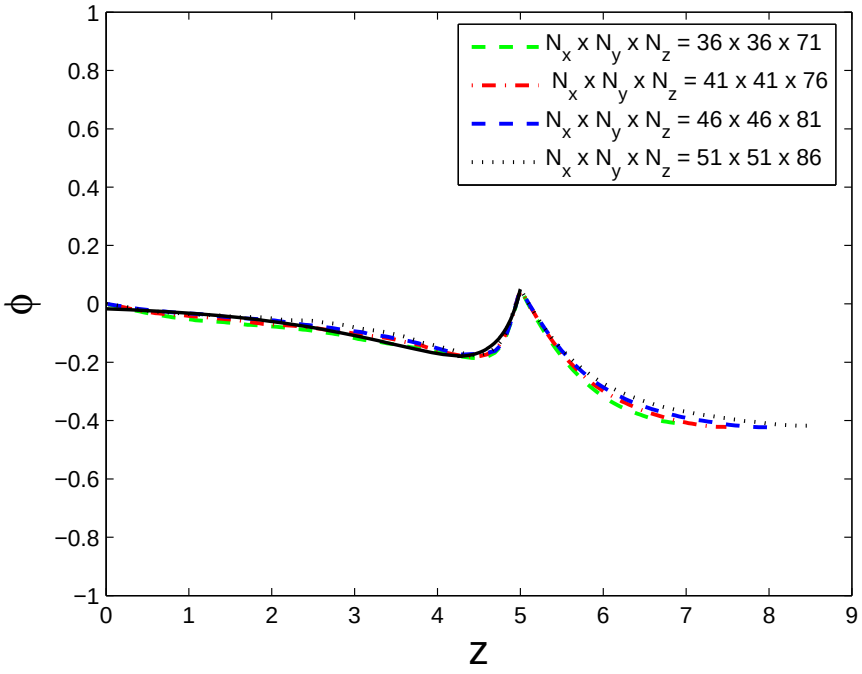

Figure 3.7: Potential profile along z-axis for different domain size at $\Delta x = \Delta y = \Delta z = 0.1\lambda_d$. Solid line indicates the sheath profile obtained from the analytical method.

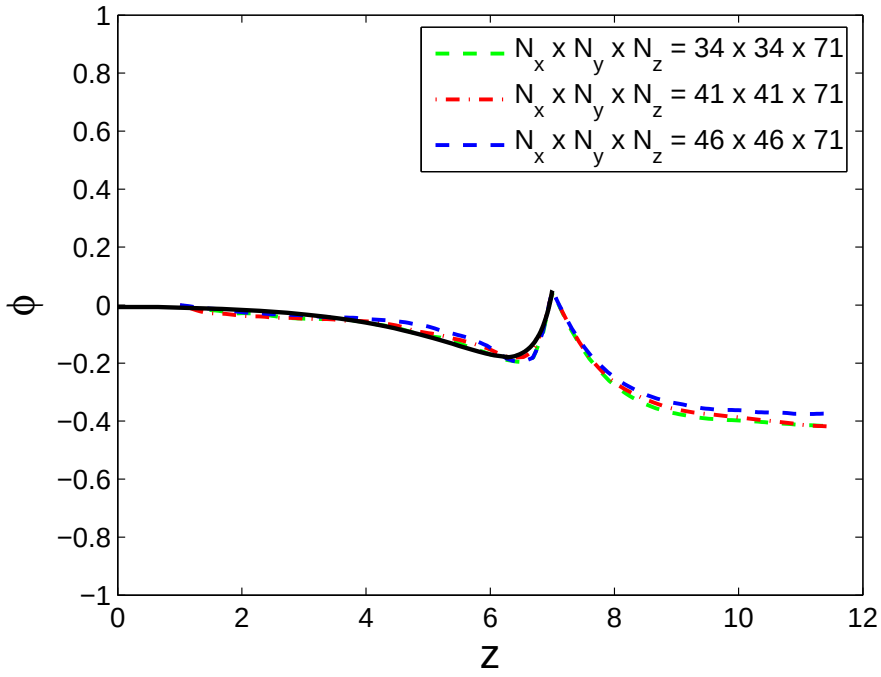

Figure 3.8: Potential profile along z-axis for different domain size at $\Delta x = \Delta y = \Delta z = 0.15\lambda_d$. Solid line indicates the sheath profile obtained from the analytical method.

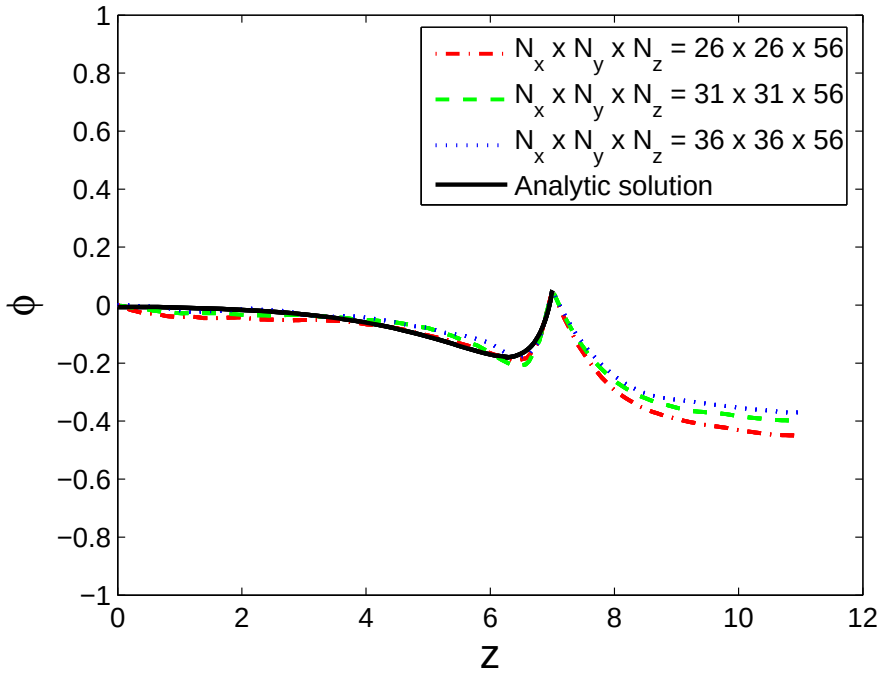

Figure 3.9: Potential profile along z-axis for different domain size at $\Delta x = \Delta y = \Delta z = 0.2\lambda_d$. Solid line indicates the sheath profile obtained from the analytical method.

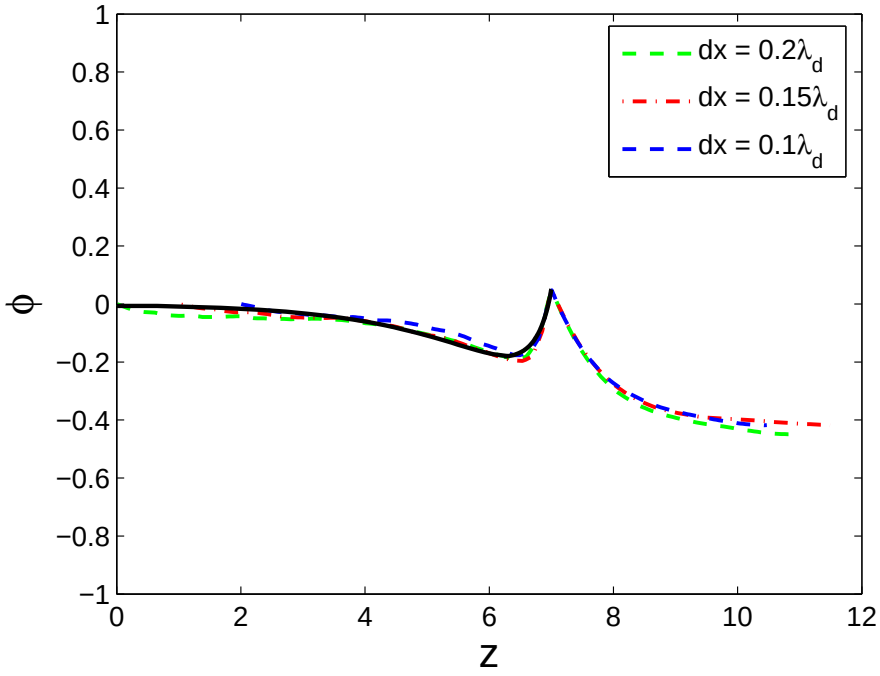

Figure 3.10: Sensitivity analysis for cell size. Cell size is normalized by $\lambda_d = 15.4m$.

3.3.2 Comparison with Sheath Measurement

In order to validate the PIC code, we carried out a simple simulation and compared the PIC results with sheath measurement. The experimental study used for this comparison is performed in [23] using laser-induced fluorescence (LIF). The ion source is Argon and the electrode was biased at $-100V$. Fig. 3.11 shows the experimental schematic. Table 3.1 shows the experimental input conditions. The simulation is carrried out for 1-D simulation setup where negative biased plate is placed on the z_{max}. $L_x \times L_y \times L_z$ is $4.5\lambda_d \times 4.5\lambda_d \times 45\lambda_d$ where $\Delta x = \Delta y = \Delta z = 0.9\lambda_d$. For the field boundary, open boundaries for x-surface and y-surface are imposed. The Dirichlet boundary condition for z-surface is used as $\phi = 0$ at z_{min} and $\phi = -100V$ at z_{max}. The absorption and emission boundary condition for particles are implemented on the upstream boundary while absorption boundary condition is used on the downstream boundary. Periodic boundary conditions are used for the other boundaries. Fig. 3.12 shows comparison of results obtained from the experimental data (point) and numerical simulation (solid line). We found the PIC code gives a good agreement with the measurement.

Table 3.1: Experimental input conditions.

Parameter	Experimental Input
Density, cm^{-3}	$n_e, n_i = 0.9 \times 10^8$
Temperature, eV	$T_e = 0.53$, $T_i = 0.0054$
Drifting Velocity , km/s	$v_d = 2.5$
Potential, V	$\phi = -100$

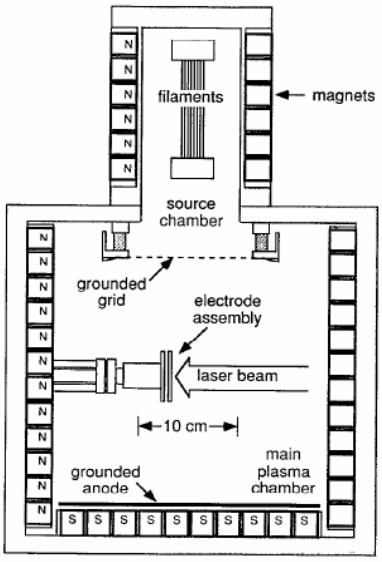

Figure 3.11: Schematic of plasma chamber used to measure plasma sheath using laser-induced fluorescence (LIF) [23].

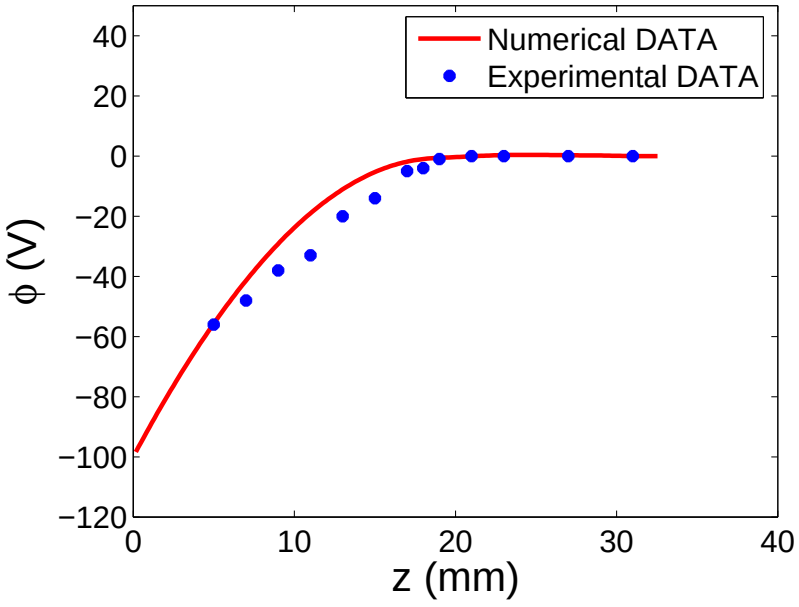

Figure 3.12: Comparison of measurements (point) and numerical simulation (solid line).

3.4 Charging Model

This section presents the charging model developed in this dissertation. A charging model is incorporated into the PIC code to calculate spacecraft floating potential. The charging on the surface is determined directly from deposited charges on the surface. To obtain the charge redistribution on a conductive object, the classical capacitance matrix technique [7, 8, 2, 32] is applied. We treat the object as part of the simulation domain and the potential on the object is calculated directly from the charges deposited on the surface. The local potential is determined by the charges stored on each node of the surface and then it can be obtained by solving the Poisson's equation:

$$\nabla \cdot (\varepsilon_0 \varepsilon_r \nabla \phi) = -\rho \tag{3.10}$$

where ε_r and ε_0 are the dielectric constant and the permittivity of the free space, respectively.

3.4.1 Charging Model for a Thin Plate

Fig. 3.13 shows the discretization in the simulation domain including a thin platform. The finite difference equation for the Poisson's equation is given by

$$\begin{aligned} &\frac{\varepsilon\phi_{i+1,j,k} - 2\varepsilon\phi_{i,j,k} + \varepsilon\phi_{i-1,j,k}}{\triangle x^2} + \frac{\varepsilon\phi_{i,j+1,k} - 2\varepsilon\phi_{i,j,k} + \varepsilon\phi_{i,j-1,k}}{\triangle y^2} \\ + \quad &\frac{\varepsilon_0\phi_{i,j,k+1} - 2\varepsilon\phi_{i,j,k} + \varepsilon_0\phi_{i,j,k-1}}{\triangle z^2} = -\rho_{i,j,k} \end{aligned} \tag{3.11}$$

where $\varepsilon(= \varepsilon_0\varepsilon_r)$ are the permittivity of the material. Table 3.2 provides the dielectric constant associated with the materials used in real space missions.

In the PIC code, after the charged particles are deposited on a surface, we solve the Poissons equation for each node on the surface using the deposited charges. On a conducting material, the deposited charges on the surface are redistributed, resulting in equipotential over the

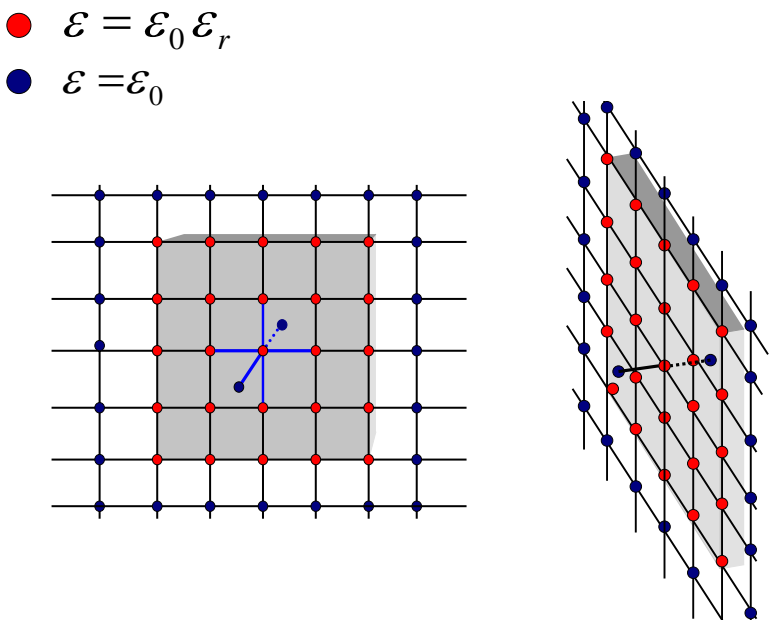

Figure 3.13: Discretization in the interface of the dielectric material.

entire surface. In this study, the classical capacitance matrix method is applied to calculate the charge redistribution on the conducting surface. To construct the capacitance matrix [7, 8, 2, 32] one first places a unit surface charge on each surface node in turn and solve the Poisson's equation. The potential vector $\phi_{s,i}, (i = 1\ N)$ for the unit surface charge for i-row gives the j-column of the matrix A as shown below.

$$\begin{bmatrix} \phi_{s,1} \\ . \\ . \\ \phi_{s,i} \\ . \\ . \\ \phi_{s,N} \end{bmatrix} = \begin{bmatrix} \cdot & A_{1,j} & \cdot \\ \cdot & \cdot & \cdot \\ \cdot & \cdot & \cdot \\ \cdot & A_{i,j} & \cdot \\ \cdot & \cdot & \cdot \\ \cdot & \cdot & \cdot \\ \cdot & A_{N,j} & \cdot \end{bmatrix} \cdot \begin{bmatrix} 0 \\ . \\ . \\ 1 \\ . \\ . \\ 0 \end{bmatrix}$$

The capacitance matrix C is found by the inversion of capacitance matrix A. We simply

Table 3.2: Dielectric constant for material properties.

Parameter	ε_r
Borosilicate Glass	6.7
CMX Glass	3.8
Kapton	3.45
ETFE	2.5
Teflon	2.15

apply the LU decomposition method to perform the inversion of the matrix. Then, the redistribution of the deposited charge is determined using the capacitance matrix C. Since the surface potential is constant, we can obtain the desired potential using the following matrix form:

$$\begin{bmatrix} \cdot & C_{1,j} & \cdot \\ \cdot & \cdot & \cdot \\ \cdot & \cdot & \cdot \\ \cdot & C_{i,j} & \cdot \\ \cdot & \cdot & \cdot \\ \cdot & \cdot & \cdot \\ \cdot & C_{N,j} & \cdot \end{bmatrix} \cdot \begin{bmatrix} \phi_{s,1} \\ \cdot \\ \cdot \\ \phi_{s,i} \\ \cdot \\ \cdot \\ \phi_{s,N} \end{bmatrix} = \begin{bmatrix} \cdot & C_{1,j} & \cdot \\ \cdot & \cdot & \cdot \\ \cdot & \cdot & \cdot \\ \cdot & C_{i,j} & \cdot \\ \cdot & \cdot & \cdot \\ \cdot & \cdot & \cdot \\ \cdot & C_{N,j} & \cdot \end{bmatrix} \cdot \begin{bmatrix} 1 \\ \cdot \\ \cdot \\ 1 \\ \cdot \\ \cdot \\ 1 \end{bmatrix} \quad \phi^* = \begin{bmatrix} q_1 \\ \cdot \\ \cdot \\ q_i \\ \cdot \\ \cdot \\ q_N \end{bmatrix}$$

Finally, the desired potential ϕ^* can be determined by

$$\phi^* = \frac{\sum_{i=1}^{N} q_i}{\sum_{i=1}^{N} \sum_{j=1}^{N} C_{i,j}} \tag{3.12}$$

Then, the correction term for charge redistribution can be found by using the difference between the desired potential ϕ^* and the potential ϕ obtained by solving the Poisson's equation as follows:

$$\delta q = C(\phi^* - \phi) = C(\delta\phi) \tag{3.13}$$

The Poisson's equation is solved again after the correction term is added to the source term of charges:

$$\nabla^2\phi = -(\rho + \delta q)/\varepsilon \tag{3.14}$$

Finally, the potential of the conducting surface can be obtained, resulting in uniform potential on the surface. Fig. 3.14 represents the capacitance matrix calculated for a thin plate using the capacitance matrix technique. It shows that the capacitance matrix is symmetric and positive definite.

3.4.2 Charging Model for a Spacecraft

We next consider a more complex configuration. We model the spacecraft as a combination of a solid box made of dielectric or conducting materials and thin plates. The local potential on the object is directly calculated using the deposited charges on each node. The Poisson's equation on the spacecraft can be discretized using finite difference equation.

$$\begin{aligned} &\frac{\varepsilon\phi_{i+1,j,k} - 2\varepsilon\phi_{i,j,k} + \varepsilon\phi_{i-1,j,k}}{\triangle x^2} + \frac{\varepsilon\phi_{i,j+1,k} - 2\varepsilon\phi_{i,j,k} + \varepsilon\phi_{i,j-1,k}}{\triangle y^2} \\ + &\frac{\varepsilon\phi_{i,j,k+1} - 2\varepsilon\phi_{i,j,k} + \varepsilon\phi_{i,j,k-1}}{\triangle z^2} = -\rho_{i,j,k} \end{aligned} \tag{3.15}$$

Fig. 3.15 shows the discretization associated with a spacecraft. If the spacecraft surface is conductive, we apply the capacitance matrix technique to calculate the charge re-distribution. It is necessary to obtain the corresponding capacitance matrix for the desired geometry since the capacitance matrix only depends on the geometry of an object. To generate the capacitance matrix for each desired object, we solved the Poisson's equation by placing a unit charge on the nodes designated as objects. While obtaining the matrix, special attention is required on the computer memory since the dimensions of the capacitance matrix are $N_x \times N_x$ where N_x is the total grid number of a spacecraft. The basic principle to calculate charge re-distributions on the desired object is described in the previous section. In this study, we consider two different types of electrical connections. In case I, we consider that

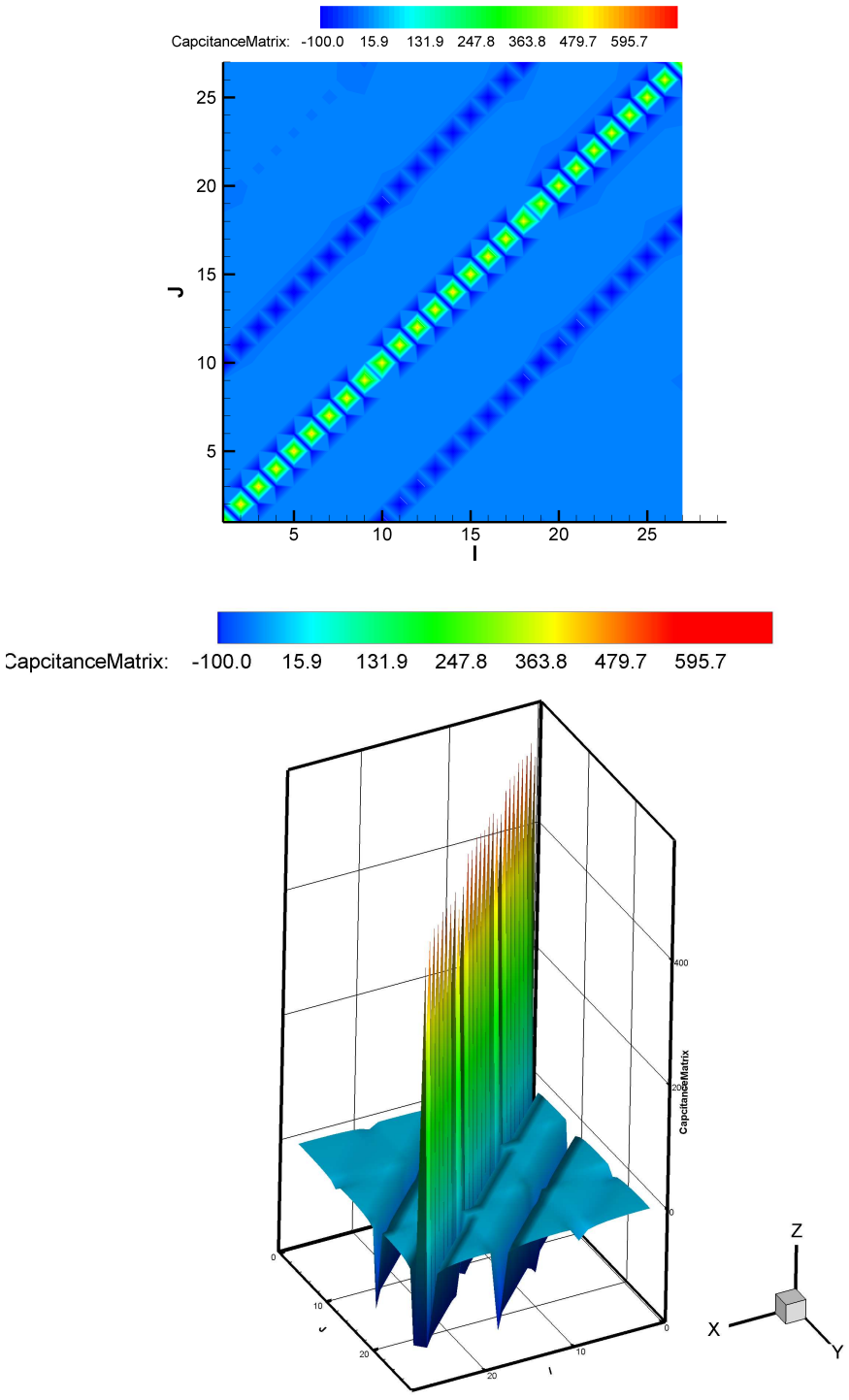

Figure 3.14: Capacitance matrix for a thin plate

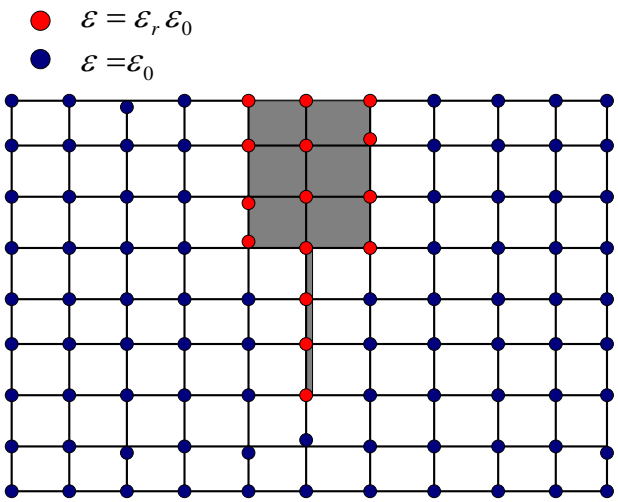

Figure 3.15: Discretization for a spacecraft.

a main body and a solar panel are disconnected electrically and hence the main body and the panel may have a different floating potential. In case II, we consider that a main body and a solar panel is connected electrically and so the main body and the panel has the same floating potential. In case I, the deposited charges are re-distributed separately on a main body and a solar panel and hence the capacitance matrices corresponding to each rectangular body and thin plate should be calculated. In case II, the charges are redistributed between a main body and a solar panel and hence case II requires only one capacitance matrix. In this work, the simulations are performed only on a quarter of the spacecraft due to the symmetric geometry of the object, This requires to calculate two capacitance matrices for case I and one matrix associated with a main body and a solar panel for case II. Figs. 3.16 - 3.17 provides the capacitance matrices the main body and the solar panel of case I. Fig. 3.18 shows the capacitance matrix corresponding to case II. As expected, those obtained capacitance matrices are symmetric and positive definite. Fig. 3.19 describes the algorithm used in the charging model. We summarize the model algorithm related to the spacecraft charging.

1. Calculate and save the capacitance matrix corresponding to the desired geometry of a spacecraft at the initial time.
2. Inject ambient plasma on the boundaries.
3. If sunlight, inject photoelectrons on a sunlit object surface.
4. Simulate plasma flow for three species: ambient electrons, ambient ions, and photoelectrons.
5. Deposit the charges for particles hitting on the object surface on each node.
6. Calculate the potential by solving the Poisson's equation for both a domain and an object surface.
7. Obtain charge re-distribution on the object surface using the obtained capacitance matrix.
8. Solve the Poisson's equation again.
9. Repeat step 2 through 7 until a simulation reaches to steady state.

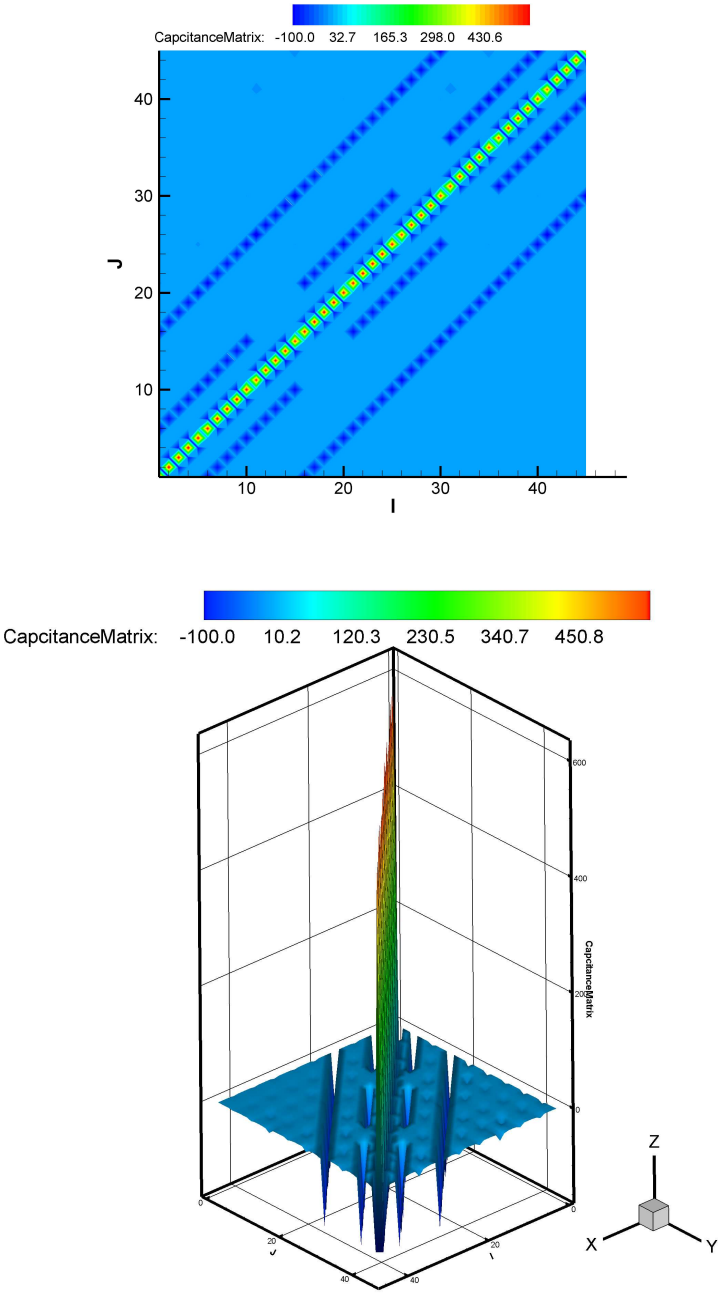

Figure 3.16: Capacitance matrix for a main body corresponding to case I.

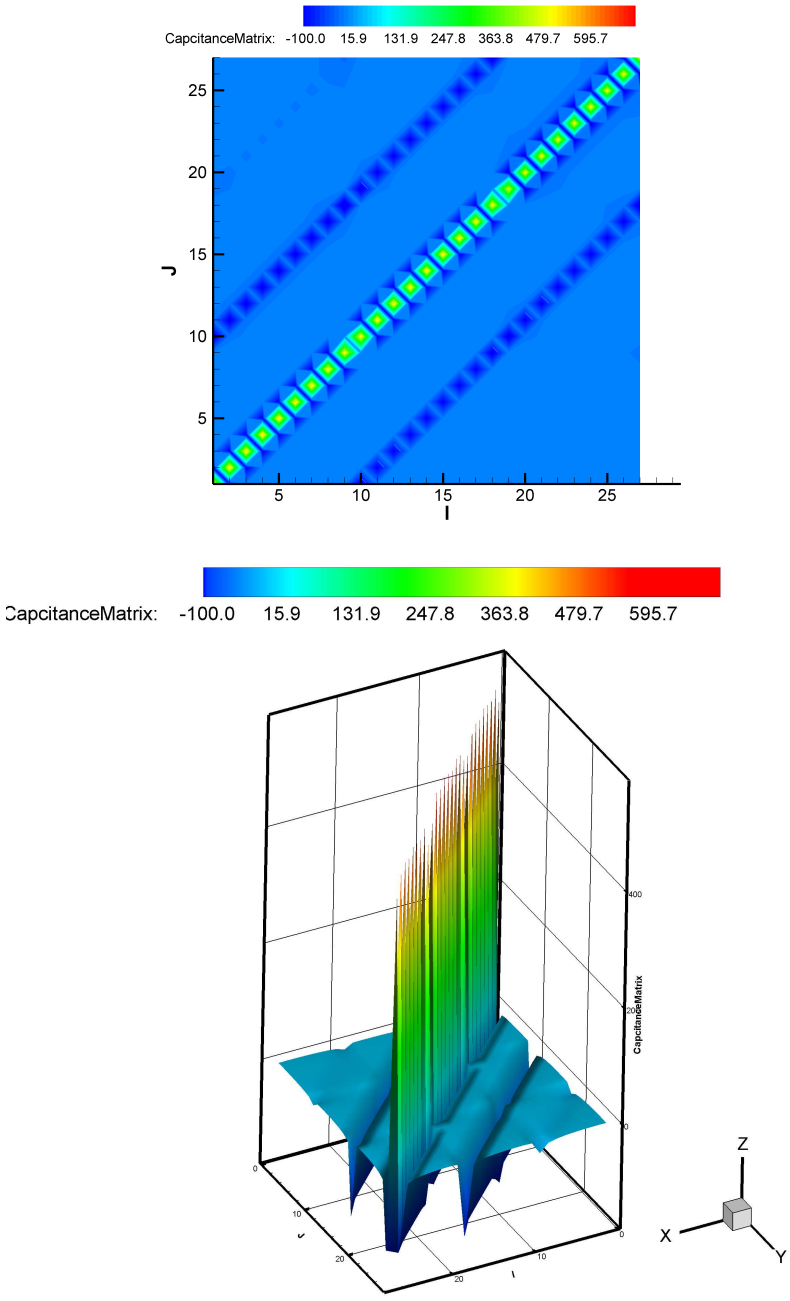

Figure 3.17: Capacitance matrix for a solar panel corresponding to case I.

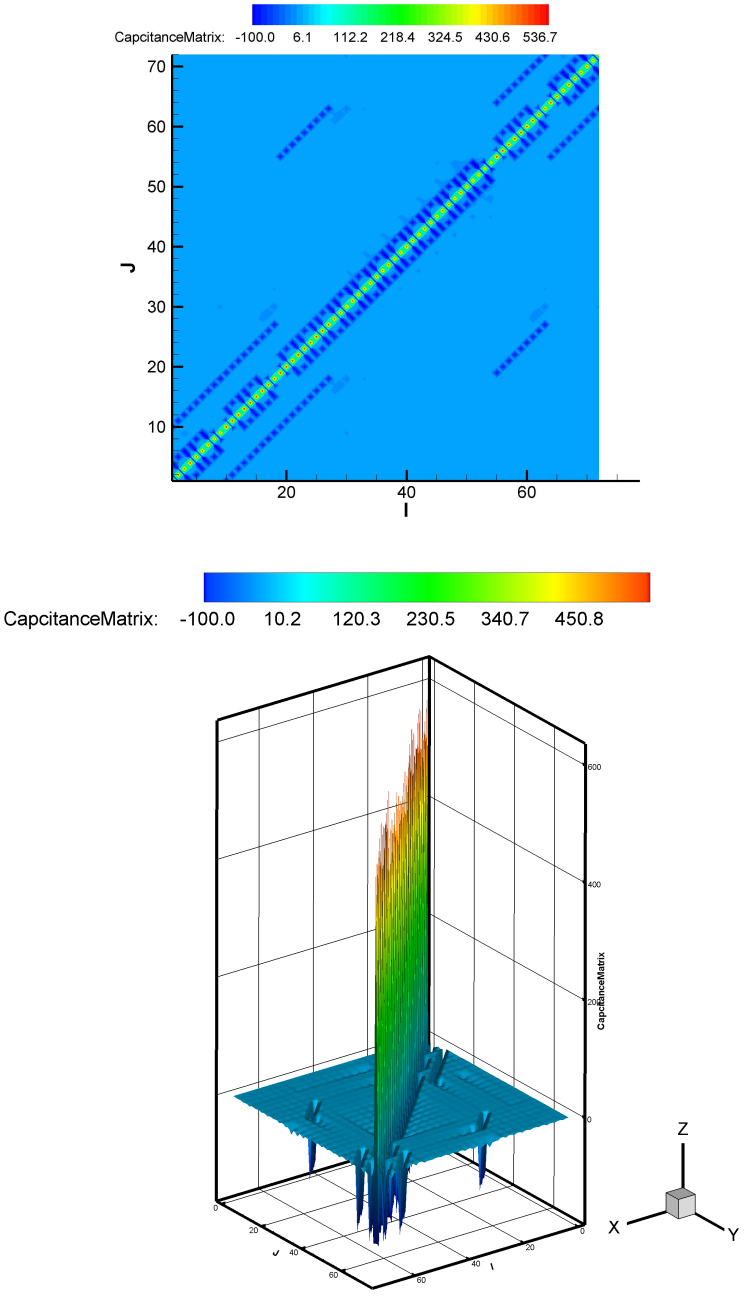

Figure 3.18: Capacitance matrix for the entire spacecraft corresponding to case II.

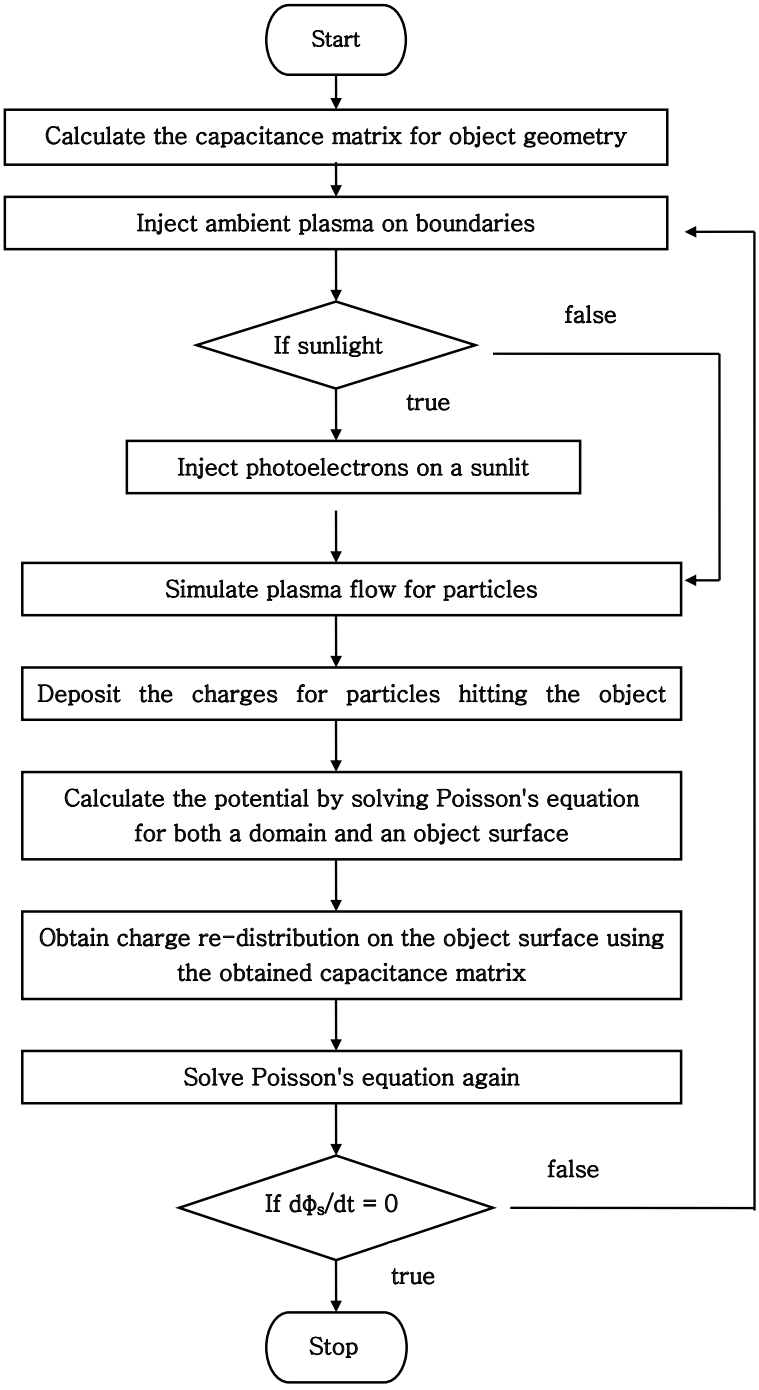

Figure 3.19: Flowchart of a spacecraft charging model.

Chapter 4

Results and Discussions

4.1 Solar Wind Interactions with a Thin Plate

4.1.1 Thin Plate with Fixed Surface Potential

This section presents the simulation of solar wind interactions with a thin plate. We first consider the situation where the plate surface potential is an input to the PIC code. Here, the plate potential is obtained using the analytical approach described in Chapter 2. The solar wind and photoelectron emission parameters used in the simulation are given in Table 2.1. For the results presented here, the plate size is taken to be $1\lambda_d \times 1\lambda_d$ where $\lambda_d (= 15.4m)$ is the solar wind plasma Debye length. The simulation domain is taken to be $3.5\lambda_d \times 3.5\lambda_d \times 7.5\lambda_d$. The cell size is taken to be $\Delta x = \Delta y = \Delta z = 0.1\lambda_d$. The cell resolution corresponds to $1.3\lambda_{ph}$, $0.9\lambda_{ph}$, and $0.7\lambda_{ph}$ for $T_{ph} = 1eV$, $T_{ph} = 2eV$, and $T_{ph} = 4eV$, respectively. The time step is calculated from the cell size and the maximum velocity for particles at each time step. The number of macro-particles used is $\sim$ 50 per cell for each species. The simulation is performed using the real ion to electron mass ratio $m_i/m_e = 1836$ in order to maintain the correct mesothermal velocity ratio.

In PIC simulation presented here, all plasma species (ambient ions and electrons, and pho-

toelectrons) are modeled as macro-particles. Figure 4.1 shows the density distribution of ion, electron, photoelectron, and total charge densities, respectively. Figure 4.2 shows the potential contour on a $y-z$ plane and a 1-D potential profile along $y=0$ for $T_{ph}=2eV$. As shown in the figure, the non-monotonic potential profile develops in front of the sunlit surface. Figure 4.3 shows the 1-D potential profile along $y=0$ on the $y-z$ plane for $T_{ph}=1eV$, $T_{ph}=2eV$, and $T_{ph}=4eV$, respectively. Fig. 4.4 shows a comparison of the potential profiles obtained from the numerical simulation and predicted by the analytical method. The black solid line, dashed line, dotted line indicate the numerical solution, non-monotonic analytical solution, and monotonic analytical solution, respectively. It is found that the numerical results agree well with the non-monotonic potential profiles obtained from the analytical method. The simulation results suggest that the non-monotonic potential profile is the physical solution for given parameters between two analytical solutions obtained in Chapter 2 [18, 69]. Table 4.1 shows the comparison of surface floating potential ϕ_0, potential minimum ϕ_m, and the distance between the minimum potential and the plate r_m.

We next examine the detailed electron dynamics in the photoelectron sheath. Using the potential obtained from PIC simulation, we can easily calculate the minimum velocity required for the ambient electrons and the photoelectrons to overcome the potential barrier in the photoelectron sheath. Table 4.2 shows the minimum velocity for different photoelectron temperatures where $v_{m,0}$ and $v_{m,\infty}$ indicate the velocities for photoelectrons and plasma electrons, respectively. In order to obtain the velocity distribution for photoelectrons, we separate the photoelectron sheath into two regions as shown in Fig. 4.5: the inside (region I) and the outside (region II) of the potential barrier. Here, region I and region II are defined as $z_m < z < z_o$ and $z_\infty < z < z_m$, respectively where z_∞, z_m, and z_o indicate infinity, position of potential minimum, and position of the plate. Figures 4.6 and 4.7 show the velocity distribution of photoelectrons with $T_{ph}=1eV$ and $T_{ph}=4eV$, respectively. The presented distributions are obtained in the range of $0<x<R$ and $0<y<R$ where $R(=1\lambda_d)$ is the plate dimension. Velocity distributions (region I) show that low energy photoelectrons ($-v_{m,0}<v<v_{m,0}$) are captured by the potential barrier where $v_{m,0}\sim 0.36$ for $T_{ph}=1eV$

and $v_{m,0} \sim 0.69$ for $T_{ph} = 4eV$. The distributions (region II) show that relatively high energy photoelectrons ($v > v_{m,0}$) overcome the potential barrier.

In Figure 4.8 and Figure 4.9, we compare the phase space plot for photoelectrons in the entire simulation domain (left) with that for a subdomain of $0 < x < R$ and $0 < y < R$ (right). It can be seen that some photoelectrons are pushed by electric field within the sheath and back flow to the wake side of the plate.

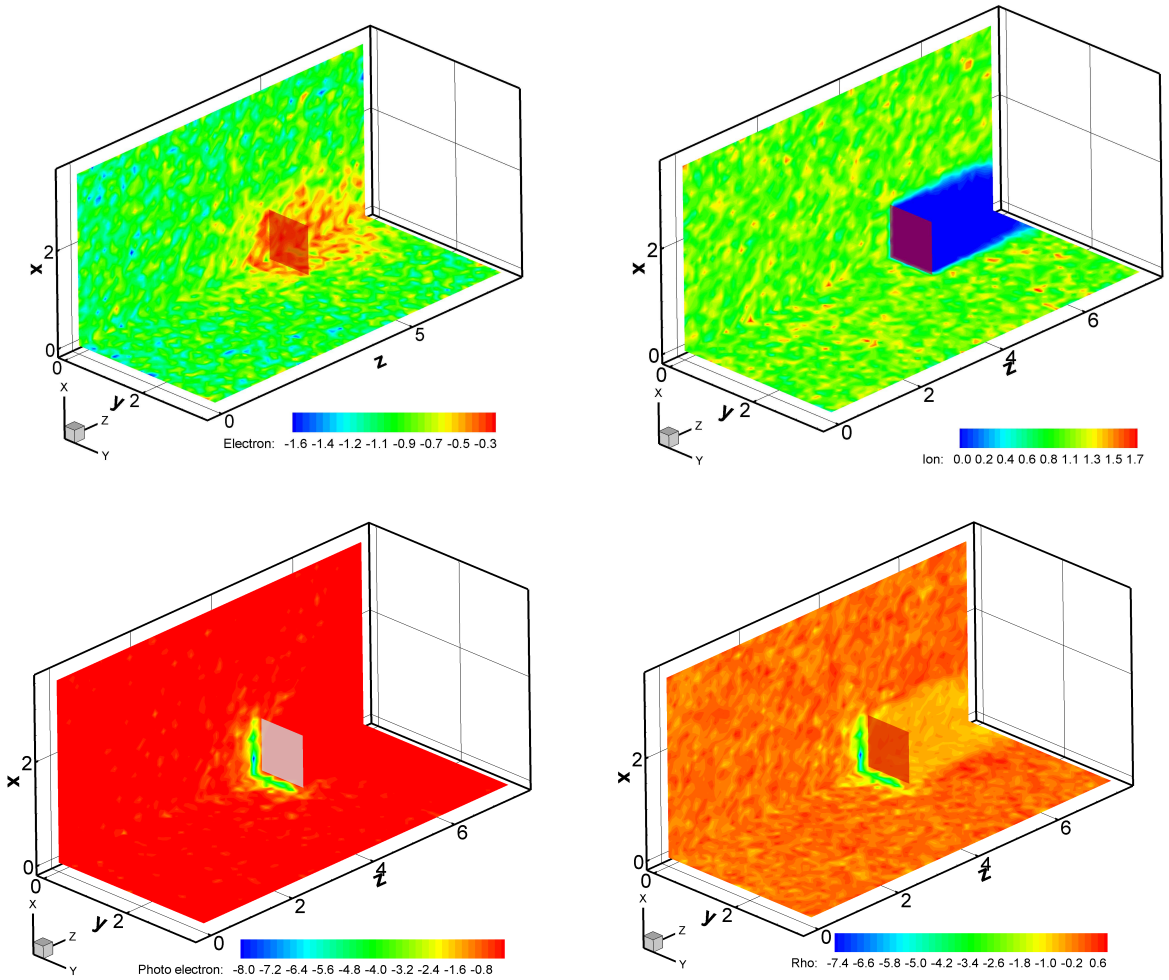

Figure 4.1: Density distributions for electron, ion, photoelectron, and total charge.

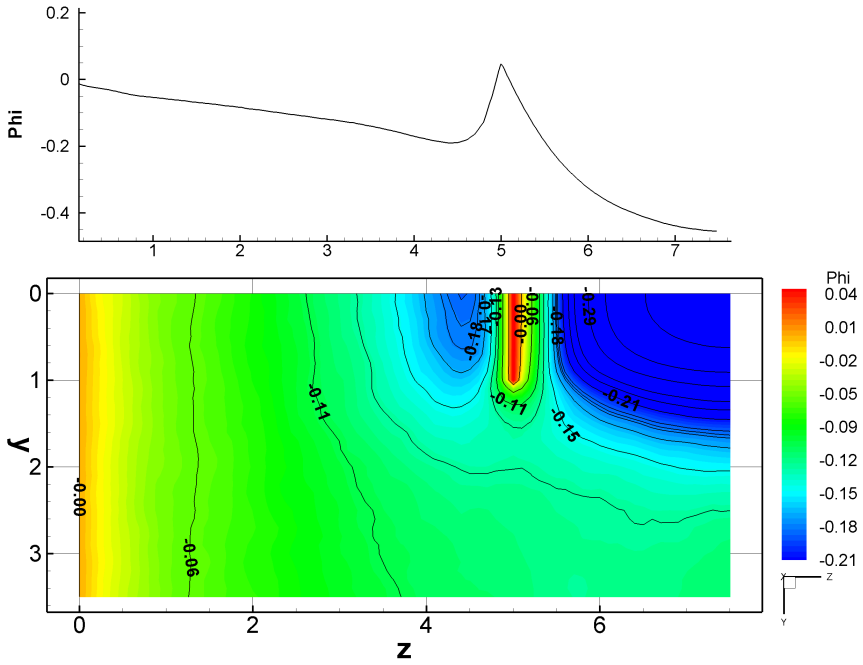

Figure 4.2: 1-D potential profile along $y = 0$ on a $y - z$ plane where potential is normalized by $T_e = 15eV$ and z is normalized by $\lambda_d = 15.4m$ for $T_{ph} = 2eV$.

Table 4.1: Comparison of surface floating potential ϕ_0, potential minimum ϕ_m, distance between minimum potential and a plate r_m for drifting electrons where surface floating potential is obtained from the theoretical method.

T_{ph}, eV	$1eV$	$2eV$	$4eV$
ϕ_0, V	-2.24	0.77	6.36
ϕ_m, V	-4.19	-2.73	-0.82
r_m, m	5.1	7.4	16.76

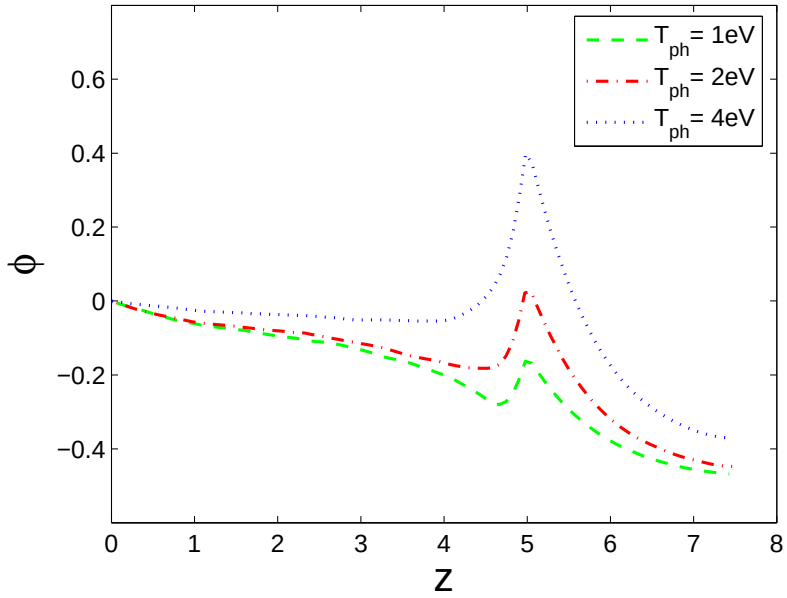

Figure 4.3: 1-D potential profile along $y = 0$ on a $y - z$ plane where potential is normalized by $T_e = 15eV$ and z is normalized by $\lambda_d = 15.4m$.

Table 4.2: Comparison of the minimum velocity for ambient electrons and photoelectrons to overcome a potential barrier. Velocity is normalized by electron thermal energy.

T_{ph}, eV	$1eV$	$2eV$	$4eV$
$v_{m,0}$	0.36	0.48	0.69
$v_{m,\infty}$	0.53	0.43	0.23

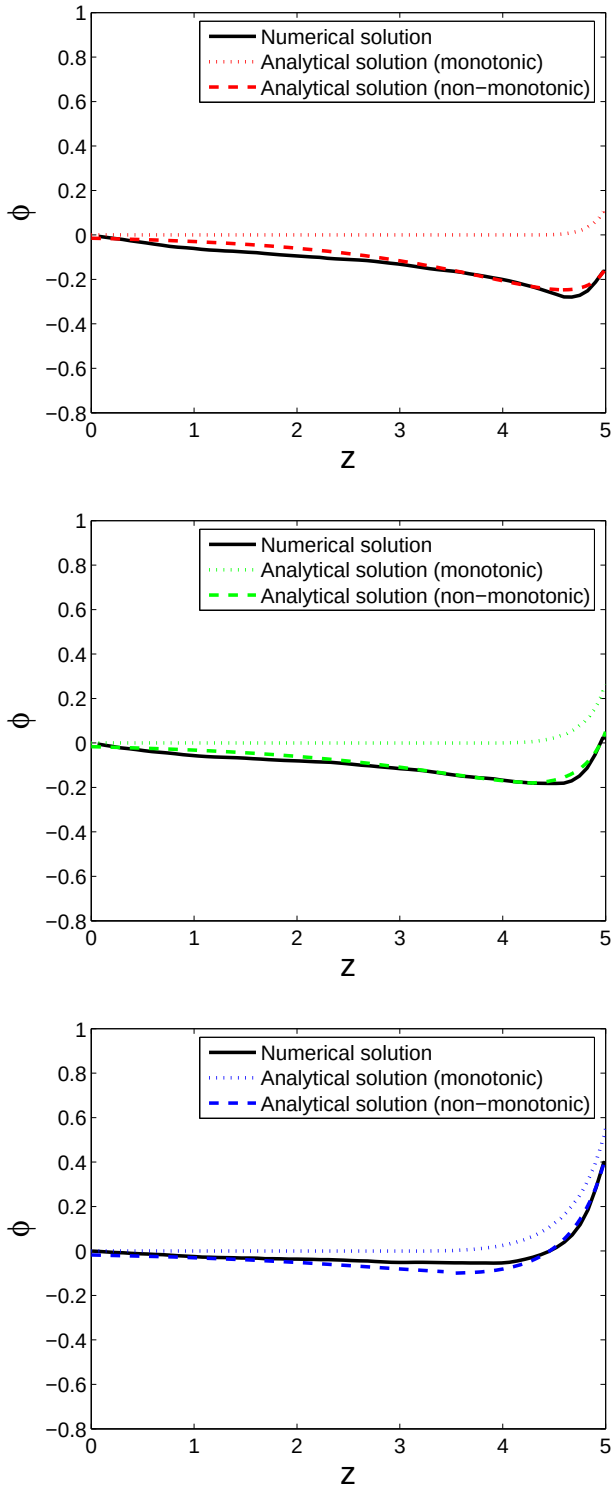

Figure 4.4: Comparison of the potential profiles obtained from numerical simulation and predicted by the analytical method for $T_{ph} = 1eV$ (top), $T_{ph} = 2eV$ (middle), and $T_{ph} = 4eV$ (bottom). Potential is normalized by $T_e = 15eV$ and z is normalized by $\lambda_d = 15.4m$.

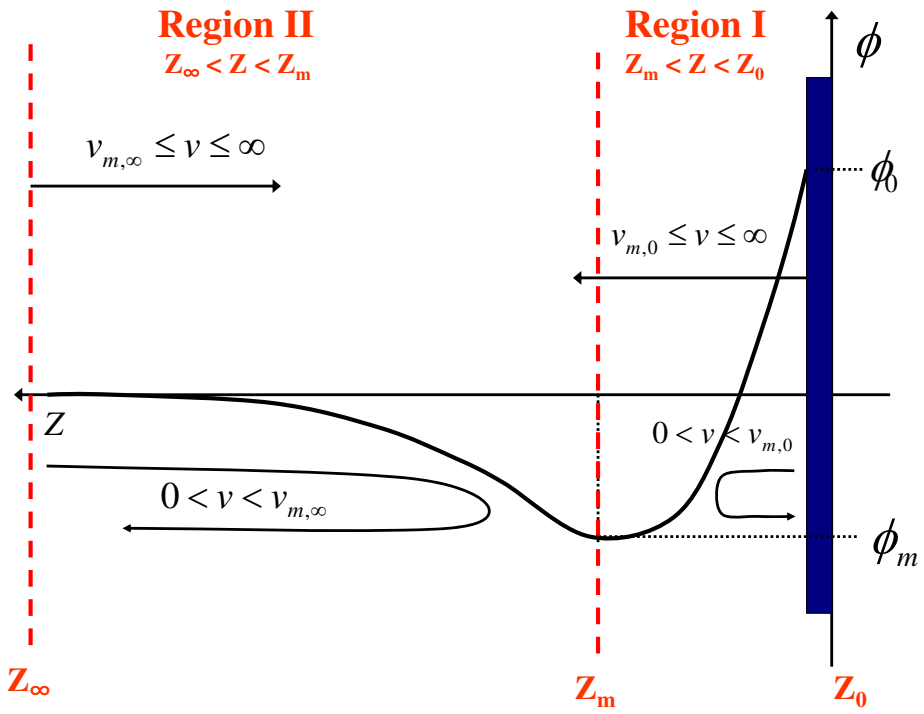

Figure 4.5: Schematics for region I and region II to obtain velocity distributions.

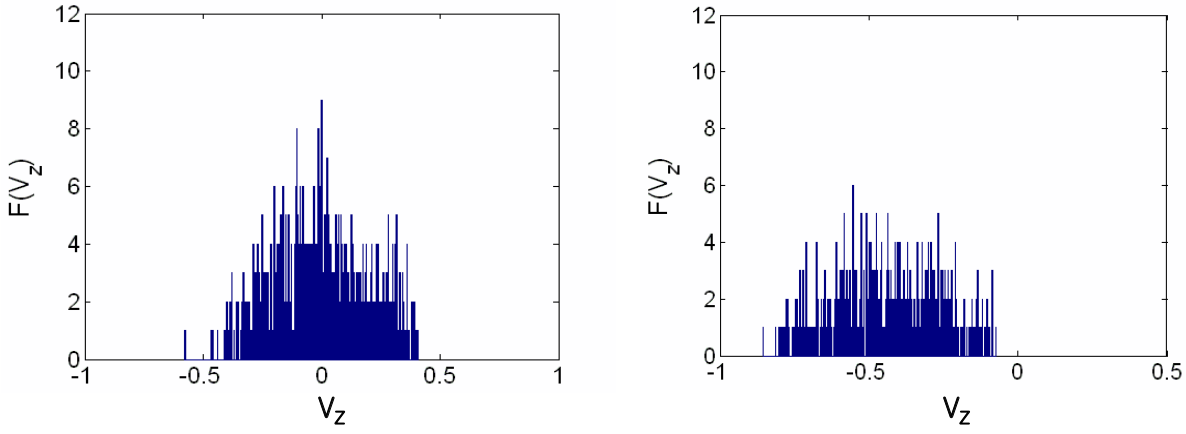

Figure 4.6: Velocity distribution for photoelectrons at region I, $z_m < z < z_o$ (left) and at region II, $z_\infty < z < z_m$ (right) for $T_{ph} = 1eV$ where z_∞, z_m, and z_o indicate infinity, position of potential minimum, and position of the plate. The presented distributions are obtained in the range of $0 < x < R$ and $0 < y < R$ where $R(= 1\lambda_d)$ is the plate dimension.

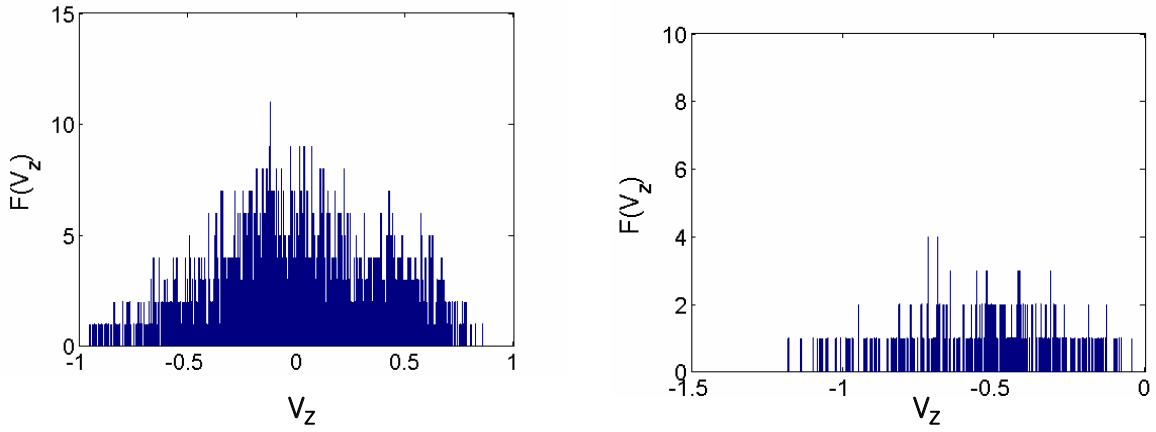

Figure 4.7: Velocity distribution for photoelectrons at region I, $z_m < z < z_o$, (left) and at region II,$z_\infty < z < z_m$ (right) for $T_{ph} = 4eV$ where z_∞, z_m, and z_o indicate infinity, position of potential minimum, and position of the plate. The presented distributions are obtained in the range of $0 < x < R$ and $0 < y < R$ where $R(= 1\lambda_d)$ is the plate dimension.

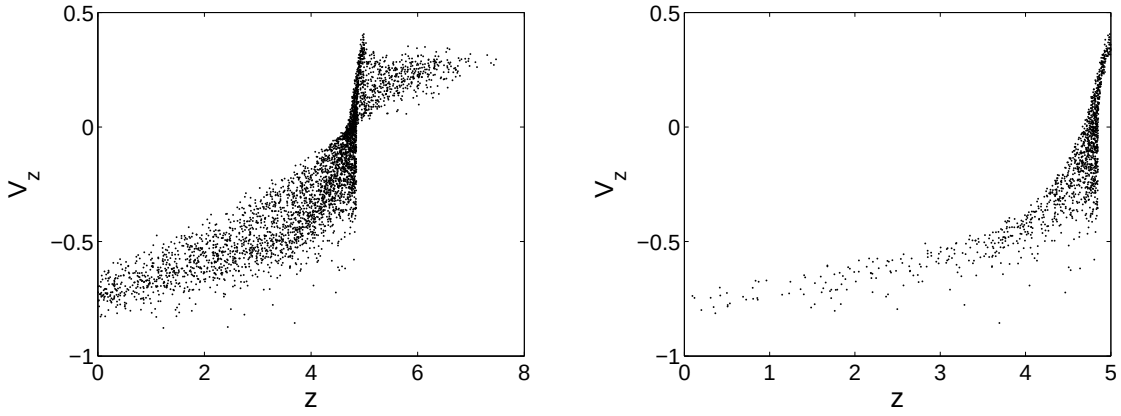

Figure 4.8: Photoelectron phase space plot in $z - V_z$ with respect to $T_{ph} = 1eV$ in whole domain (left) and in the range of $0 < x < R$ and $0 < y < R$ (right) where $R(= 1\lambda_d)$ is the plate dimension.

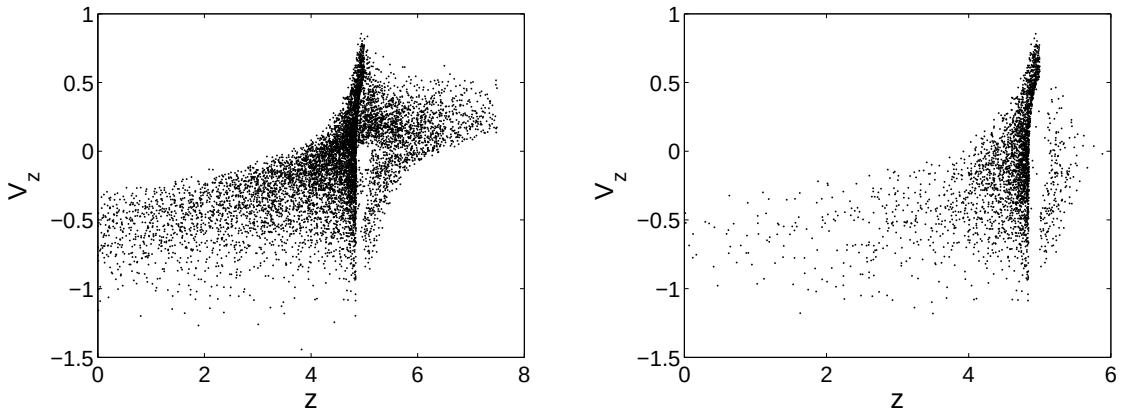

Figure 4.9: Photoelectron phase space plot in $z - V_z$ with respect to $T_{ph} = 4eV$ in whole domain (left) and in the range of $0 < x < R$ and $0 < y < R$ (right) where $R(= 1\lambda_d)$ is the plate dimension.

4.1.2 Thin Plate with Floating Surface Potential

Thin Plate Charging

We next consider the situation where the plate surface potential is floating. The floating potential is obtained self-consistently from deposited charges on the object surface using the charging model in the Chapter 3.4. For the results presented here, the plate size is taken to be $1\lambda_d \times 1\lambda_d$, where $\lambda_d (= 15.4m)$ is the solar wind plasma Debye length. The simulation domain is taken to be $3.5\lambda_d \times 3.5\lambda_d \times 7.5\lambda_d$. The cell resolution is taken to be $\Delta x = \Delta y = \Delta z = 0.1\lambda_d$. The cell resolution corresponds to $1.3\lambda_{ph}$, $0.9\lambda_{ph}$, and $0.7\lambda_{ph}$ for $T_{ph} = 1eV$, $T_{ph} = 2eV$, and $T_{ph} = 4eV$, respectively. Table 2.1 shows the parameters used in this simulation. Fig. 4.10 shows the surface floating potentials obtained from the charging simulations for a dielectric thin plate and conductive thin plate ($\varepsilon_r = 1$). Fig. 4.11 shows the surface charge distribution for each material. Fig. 4.12 shows the electric potential profile on a $y-z$ plane for $T_{ph} = 1eV$, $T_{ph} = 2eV$, and $T_{ph} = 4eV$ respectively in a conductive plate. The PIC simulation shows that a non-monotonic sheath profile is generated by photoelectron emissions. It also shows the plasma wake is formed by the drifting plasma. Fig. 4.13 shows a 1-D potential plot cutting through a plane center of a $y-z$ plane (top) and comparison with analytical solutions (bottom). Fig. 4.14 shows comparison of the potential profiles obtained from numerical simulations and predicted by the analytical method for $T_{ph} = 1eV$ (top), $T_{ph} = 2eV$ (middle), and $T_{ph} = 4eV$ (bottom). We found that the obtained simulation results are similar to the non-monotonic potential profile obtained from the analytical method.

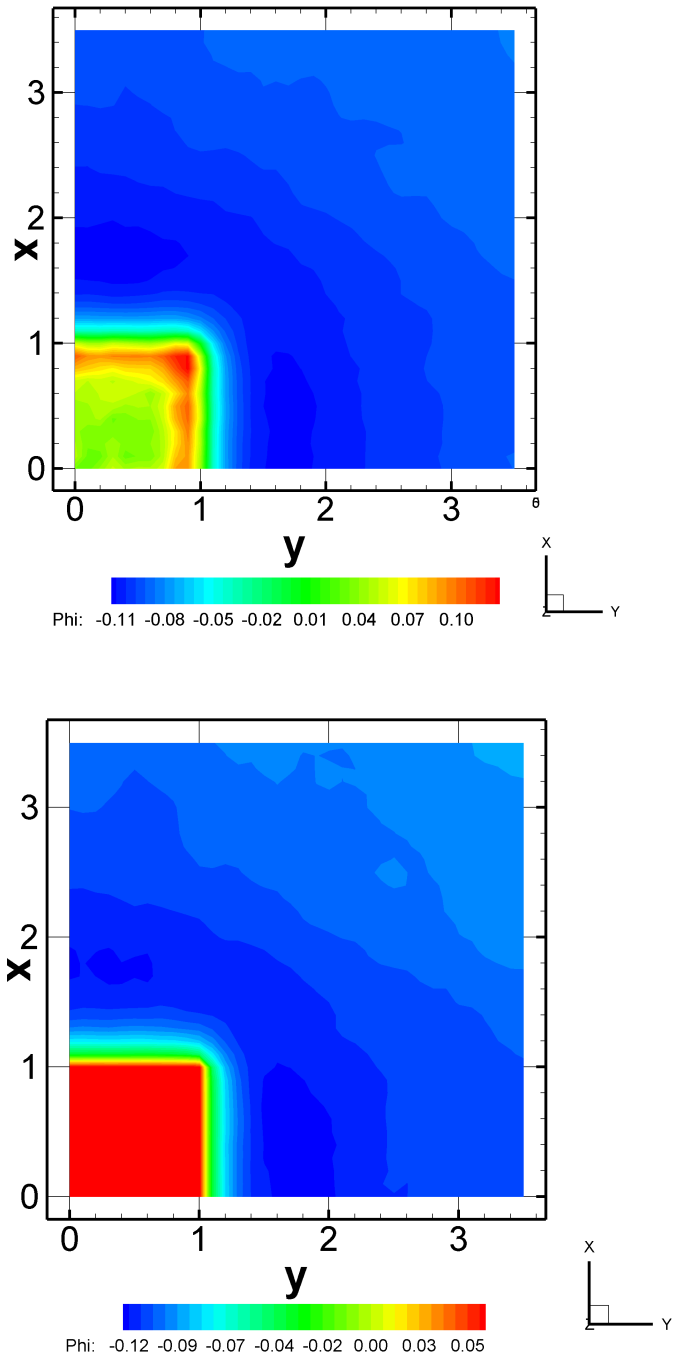

Figure 4.10: Potential contours for a dielectric thin plate (top) and conductive thin plane (bottom). Potential and distance values are normalized by $T_e = 15eV$ and electron Debye length $\lambda_d = 15.4m$, respectively.

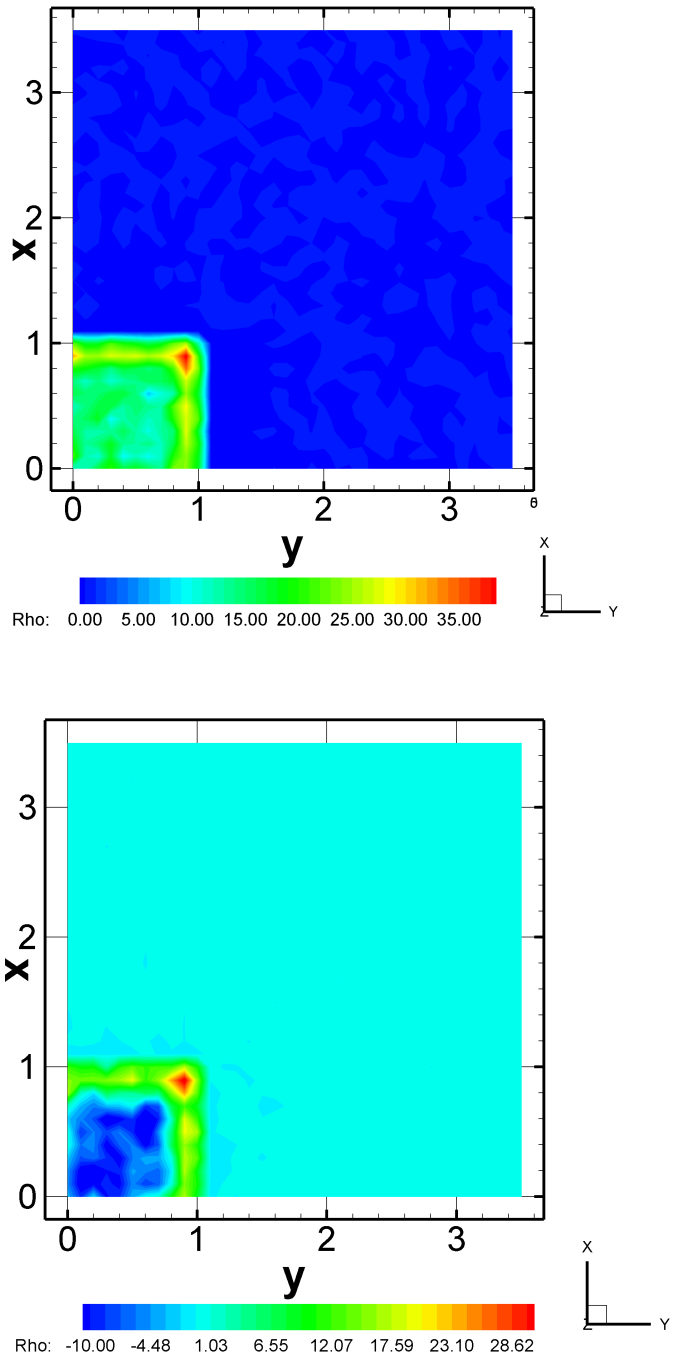

Figure 4.11: Charge density contours for a dielectric thin plate (top) and conductive thin plane (bottom). Density and distance are normalized by electron density n_e and electron Debye length $\lambda_d = 15.4m$, respectively.

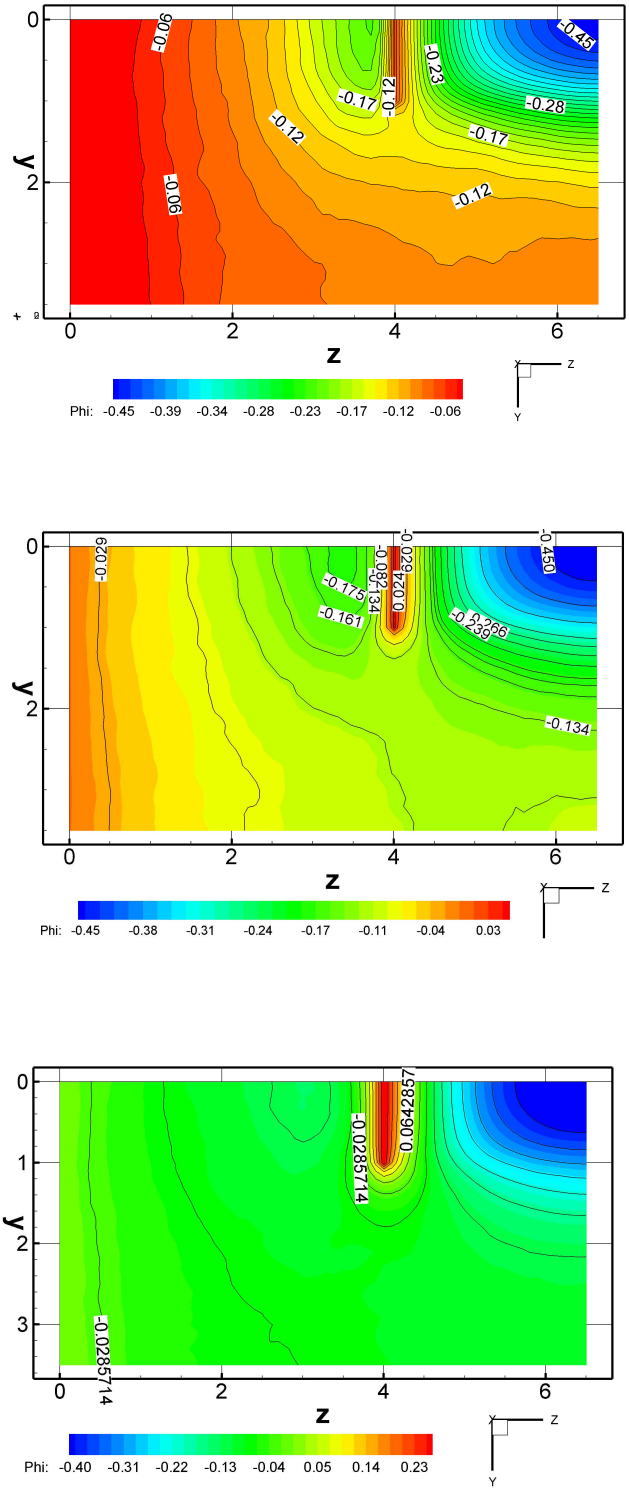

Figure 4.12: Electric potential profile on a $y-z$ plane for $T_{ph} = 1eV$ (top), $T_{ph} = 2eV$ (middle), and $T_{ph} = 4eV$ (bottom). Potential and distance are normalized by $T_e = 15eV$ and $\lambda_d = 15.4m$, respectively.

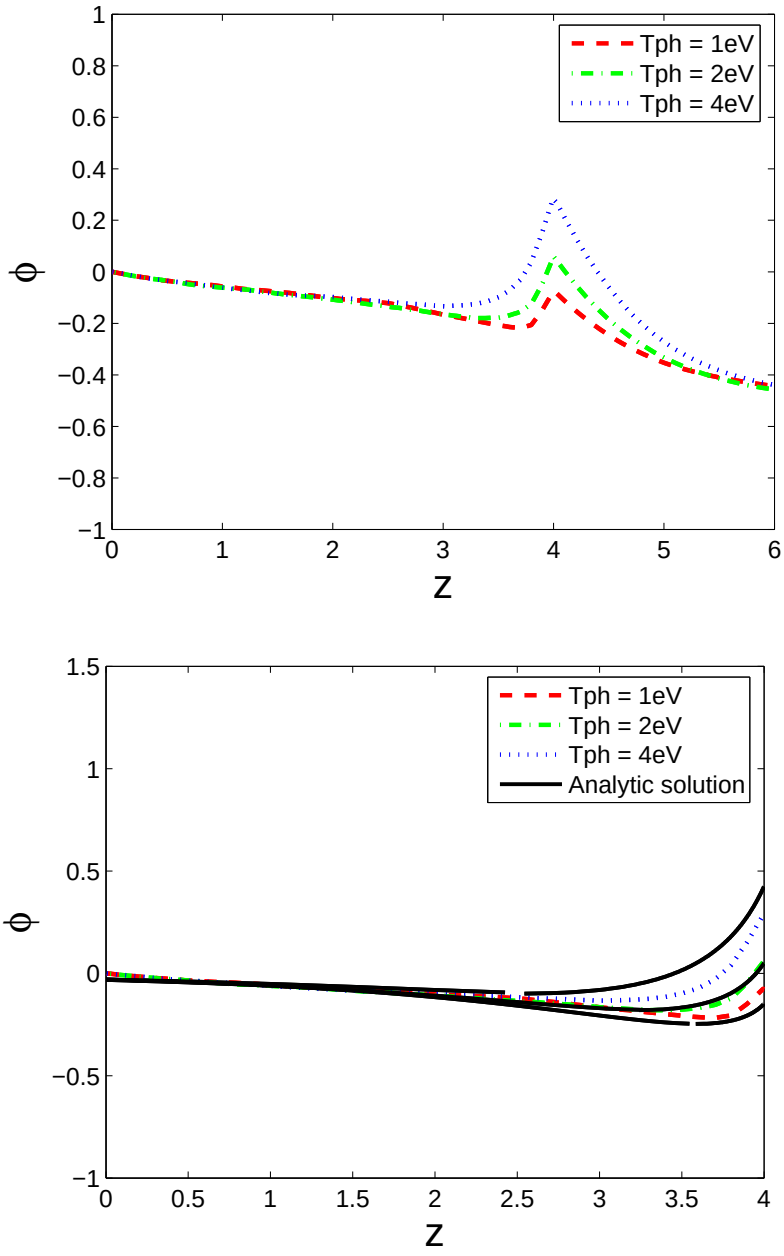

Figure 4.13: 1-D potential plot cutting through a plane center of a $y-z$ plane (top) and comparison with analytic solutions (bottom). Potential and distance are normalized by $T_e = 15eV$ and $\lambda_d = 15.4m$, respectively.

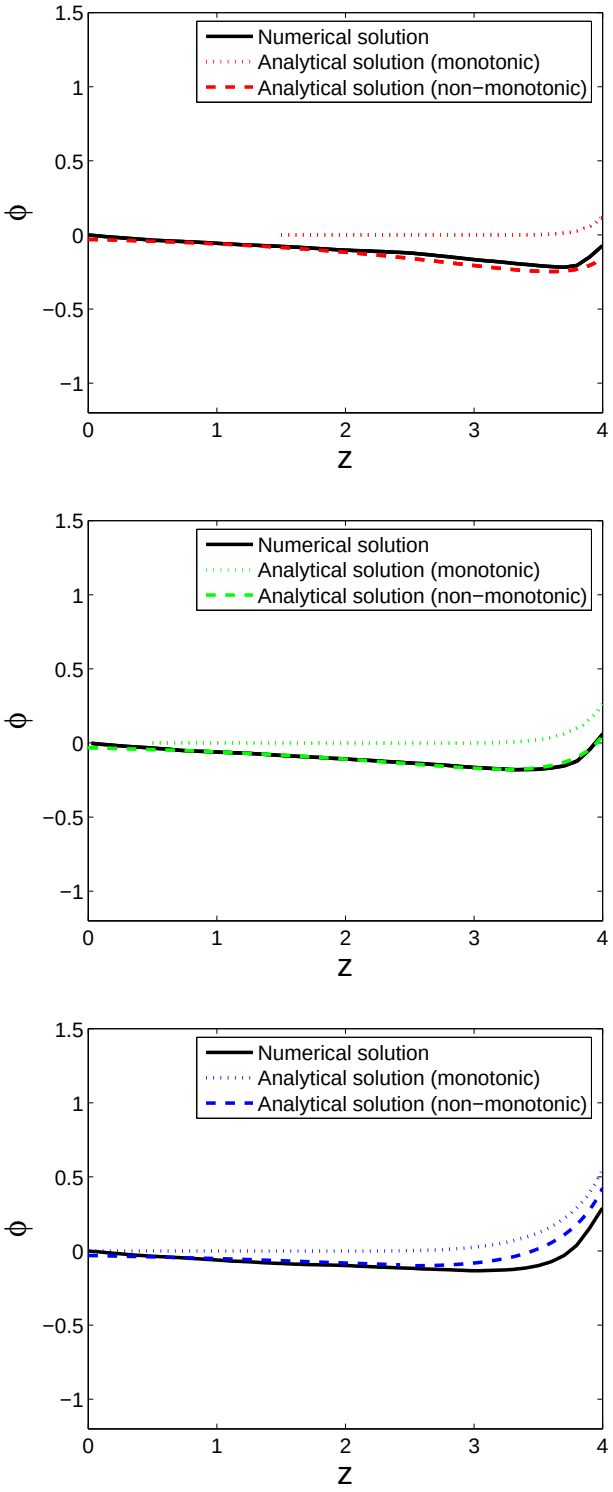

Figure 4.14: Comparison of the potential profiles obtained from numerical simulation and predicted by the analytical method for $T_{ph} = 1eV$ (top), $T_{ph} = 2eV$ (middle), and $T_{ph} = 4eV$ (bottom). Potential is normalized by $T_e = 15eV$ and z is normalized by $\lambda_d = 15.4m$.

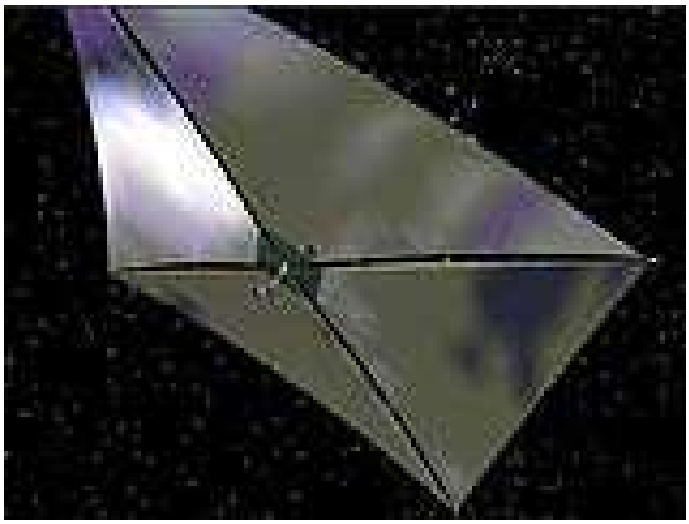

Figure 4.15: Solar sail spacecraft for future interplanetary missions.

Solar Sail Charging

Solar sail is a new advanced propulsion technology for future interplanetary missions. A number of solar sail missions with various sail designs have been considered in recent years. An important issue in the implementation of a solar sail system is the effect of plasma interaction between solar wind and the sail. In a previous study, Garrett and Wang presented a particle-in-cell (PIC) simulation model for solar sail and solar wind plasma interactions [22]. That model used a 2-step process. First, the floating potential of the solar sail was calculated using a 1-D current balance equation where analytical approximations were used in order to estimate the current collected by the sail. The obtained sail potential was then adopted as an input in the second step where solar wind flow around a solar sail is simulated using a 3-D hybrid electrostatic PIC code. In the model, the electrons were assumed to follow the Boltzmann approximation. Here, we revisit this problem by using fully kinetic simulation model developed in this thesis.

The focus of this study is on the effects of materials on solar sail spacecraft charging. Extensive tests have been carried out to investigate the material properties for candidate solar sail membrane materials [68]. In this work, we consider a solar sail dielectric constant and photoelectron emission property similar to that measured for Maylar. The sail dielectric constant is $\epsilon_r = 3.2$. The current density of photoelectron emissions under normal sunlight incidence is $J_{ph} = 10\mu A/m^2$ and the average temperature of the emitted photoelectrons is $T_{ph} = 2.1eV$. Assuming a Maxwellian distribution for the photoelectrons, the number density associated with photoelectrons emitted at solar sail surface is $n_{ph} \simeq 257cm^{-3}$. The mean observed solar wind parameters from [24] will be used throughout this work, and are summarized in Table 1.1 along with the basic plasma parameters relevant to this problem. The parameters for photoelectron emission are listed in Table 4.3. For the results presented in this section, we take the solar sail size to be $2\lambda_d \times 2\lambda_d$ where $\lambda_d = 8.73m$ is the solar wind plasma Debye length. Hence, in physical unit, the sail size is about $17.4m$ by $17.4m$. The simulation domain is taken to be $6\lambda_d \times 6\lambda_d \times 10\lambda_d$. The time interval is calculated from the cell size and the maximum velocity for particles at each time step. The number of macro-particles used is on average about 84 per cell for each species. In order to maintain the correct mesothermal velocity ratio, the simulation is run using the real ion to electron mass ratio, $m_i/m_e = 1836$. Fig. 4.16 shows the potential contour on the two symmetric

Table 4.3: Material properties of solar sail

Parameter	SRS
Relative dielectric constant (ε_r)	2.77 ± 1
Photoelectron yield (J_{ph}), $A \cdot m^2$	$(1 \pm 1) \times 10^{-5}$

surfaces at $x = 0$ and $y = 0$. Figure 4.17 shows the solar wind proton and photoelectron density contours and total charge density contours on the $x = 0$ plane. Figure 4.18 further shows the potential contours on the $y = 0$ plane and the 1-D potential profile along the central axis of the solar sail. These results show that the general feature of solar wind flowing around a solar sail is that of a photoelectron sheath in front of the sunlit surface followed

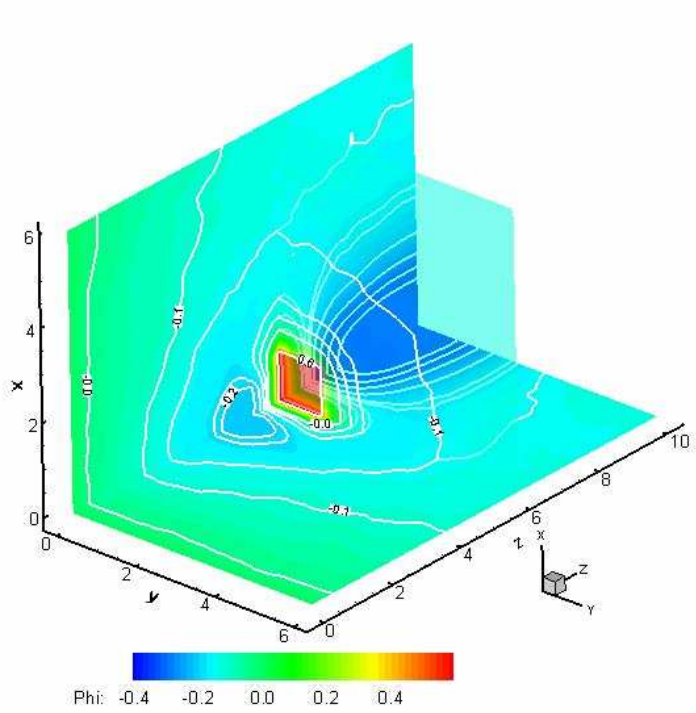

Figure 4.16: Potential contours on $x-z$ and $y-z$ planes where potential and distance values are normalized by $T_e = 12eV$ and electron Debye length $\lambda_d = 8.7m$, respectively.

by a plasma wake. Due to photoelectron emissions, the solar sail floating potential is positive with respect to the ambient plasma, $\phi_{sail} \sim 8.2V$. The photoelectron emissions also generate a non-monotonic potential profile in the photoelectron sheath. The non-monotonic potential is generated by the excessive charge caused by the photoelectron emissions. Low energy photoelectrons will be trapped by the potential barrier of the non-monotonic profile [18, 28]. Some of the low energy photoelectrons will also back flow toward the sail surface. Fig. 4.19 shows the z-direction phase space plot for photoelectrons where the trapping and back flow of photoelectrons are evident. Fig. 4.20 shows the potential distribution and charge distribution on solar sail surface. Note that the distribution of the deposited charge on the sail surface is non-uniform. However, the potential distribution is uniform as it should be for a conducting surface. Fig. 4.21 shows potential iso-surfaces where potential and distance values are normalized by $T_e = 12eV$ and electron Debye length $\lambda_d = 8.7m$, respectively.

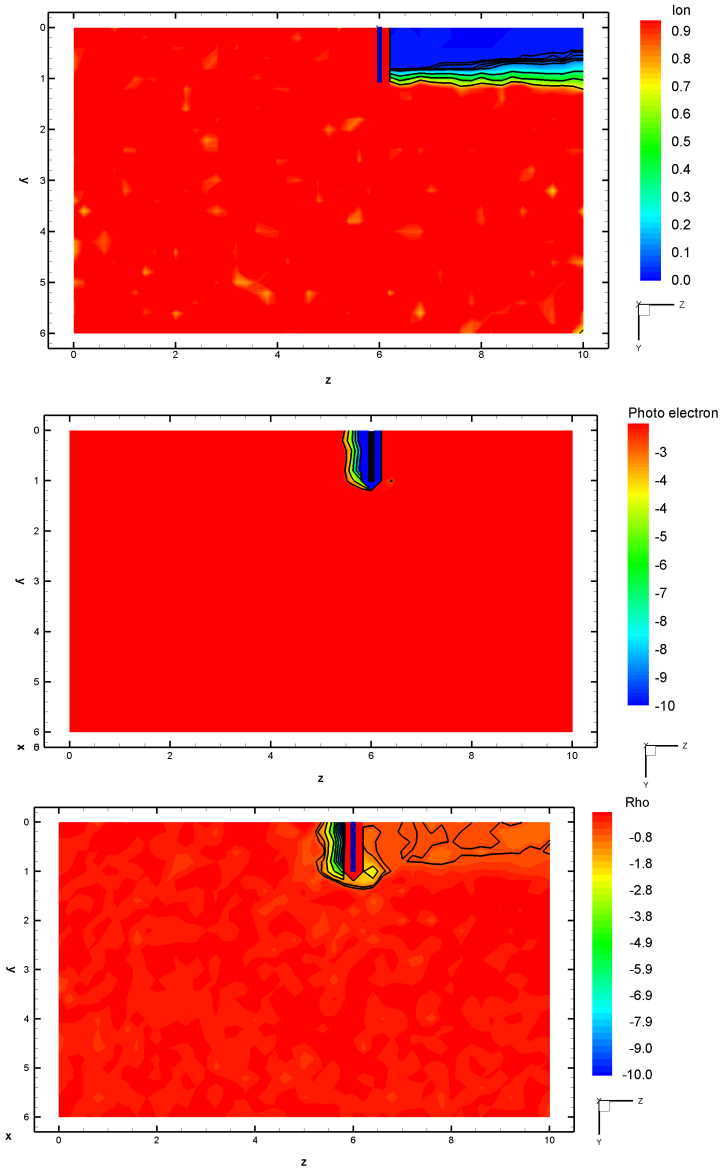

Figure 4.17: Ion density (top), photoelectron density (middle), and total charge density (bottom) contours on a $y-z$ plane. Density and distance are normalized by electron density n_e and electron Debye length $\lambda_d = 8.7m$, respectively.

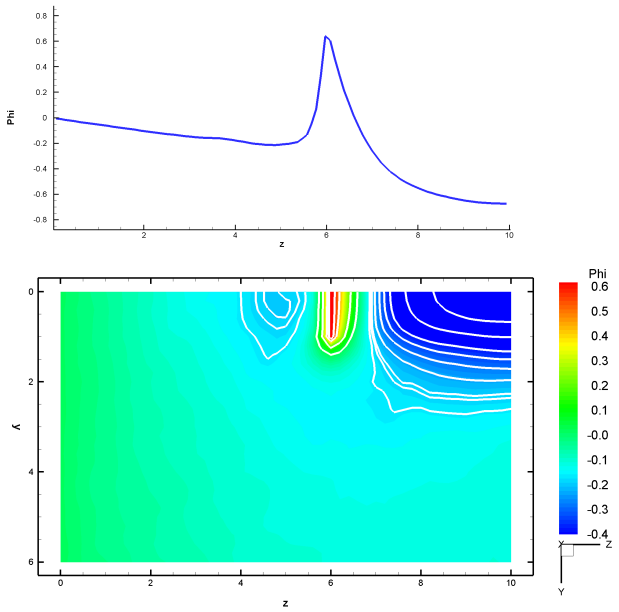

Figure 4.18: 1-D potential profile along the central axis of the solar sail (top) and potential contours on the x=0 plane (bottom). Potential and distance values are normalized by $T_e = 12eV$ and electron Debye length $\lambda_d = 8.7m$, respectively.

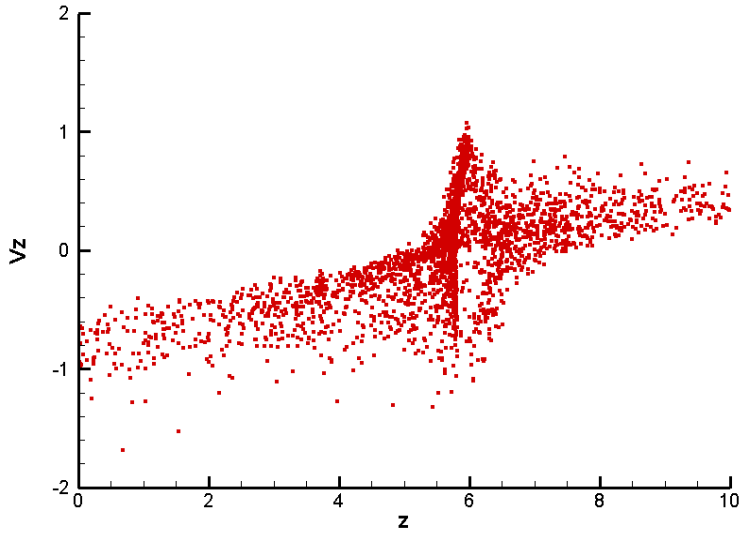

Figure 4.19: z-direction phase plot for photoelectrons. v_z and z are normalized by solar wind electron thermal velocity and electron Debye length $\lambda_d = 8.7m$, respectively.

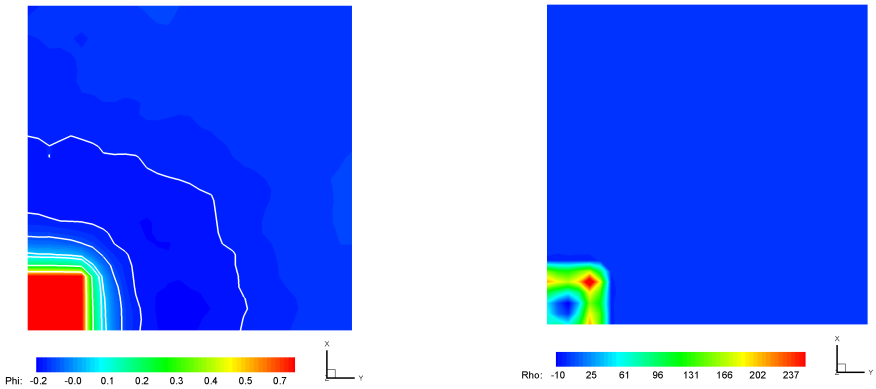

Figure 4.20: Potential contours (left) and charge density (right) on solar sail surface. Density, potential, and distance are normalized by n_e, $T_e = 12eV$, and $\lambda_d = 8.7m$, respectively.

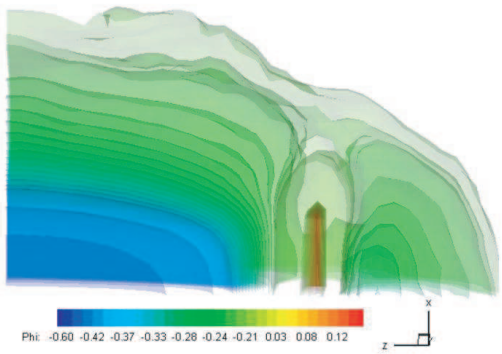

Figure 4.21: Potential iso-surfaces where potential and distance values are normalized by $T_e = 12eV$ and electron Debye length $\lambda_d = 8.7m$, respectively.

4.2 Solar Wind Interactions with a Spacecraft

This section considers a more complex configuration for spacecraft model shown in Fig 4.22. The spacecraft bus is modeled as a box and solar panels are modeled as two thin plates. We consider two types of electric connections. In case I, we consider that the main body is electrically isolated from the solar panels. In case II, we consider that the spacecraft connected electrically between a main body and solar panels. The spacecraft charging is examined under various solar wind conditions: solar wind mean flux, solar wind 5% flux, solar wind 95% flux, and severe magnetosheath charging conditions as listed in Table 1.2. In this simulation, photoelectron saturation current density and photoelectron energy are assumed as $J_{ph} = 5(\mu A m^{-2})$ and $T_{ph} = 2eV$, respectively. Table 4.4 shows the spacecraft dimension corresponding to solar wind conditions. Using symmetric geometry of a spacecraft, the simulation is carried out only on a quarter of the spacecraft as shown in Fig. 4.22. Table 4.4 shows the spacecraft dimensions used in the simulations. The cell resolution is taken to be $\Delta x = \Delta y = \Delta z = 0.1\lambda_d$ where λ_d is the solar wind plasma Debye length. Here, the photoelectron Debye length is $\lambda_{ph} = 0.92m$. The time interval is calculated from the cell size and the maximum velocity for particles at each time step. The number of macro-particles used is about 50 per cell for each species. The simulation is performed using the real ion to electron mass ratio $m_i/m_e = 1836$ in order to maintain the correct mesothermal velocity ratio. In order to roughly estimate charging, the solar wind current density on the upstream boundary is obtained using the one-sided drifting Maxwellian function of Eq. (2.7). Their magnitudes are shown in Table 4.5. The balance for solar wind and photoelectron current densities would allow a simple estimating of the spacecraft potential. For instance, it can be expected that the spacecraft have high negative potential under severe magnetosheath charging condition. Table 4.6 summarizes the floating potential obtained from the numerical simulation for case I and case II.

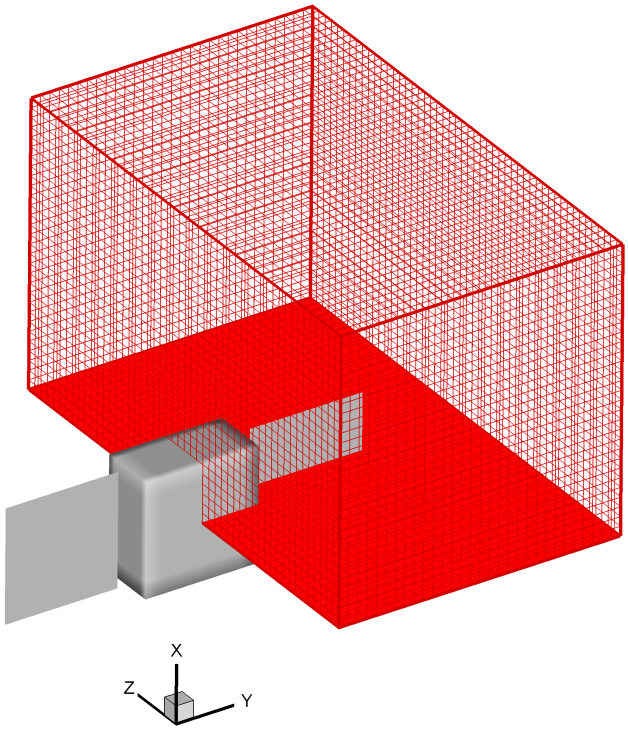

Figure 4.22: Simulation set-up associated with spacecraft geometry consisting of a body and solar panels.

SPACECRAFT CHARING IN DIELECTRIC MATERIAL

We first performed a 3-D full PIC simulation for the spacecraft consisting of dielectric materials under the mean solar wind condition. Fig. 4.23 shows the potential contours on a $y-z$ plane for a spacecraft consisting of typical dielectric materials. As shown in the figure, the sunlit surface of the main body is positively charged by the photoelectron emissions. The wake side of the body is negatively charged due to back-flowing electrons. Solar panel also shows a non-uniform potential distribution on the surface.

MEAN SOLAR WIND CONDITION

Fig. 4.24 shows the potential contours on a $y-z$ plane of a spacecraft electrically isolated

Table 4.4: Spacecraft dimensions used in charging simulations.

	Main body (m^3)	Solar panel (m^2)	ε_r
Solar wind mean flux density	$7 \times 7 \times 3.5$	7×7	1
Solar wind 5% flux density	$12 \times 12 \times 6$	12×12	1
Solar wind 95% flux density	$2 \times 2 \times 1$	2×2	1
Magnetosheath	$46 \times 46 \times 23.5$	46×46	1

Table 4.5: Comparison of solar wind and photoelectron current densities.

	$J_e(\mu Am^{-2})$	$J_i(\mu Am^{-2})$	$J_{ph}(\mu Am^{-2})$
Solar wind mean flux density	1.18	0.65	5
Solar wind 5% flux density	0.41	0.24	5
Solar wind 95% flux density	18.2	14.4	5
Magnetosheath	92.16	14.4	5

(case I) under the mean solar wind condition. The figure clearly shows the photoelectrons sheath profile in the front side of a spacecraft by photoelectron emissions and the wake structure in the back side of a spacecraft by drifting plasma. As shown in the figure, a solar panel is positively charged up to $3.6V$ under photoelectron emissions, $J_{ph} = 5\mu A/m^2$. On the other hand, a main body has relatively low positive floating potential, $\phi_s \sim 0.2V$, due to the ambient electrons impinging onto the side of the body. Fig. 4.25 provides iso-surfaces for

Table 4.6: Floating potential under various solar wind conditions for case I and case II.

Parameter	body	panel	body + panel
Solar wind mean flux density	$1.2V$	$3.6V$	$2.5V$
Solar wind 5% flux density	$4.8V$	$7.2V$	$6V$
Solar wind 95% flux density	$-6V$	$-1.5V$	$-3V$
Magnetosheath	–	–	$-1400V$

electric potential (Case I) under the mean solar wind condition. The potential and distance are normalized by $T_e = 12eV$ and electron Debye length $\lambda_d = 8.7m$, respectively. Figs. 4.26 - 4.28 show the results (case II) for spacecraft charging under the mean solar wind condition. Fig. 4.26 shows electron (top-left), ion (top-right), photoelectron (bottom-left), and total charge (bottom-right) density contours on $y-z$ and $x-z$ planes at steady state. The density and distance are normalized by electron density n_e and electron Debye length λ_d, respectively. Fig. 4.27 shows the potential contours on a $y-z$ plane. As shown in Figs. 4.27 - 4.28, the floating potential is equipotential, $\phi_s \sim 2.5V$, on the entire spacecraft by charge re-distribution. It is obvious that the spacecraft is charged positively based on current balance given in Table 4.5. Fig. 4.29 shows the spacecraft potential evolution through time where the dotted line, dashed line, and solid line indicate a main body (case I), a solar panel (case I), and a spacecraft (case II). Potential and time are normalized by $T_e = 12eV$ and $\omega_{pe}^{-1} = 6. \times 10^{-6}s$, respectively.

SOLAR WIND 5% FLUX CONDITION

Figs. 4.30 - 4.34 shows the results for spacecraft charging for both case I and case II under solar wind 5% flux condition. Fig. 4.30 shows the potential contours on a $y-z$ plane of a spacecraft electrically isolated (case I). Fig. 4.31 provides iso-surfaces for electric potential (case I) under solar wind 5% flux condition. The potential and distance are normalized by $T_e = 12eV$ and electron Debye length $\lambda_d = 14.5m$, respectively. Fig. 4.32 shows the potential contours on a $y-z$ plane for case II. Fig. 4.34 shows the spacecraft potential evolution through time where the dotted line, dashed line, and solid line indicate a main body (case I), a solar panel (case I), and a spacecraft (case II). The potential and time are normalized by $T_e = 12eV$ and $\omega_{pe}^{-1} = 1.0 \times 10^{-5}s$, respectively.

SOLAR WIND 95% FLUX CONDITION

Figs. 4.35 - 4.39 shows the results for spacecraft charging for both case I and case II under

95% solar wind flux condition. As shown in Table 4.5, the ambient electron current density exceeds the ion current and photoelectron current and expected to result in the negative floating potential. Fig. 4.35 shows the potential contours on a $y-z$ plane (case I). Fig. 4.36 provide iso-surfaces for electric potential (case I). The potential and distance are normalized by $T_e = 12eV$ and electron Debye length $\lambda_d = 2.6m$, respectively. Fig. 4.37 shows the potential contours on a $y-z$ plane (case II). As shown in Figures 4.37 - 4.38, the floating potential is equipotential on the entire spacecraft (case II). Fig. 4.39 shows the spacecraft potential evolution over time where the dotted line, dashed line, and solid line indicate a main body (case I), a solar panel (case I), and a spacecraft (case II). The potential and time are normalized by $T_e = 12eV$ and $\omega_{pe}^{-1} = 1.8 \times 10^{-6}s$, respectively.

SEVERE MAGNETOSHEATH CHARGING CONDITION

Charging analysis is carried out in magnetosheath for case II. Table 4.5 shows that the electrons current density extremely exceeds the ion current and photoelectron current. As expected in the current comparison, spacecraft is negatively charged up to $-1400V$. Fig. 4.40 shows the potential contours on a $y-z$ plane. As shown in Figs. 4.40 - 4.41, the floating potential is equipotential on the entire spacecraft. Fig. 4.42 shows the spacecraft potential evolution through time (case II).

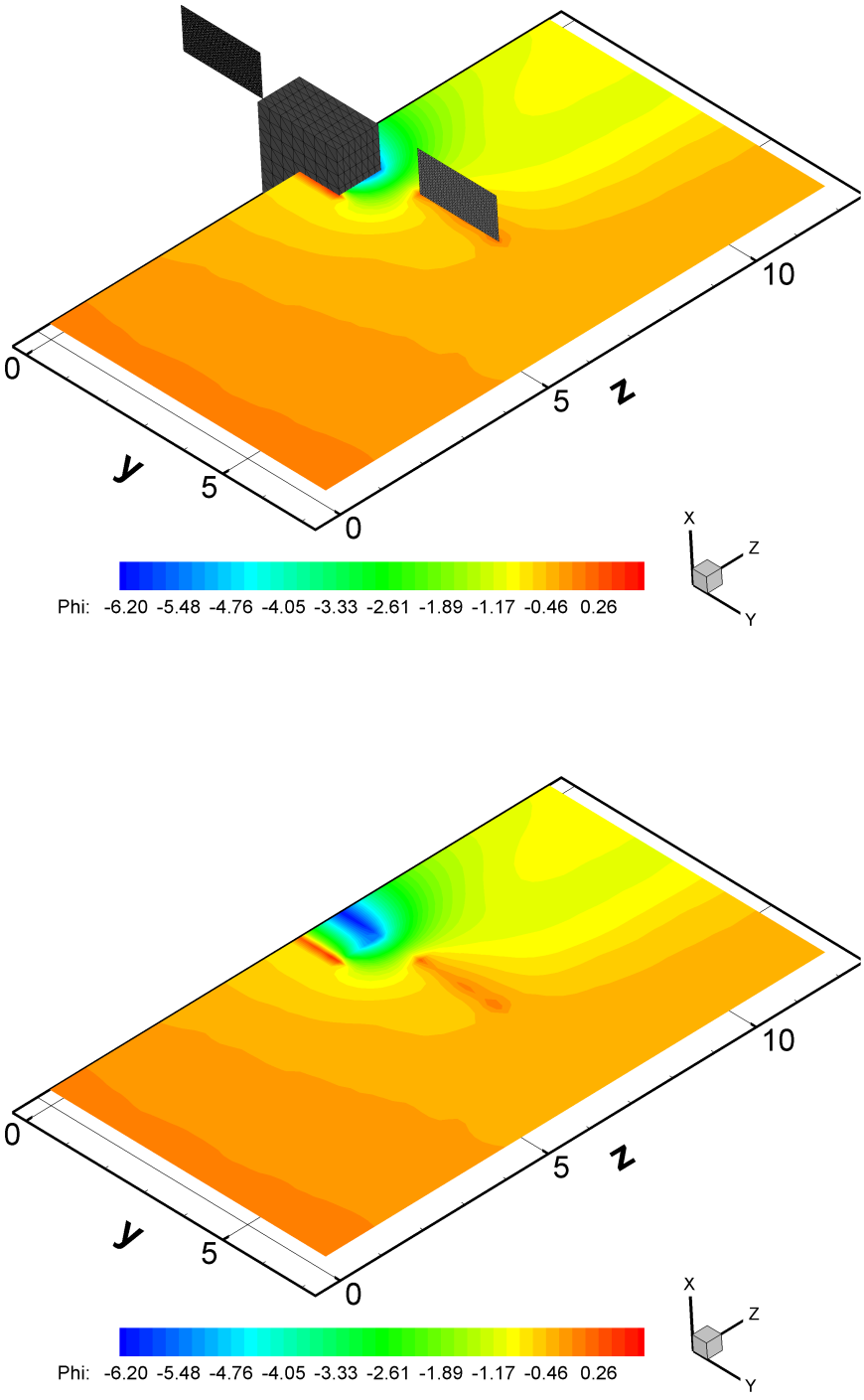

Figure 4.23: Potential contours on a $y-z$ plane for a spacecraft consisting of a dielectric material. The potential and distance are normalized by $T_e = 15eV$ and electron Debye length $\lambda_d = 15.4m$, respectively.

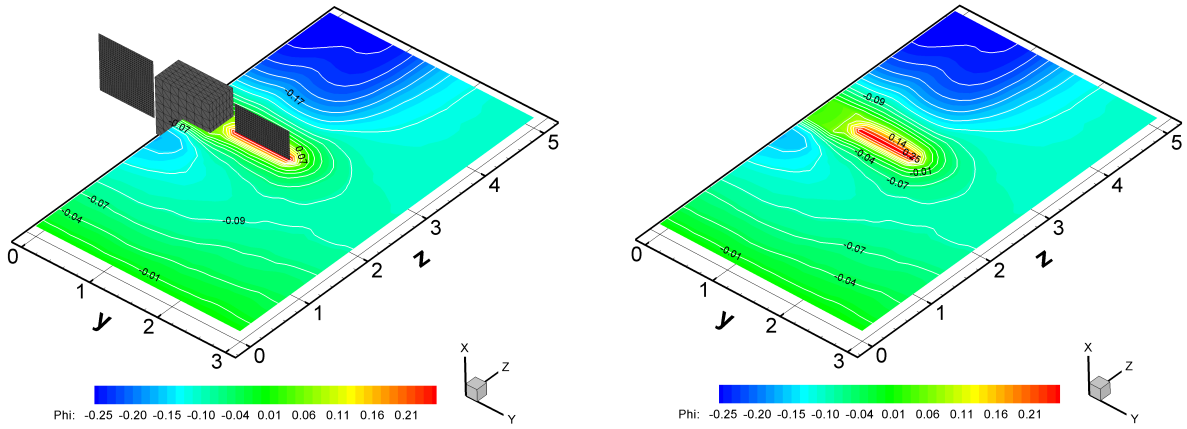

Figure 4.24: Potential contours on a $y-z$ plane under the mean solar wind condition (case I) where the main body and solar panel are electrically isolated. The potential and distance are normalized by $T_e = 12eV$ and electron Debye length $\lambda_d = 8.7m$, respectively.

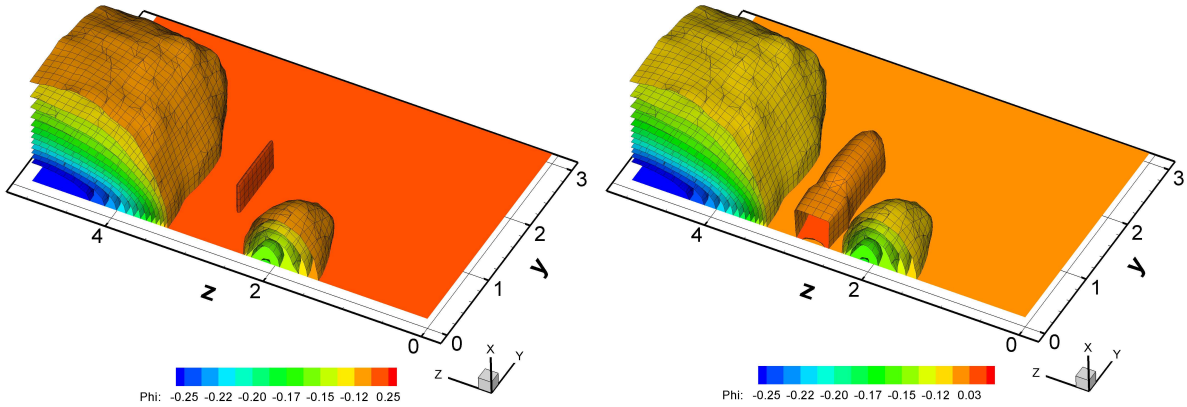

Figure 4.25: Iso-surfaces for electric potential (case I) under the mean solar wind condition. The potential and distance are normalized by $T_e = 12eV$ and electron Debye length $\lambda_d = 8.7m$, respectively.

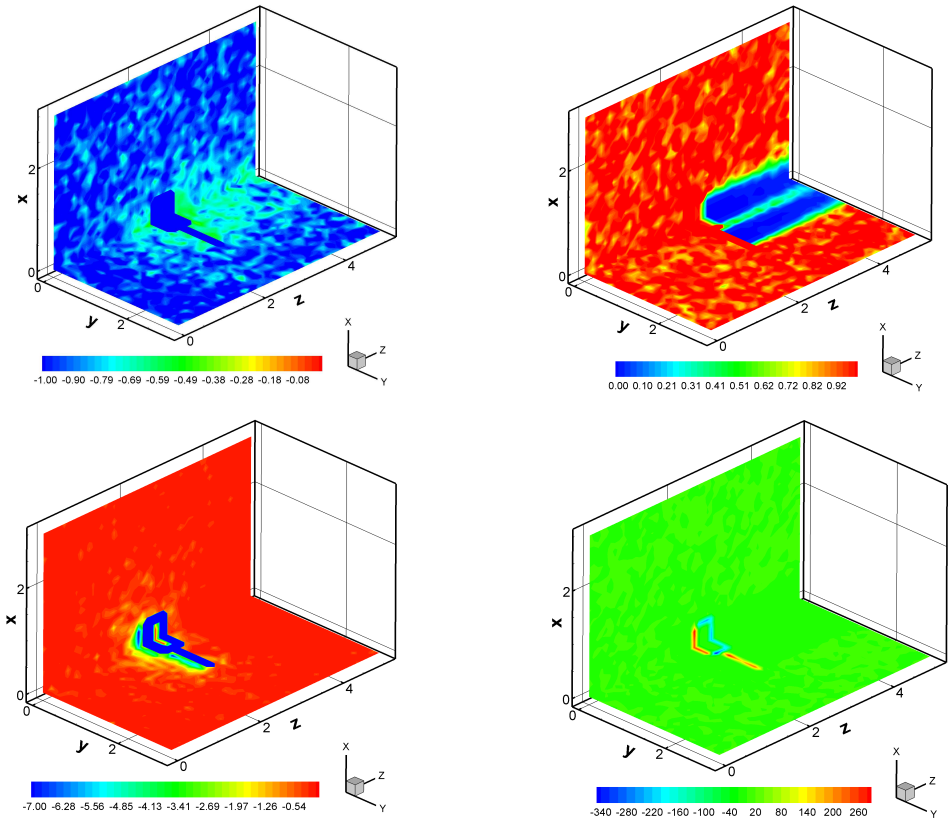

Figure 4.26: Electron (top-left), ion (top-right), photoelectron (bottom-left), and total charge (bottom-right) density contours on $y-z$ and $x-z$ planes at steady state under the mean solar wind condition (case II). The density and distance are normalized by electron density n_e and electron Debye length $\lambda_d = 8.7m$, respectively.

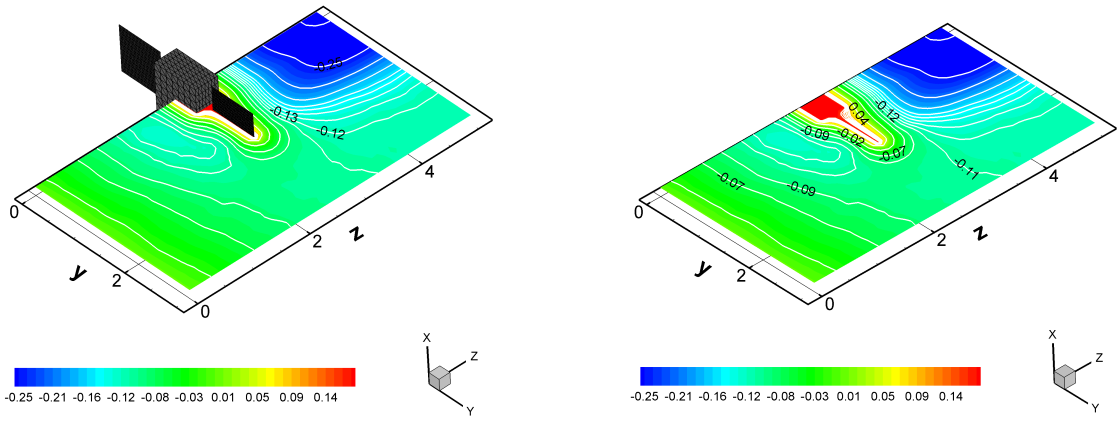

Figure 4.27: Potential contours on a $y-z$ plane where the main body and solar panel are electrically connected under the mean solar wind condition (case II). The potential and distance are normalized by $T_e = 12eV$ and electron Debye length $\lambda_d = 8.7m$, respectively.

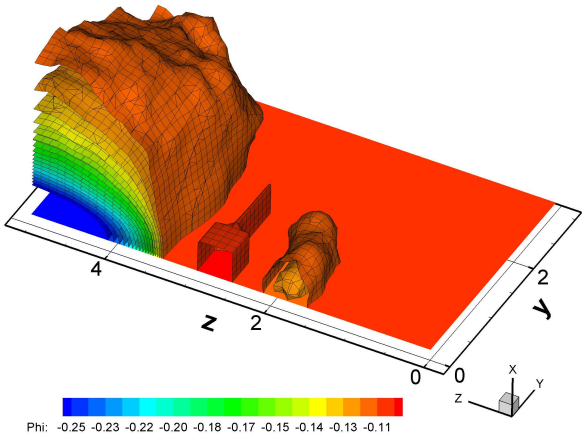

Figure 4.28: Iso-surfaces for electric potential (case II) under the mean solar wind condition. The potential and distance are normalized by $T_e = 12eV$ and electron Debye length $\lambda_d = 8.7m$, respectively.

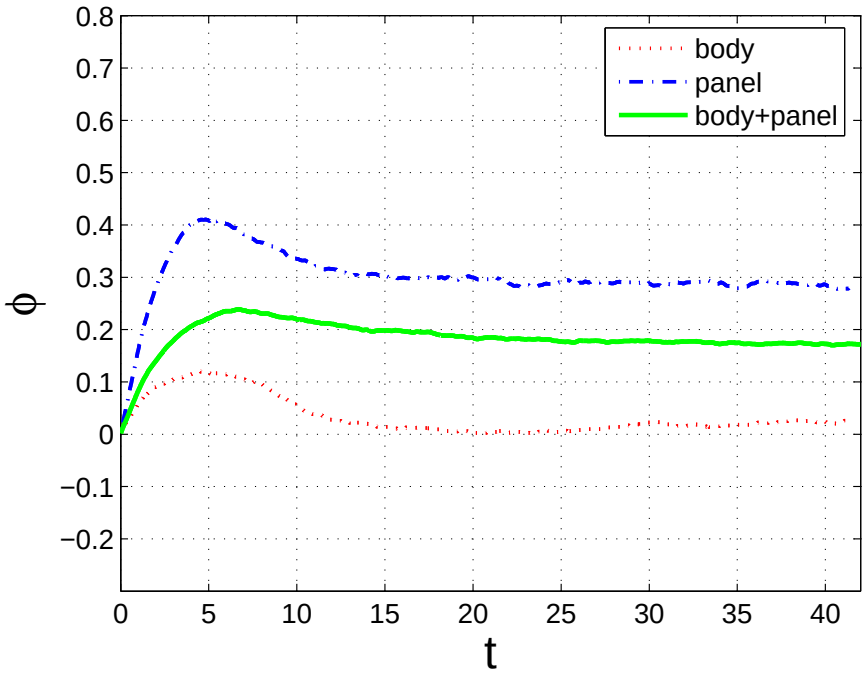

Figure 4.29: Spacecraft potential evolution over time where the dotted line, dashed line, and solid line indicate a main body (case I), a solar panel (case I), and a spacecraft (case II) under the mean solar wind condition. The potential and time are normalized by $T_e = 12eV$ and $\omega_{pe}^{-1} = 6. \times 10^{-6}s$, respectively.

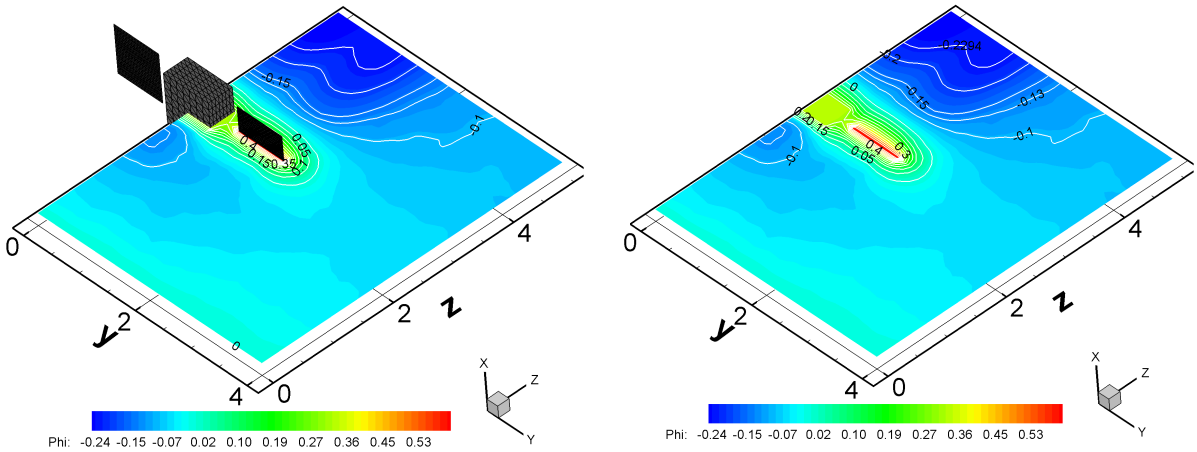

Figure 4.30: Potential contours on a $y-z$ plane under solar wind 5% flux condition (case I) where the main body and solar panel are electrically isolated.

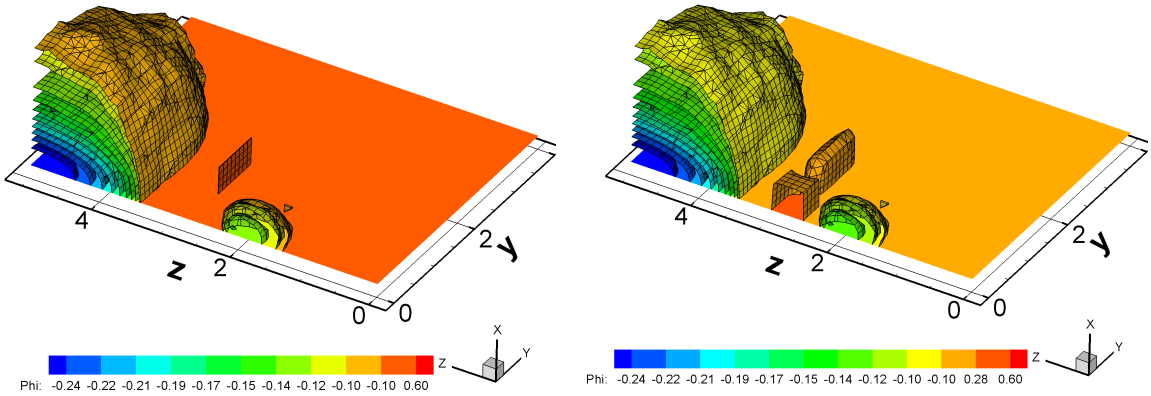

Figure 4.31: Iso-surfaces for electric potential (case I) under solar wind 5% flux condition. The potential and distance are normalized by $T_e = 12eV$ and electron Debye length $\lambda_d = 14.5m$, respectively.

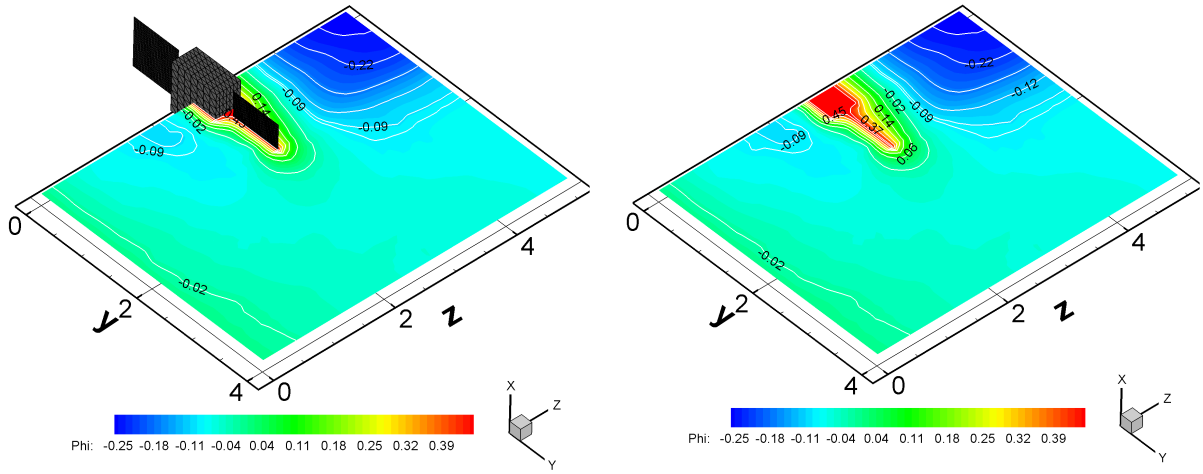

Figure 4.32: Potential contours on a $y-z$ plane where the a main body and a solar panel are electrically connected under solar wind 5% flux condition (case II). The potential and distance are normalized by $T_e = 12eV$ and electron Debye length $\lambda_d = 14.5m$, respectively.

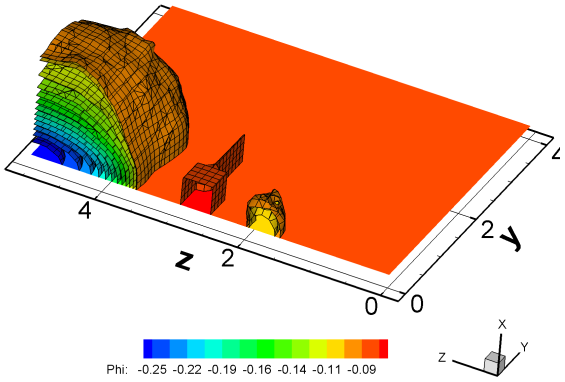

Figure 4.33: Iso-surfaces for electric potential (case II) under solar wind 5% flux condition. The potential and distance are normalized by $T_e = 12eV$ and electron Debye length $\lambda_d = 14.5m$, respectively.

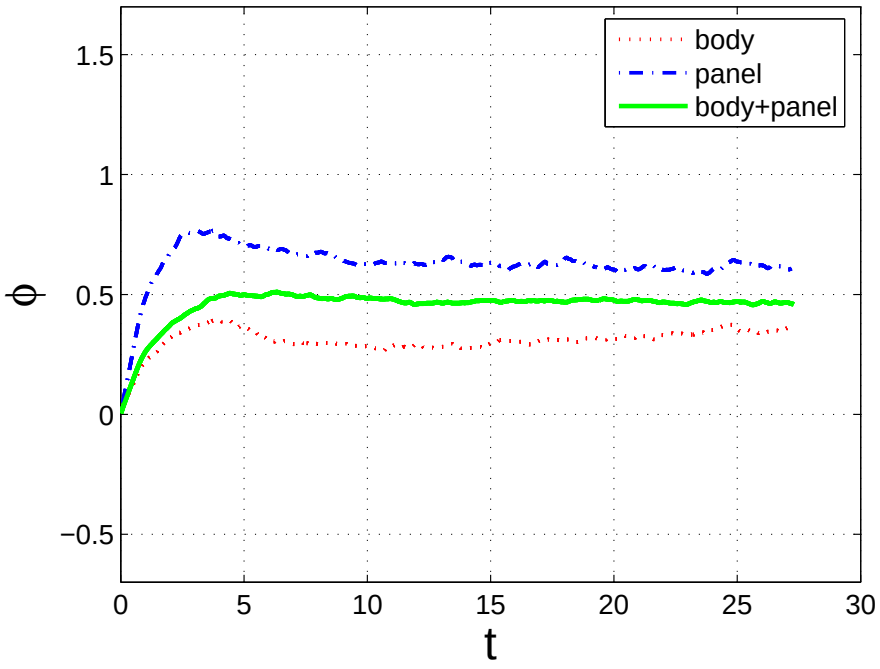

Figure 4.34: Spacecraft potential evolution over time where the dotted line, dashed line, and solid line indicate a main body (case I), a solar panel (case I), and a spacecraft (case II) under solar wind 5% flux condition. The potential and time are normalized by $T_e = 12eV$ and $\omega_{pe}^{-1} = 1.0 \times 10^{-5}s$, respectively.

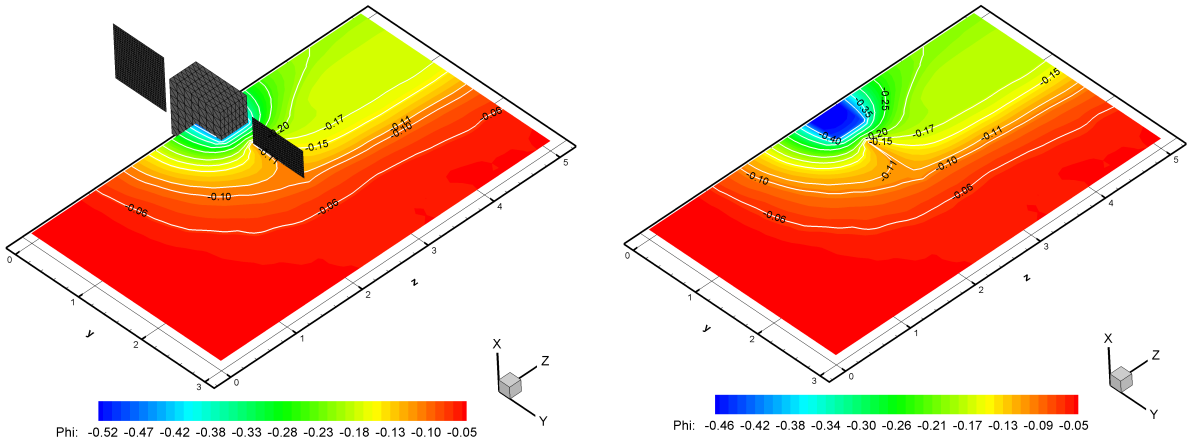

Figure 4.35: Potential contours on a $y-z$ plane under solar wind 95% flux condition (case I) where the a main body and a solar panel are electrically isolated. The potential and distance are normalized by $T_e = 12eV$ and electron Debye length $\lambda_d = 2.6m$, respectively.

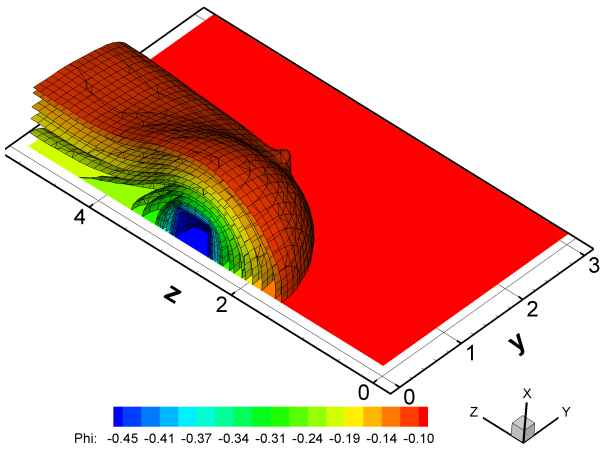

Figure 4.36: Iso-surfaces for electric potential (case I) under solar wind 95% flux condition. The potential and distance are normalized by $T_e = 12eV$ and electron Debye length $\lambda_d = 2.6m$, respectively.

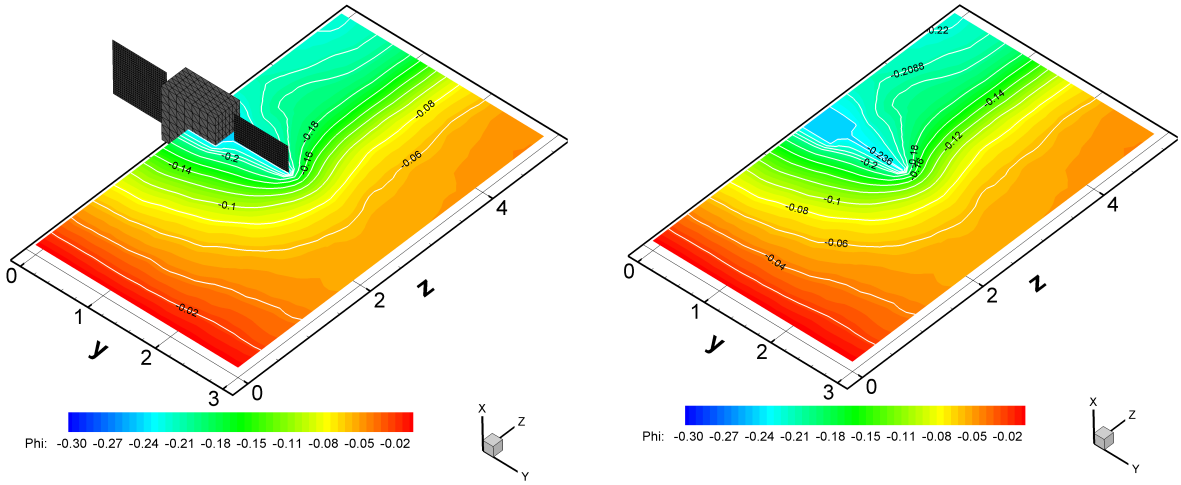

Figure 4.37: Potential contours on a $y-z$ plane where the main body and solar panel are electrically connected under solar wind 95% flux condition (case II). The potential and distance are normalized by $T_e = 12eV$ and electron Debye length $\lambda_d = 2.6m$, respectively.

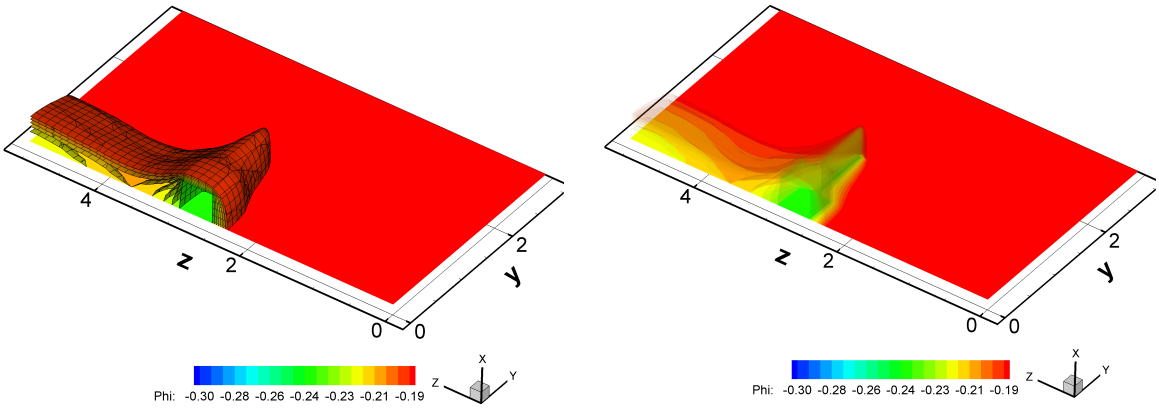

Figure 4.38: Iso-surfaces for electric potential (case II) under solar wind 95% flux condition. The potential and distance are normalized by $T_e = 12eV$ and electron Debye length $\lambda_d = 2.6m$, respectively.

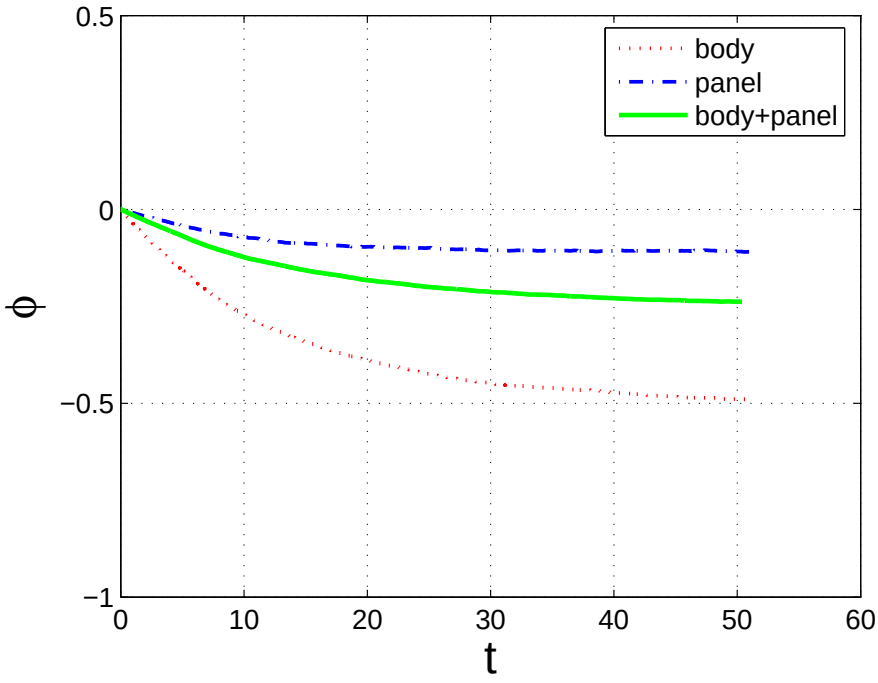

Figure 4.39: Spacecraft potential evolution over time where the dotted line, dashed line, and solid line indicate a main body (case I), a solar panel (case I), and a spacecraft (case II) under solar wind 95% flux condition. The potential and time are normalized by $T_e = 12eV$ and $\omega_{pe}^{-1} = 1.8 \times 10^{-6}s$, respectively.

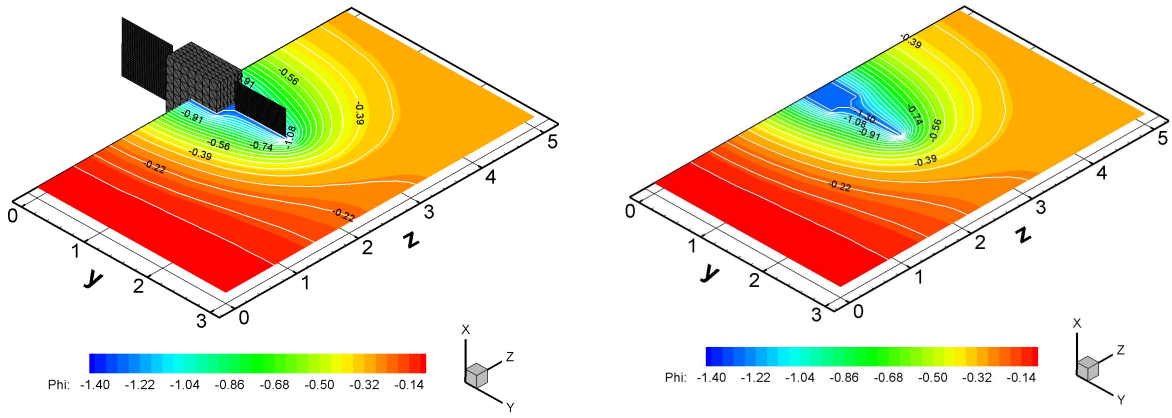

Figure 4.40: Potential contours on a $y-z$ plane where the a main body and a solar panel are electrically connected under severe magnetosheath charging condition (case II). The potential and distance are normalized by $T_e = 1000eV$ and electron Debye length $\lambda_d = 23.5m$, respectively.

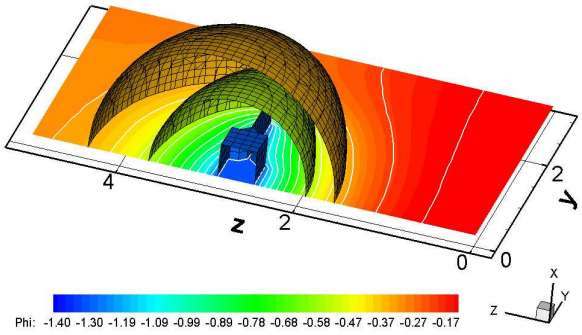

Figure 4.41: Iso-surfaces for electric potential (case II) under severe magnetosheath charging condition. The potential and distance are normalized by $T_e = 1000eV$ and electron Debye length $\lambda_d = 23.5m$, respectively.

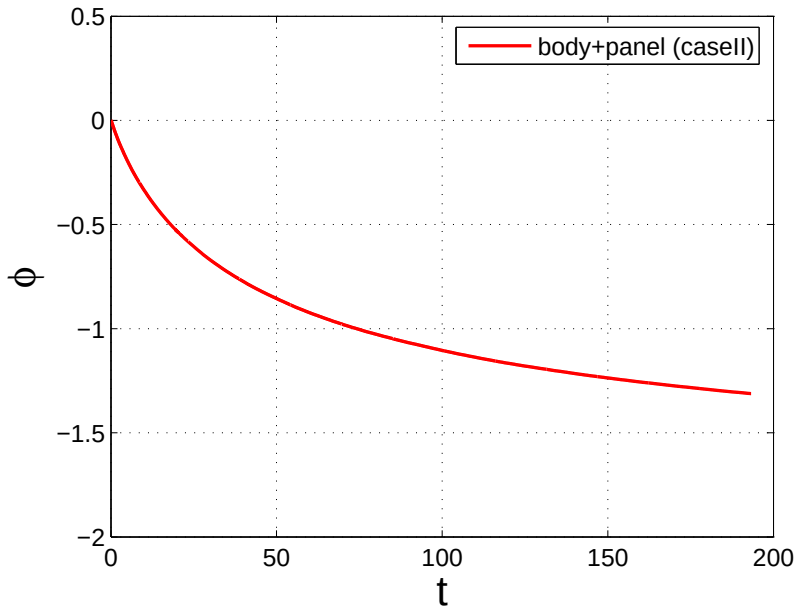

Figure 4.42: Spacecraft potential evolution through time under severe magnetosheath charging condition. The potential and time are normalized by $T_e = 1000eV$ and $\omega_{pe}^{-1} = 1.8\times10^{-6}s$, respectively.

4.3 Solar Wind Interactions with a Multibody System

In this section, we investigated the interactions of a "multibody system" and the solar wind in the absence of photoelectron emissions (eclipse). The multibody system considered here consists of a large platform and a rectangular body. The primary objective of the multibody-plasma interactions is to explore the interactions of the charged bodies as well as the wake charging effect. Several studies associated with the wake charging effects have been discussed [39, 40, 45, 87, 16, 93]. The wake charging is caused by a lack of ions in the wake behind a large structure in a flowing plasma. In previous studies, Boltzmann PIC simulations are performed to investigate the wake charging effect [93]. Here, we extend the previous studies by using a full particle simulation model.

Simulations are performed for solar wind mean flux, solar wind 95% flux, and severe magnetosheath conditions as shown in Table 1.2. Ion and electron currents collected by the free flyer are different along the distance from the platform, depending on ambient plasma temperature and the size of the front platform. In simulation conditions used here, severe wake charging may occur in the wake zone close to a front plate due to reduced ion current. In this dissertation, we set a free flyer at $2\lambda_d$ behind the large platform on the central axis in the wake. We used the the same non-dimensional input for the plate and free flyer for all three different plasma conditions considered. The plate dimension is taken to be $6\lambda_d \times 6\lambda_d$ and the free flyer dimension is $1.2\lambda_d \times 1.2\lambda_d \times 0.6\lambda_d$. Since the plasma Debye length varied under different ambient plasma conditions, the systems studied for different plasma conditions are of different sizes. The physical dimensions of the systems considered are listed in Table 4.7. Table 4.8 shows the floating potential obtained from the numerical simulations.

MEAN SOLAR WIND CONDITION

Fig. 4.44 shows electron density contours (top-left), electron velocity vectors (top-right), ion density contours (bottom-left), and ion velocity vectors (bottom-right) on a $y-z$ plane under the mean solar wind condition. Ion thermal velocity ($v_{ti} \sim 43.8 km/s$) is relatively

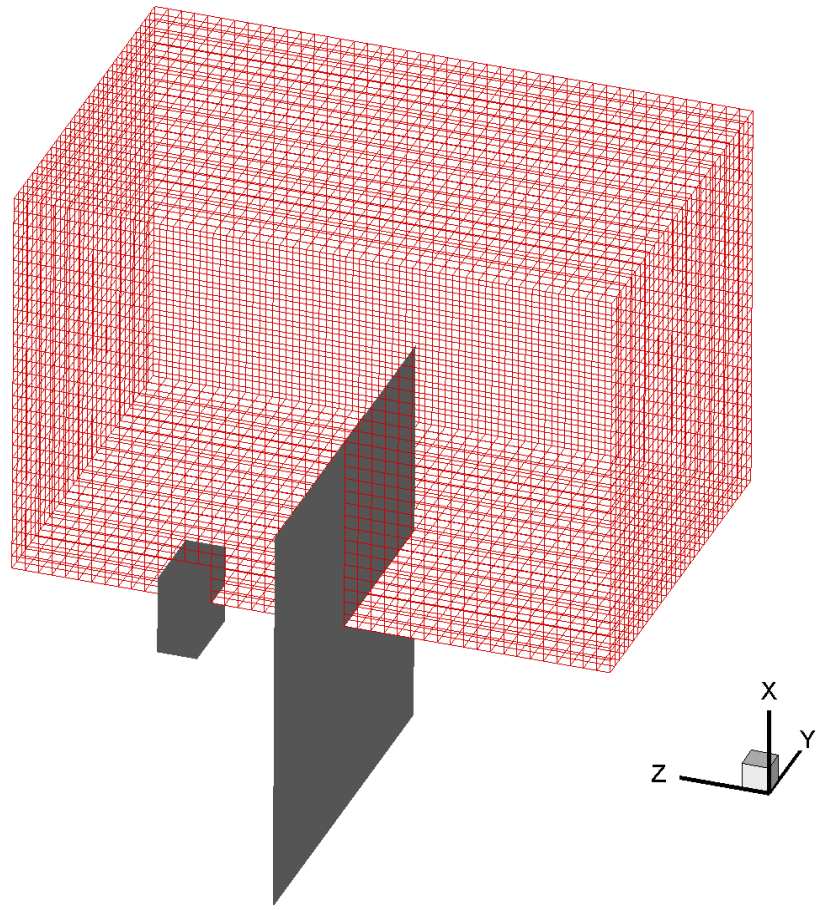

Figure 4.43: Simulation set-up associated with multibody system consisting of a large platform and a free flyer.

lower than the drifting velocity ($v_d \sim 468km/s$), resulting in the wake structure. Due to a lack of ions in the wake region, a free flyer will be charged more negatively in order to collect the ion current required to balance the electron current. The floating potential ratio between a platform and a free flyer is about $\frac{\phi_f}{\phi_p} \sim 2.14$ where ϕ_p and ϕ_f are the floating potential for a platform and a free flyer, respectively. Figs. 4.45 - 4.46 show the potential contours and iso-surfaces where the potential and distance are normalized by $T_e = 12eV$ and electron Debye length $\lambda_d = 8.7m$, respectively. Here, we consider the following system: a plate size of $6\lambda_d \times 6\lambda_d$ and a free flyer size of $1.2\lambda_d \times 1.2\lambda_d \times 0.6\lambda_d$ sitting at $2\lambda_d$ behind the platform in the wake. For this particular system, a free flyer is charged negatively about

Table 4.7: Multibody system dimensions used in charging simulations.

	Platform (m^2)	Free flyer (m^3)	ε_r
Solar wind mean flux density	52×52	$10 \times 10 \times 5$	1
Solar wind 95% flux density	16×16	$3 \times 3 \times 1.5$	1
Magnetosheath	140×140	$28 \times 28 \times 14$	1

Table 4.8: Floating potential under various simulation conditions.

Parameter	Platform (ϕ, V)	Free flyer (ϕ, V)
Solar wind mean flux density	-8.4	-18
Solar wind 95% flux density	-4.8	-17.4
Magnetosheath	~ -1810	~ -1950

$-18V(\sim -1.5T_e)$ by a wake effect. Fig. 4.47 shows the potential evolution of a platform and a free flyer over time where the potential and time are normalized by $T_e = 12eV$ and $\omega_{pe}^{-1} = 6 \times 10^{-6}s$, respectively. Fig. 4.48 shows ion and electron currents for a platform and a free flyer over time where the current and time are normalized by J_e and $\omega_{pe}^{-1} = 6 \times 10^{-6}s$, respectively. In the simulation presented here, we initially loaded particles in the simulation domain and injected particles at each time step till each object reach to steady state condition. The current collection represents transient characteristics of our simulation system, showing the current balance process to obtain the floating potential. Note that a free flyer charged by wake charging converges on a floating potential much slower than the front platform does. As shown in the table, a free flyer are charged negatively by a wake effect of about $-18V$ under the mean solar wind condition and $-17.4V$ under solar wind 95% flux condition, respectively. As can be estimated by the ambient plasma properties, a free flyer under solar wind 95% flux condition due to enhanced ion current is less charged than the free flyer under the mean solar wind condition.

SEVERE MAGNETOSHEATH CHARGING CONDITION

Fig. 4.49 shows electron density contours (top-left), electron velocity vectors (top-right), ion density contours (bottom-left), and ion velocity vectors (bottom-right) on a $y-z$ plane under severe magnetosheath charging condition. Ion thermal velocity ($v_{ti} \sim 438km/s$) is relatively high when compared with the plasma drifting velocity ($v_d \sim 900km/s$). As can be seen in the figures, significant ion back-flow occurs due to comparatively high energy ions as well as the high voltage of the front plate. The floating potential ratio ,$\frac{\phi_f}{\phi_p}$, is about 1.1 which indicates that wake charging is relatively low. Also, the vector contours show that electrons are expelled by the highly charged objects at the steady state condition. Fig. 4.52 shows the potential evolution of a platform and a free flyer over time where the potential and time are normalized by $T_e = 1000eV$ and $\omega_{pe}^{-1} = 1.8 \times 10^{-6}s$, respectively. For a multibody system consisting of a $6\lambda_d \times 6\lambda_d$ plate and a $1.2\lambda_d \times 1.2\lambda_d \times 0.6\lambda_d$ free flyer, the floating potential for a free flyer is as high as $\sim -1950V (\sim -1.95T_e)$. The simulation results show that wake charging is not severe under both the mean solar wind condition and severe magnetosheath charging condition.

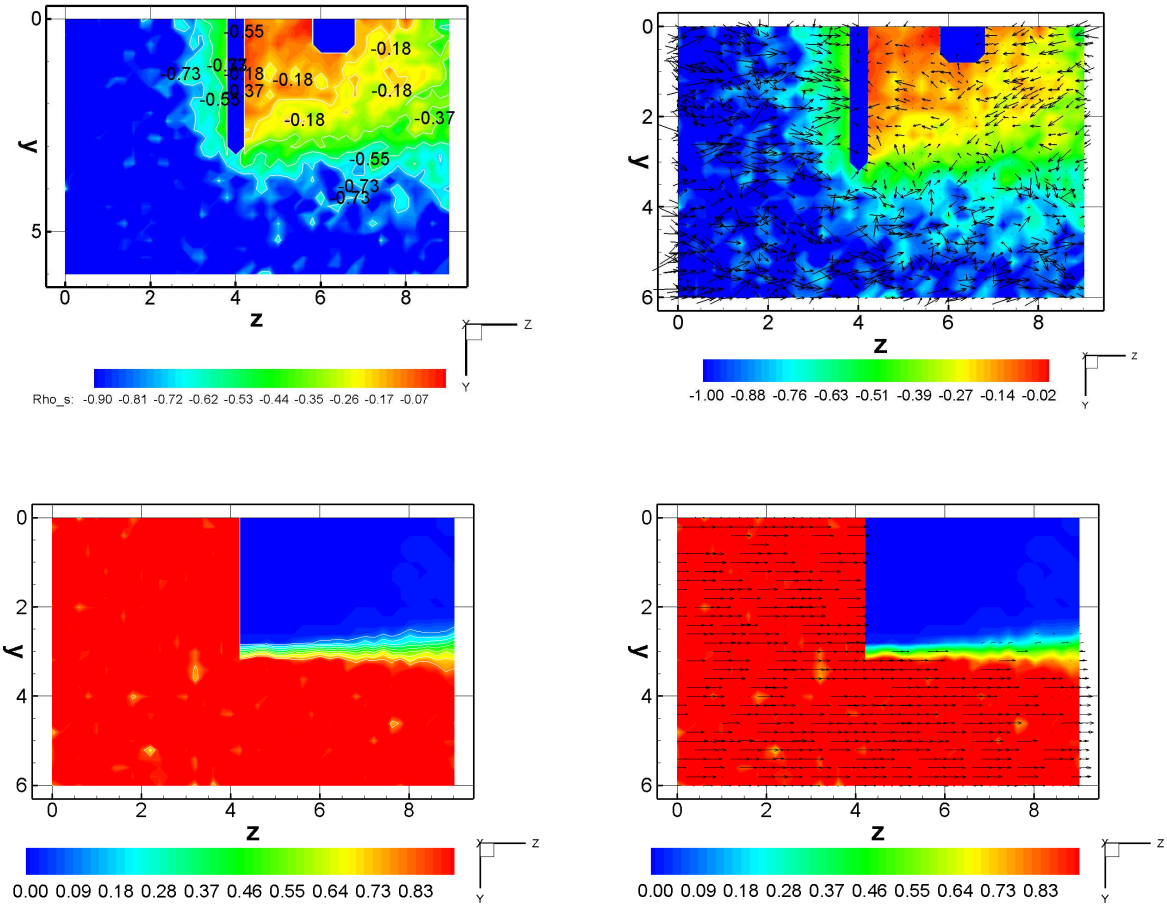

Figure 4.44: Electron density contours (top-left), electron velocity vectors (top-right), ion density contours (bottom-left), and ion velocity vectors (bottom-right) on a $y-z$ plane under the mean solar wind condition. The potential and distance are normalized by $T_e = 12eV$ and electron Debye length $\lambda_d = 8.7m$, respectively.

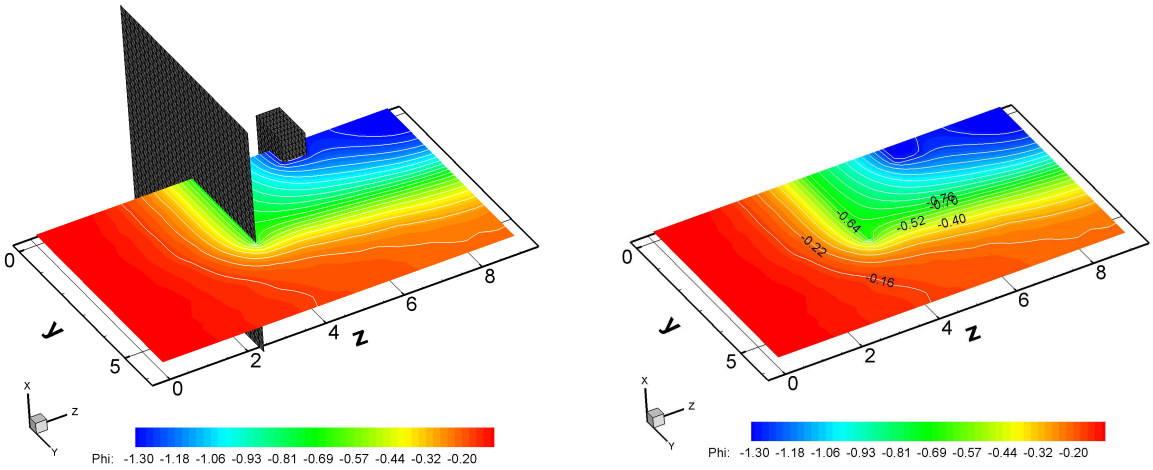

Figure 4.45: Potential contours on a $y-z$ plane under the mean solar wind flux condition. The potential and distance are normalized by $T_e = 12eV$ and electron Debye length $\lambda_d = 8.7m$, respectively.

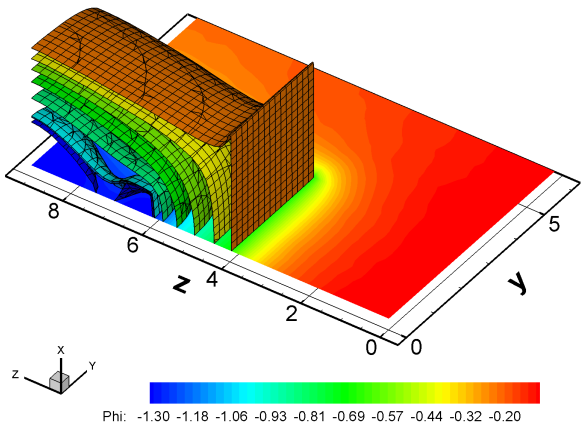

Figure 4.46: Iso-surfaces for electric potential under the mean solar wind flux condition. The potential and distance are normalized by $T_e = 12eV$ and electron Debye length $\lambda_d = 8.7m$, respectively.

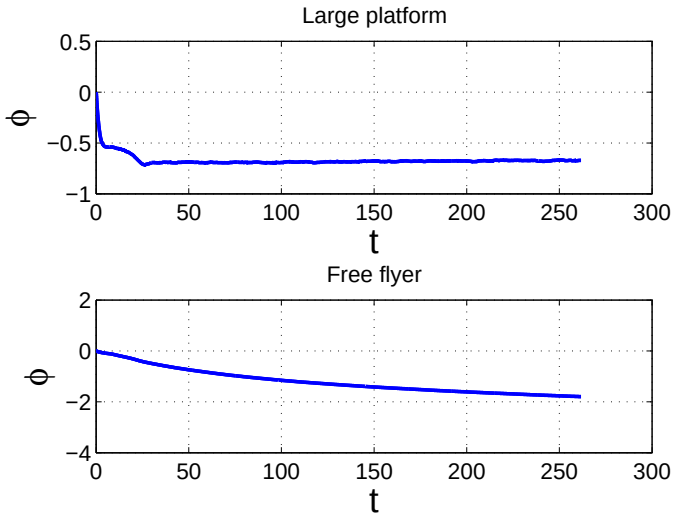

Figure 4.47: Potential evolution of a platform and a free flyer over time under the mean solar wind condition. The potential and time are normalized by $T_e = 12eV$ and $\omega_{pe}^{-1} = 6 \times 10^{-6}s$, respectively.

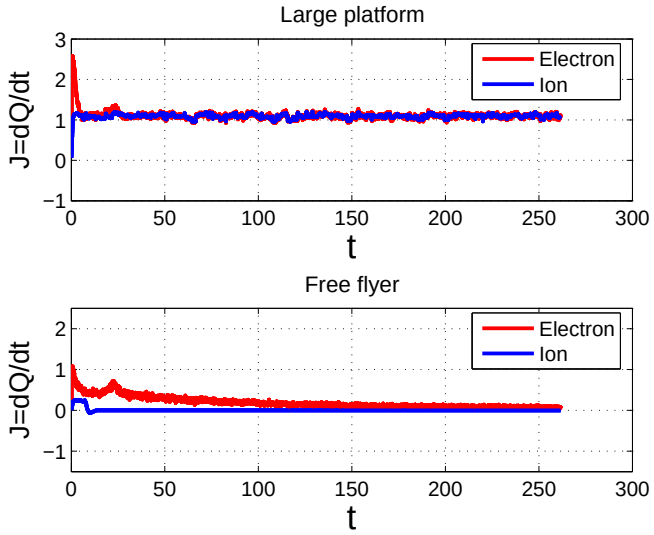

Figure 4.48: Ion and electron currents for a platform and a free flyer over time under the mean solar wind condition. The current and time are normalized by J_e and $\omega_{pe}^{-1} = 6 \times 10^{-6}s$, respectively.

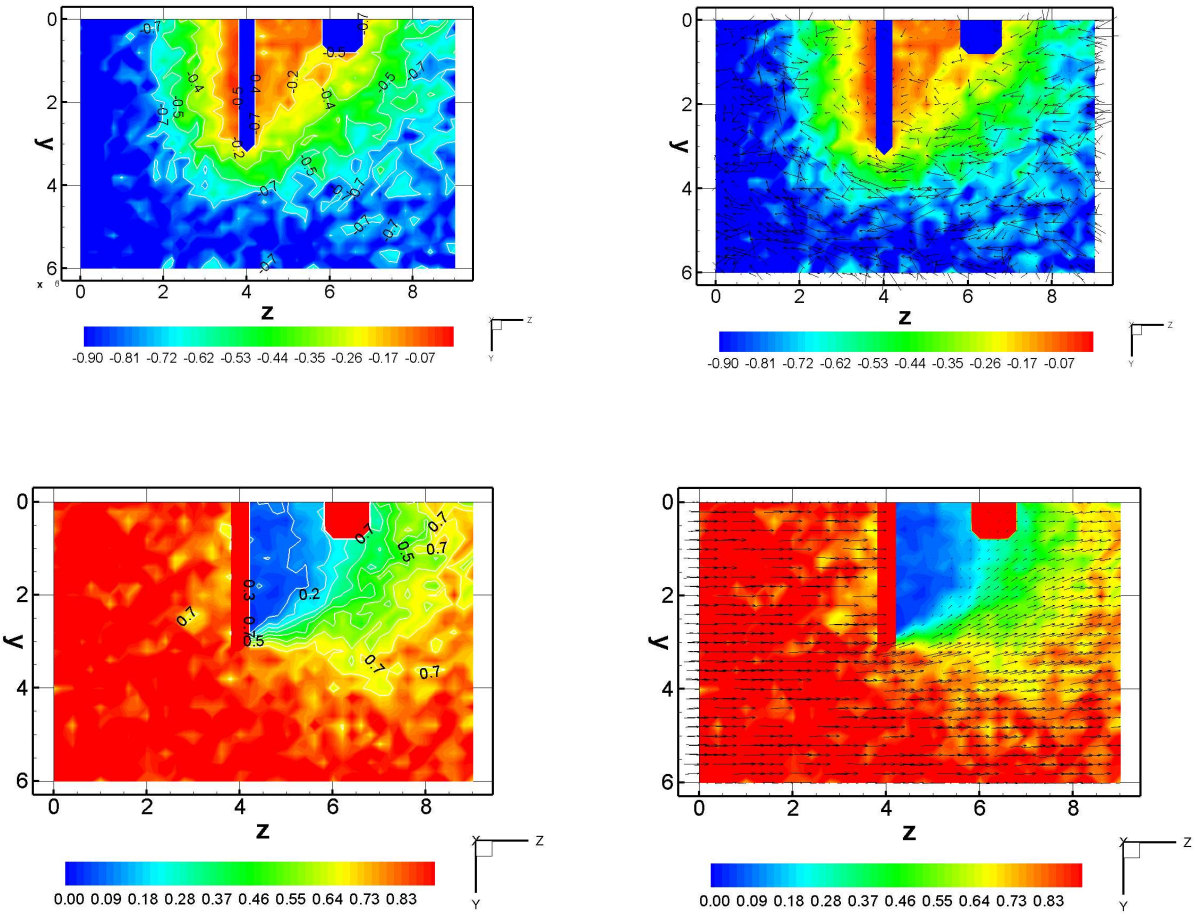

Figure 4.49: Electron density contours (top-left), electron velocity vectors (top-right), ion density contours (bottom-left), and ion velocity vectors (bottom-right) on a $y-z$ plane under severe magnetosheath charging condition. The potential and distance are normalized by $T_e = 1000eV$ and electron Debye length $\lambda_d = 23.5m$, respectively.

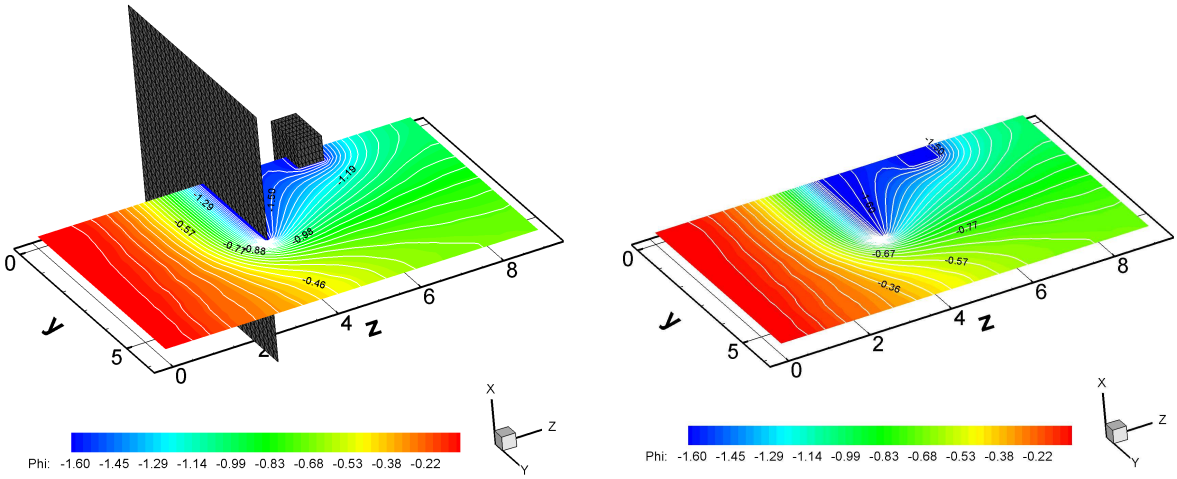

Figure 4.50: Potential contours on a $y-z$ plane under severe magnetosheath charging condition. The potential and distance are normalized by $T_e = 1000eV$ and electron Debye length $\lambda_d = 23.5m$, respectively.

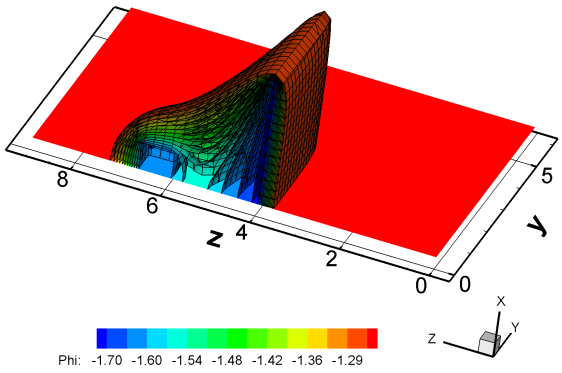

Figure 4.51: Iso-surfaces for electric potential under severe magnetosheath charging condition. The potential and distance are normalized by $T_e = 1000eV$ and electron Debye length $\lambda_d = 23.5m$, respectively.

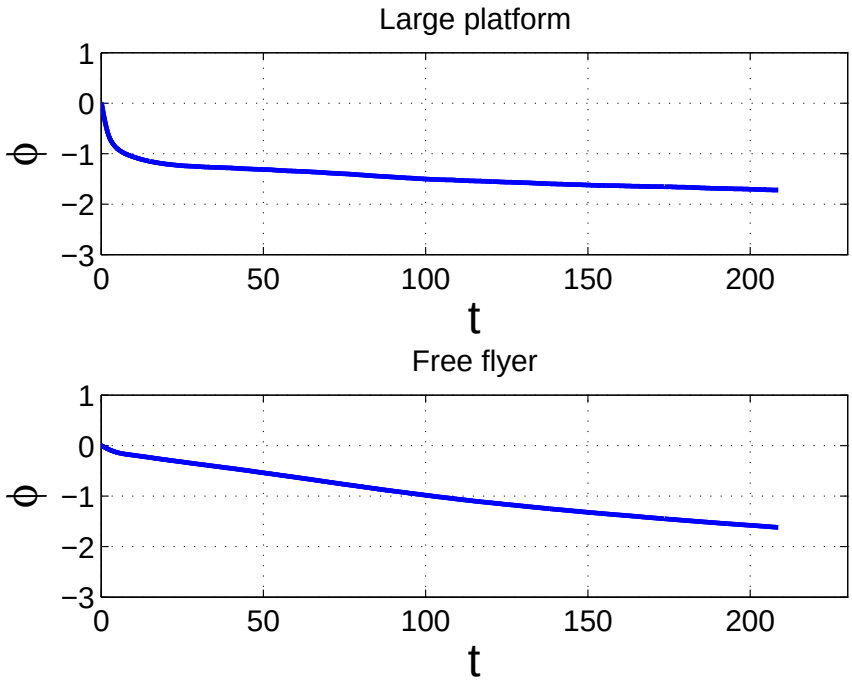

Figure 4.52: Potential evolution of a platform and a free flyer over time under severe magnetosheath charging condition. The potential and time are normalized by $T_e = 1000eV$ and $\omega_{pe}^{-1} = 1.8 \times 10^{-6}s$, respectively.

Chapter 5

Summary and Conclusions

5.1 Summary

In this dissertation, we investigated spacecraft charging and solar wind interactions by using both analytical and numerical approach.

Analytical Approach

In the analytical approach, we extended the previous photoelectron sheath theory [28, 18, 69] to include the effects of drifting electrons effects. We showed the modification of the potential profile and surface floating potential by the induced electron currents when drifting electrons are considered. There can exist three types of photoelectron sheaths in the presence of photoelectron emissions which can be classified as monotonic (Type B or Type C) or non-monotonic potential profile (Type A). Previously, Fu suggested that there can exist two solutions of monotonic and non-monotonic sheath profiles when photoelectron emissions are significant. A non-monotonic profile is the more stable solution in some parameters. We found that the surface floating potential obtained from the current balance calculation is very similar to that of the monotonic sheath solution. The potential barrier of a non-monotonic sheath will modify not only the photoelectron current but also the incident ambient current.

This is not surprising because current balance calculation does not include the modification of current sources by the potential barrier. This can lead to very different predictions on spacecraft floating potential. However, we can not determine mathematically which of two solutions is the physical one. In this dissertation, this question has been resolved using numerical simulation.

Numerical Approach

We studied a spacecraft charging and solar wind plasma interactions by using a 3-D full Particle PIC method [4]. Additionally, a charging model based on the capacitance matrix method is integrated into a PIC model so the floating potential on a spacecraft is calculated self-consistently using charges deposited on the surface. The PIC model is first applied to study the photoelectron sheath in a flowing plasma. We found that the numerical results from a charging model agree well with those of the non-monotonic sheath profile from the analytical method under solar wind conditions. PIC simulation results show that the potential barrier in a non-monotonic sheath can modify electron behavior and capture low energy electrons. The PIC model is then applied to investigate spacecraft charging under several solar wind conditions. The simulation results show that spacecraft charging is not severe under typical solar wind condition. However, a spacecraft is negatively charged up to $-1400V$ for severe magnetosheath charging condition. We also investigated the plasma interactions of a multibody system consisting of a large plate ($6\lambda_d \times 6\lambda_d$) and a small free flyer ($1.2\lambda_d \times 1.2\lambda_d \times 0.6\lambda_d$) in the absence of photoelectron emissions. In this dissertation, we set a free flyer at $2\lambda_d$ behind the large platform on the central axis in the wake. In our simulation cases, the free flyer is sufficiently far away form the platform where ion currents can be refilled and cancel electron currents. The simulation results under both the mean solar wind condition and severe magnetosheath charging condition show that wake charging for our simulation case is not severe. As a results, the free flyer potentials are about $\sim -1.5T_e$ under the mean solar wind condition and about $\sim -1.95T_e$ under severe magnetosheath charging condition.

5.2 Suggestions for Future Work

Realistic Spacecraft Configuration

The charging model presented here considered a relatively simple configuration. It is necessary to improve a charging model in order to account for a more realistic configuration and various surface materials. In order to carry out the simulations in realistic and complicated spacecraft geometry, it is critical to use a fine mesh around a spacecraft, thus suggesting the implementation of a stretched mesh method.

Another challenging work is to extend the charging model in order to account for the inhomogeneous surfaces such as a solar array. The solar array consists of a cluster of dielectric solar cells. Thus, the charging model should include the multi-material charging of both insulating and conducting materials. Additionally, the charging calculations should take into account the differential charging caused by the multi-material structure.

Parallel Computation

The dimensions of the capacitance matrix are $N_x \times N_x$ where N_x is the total grid number designated by a spacecraft. In order to carry out the simulation for the complicated and realistic spacecraft geometry, it is necessary to use a fine mesh around the desired spacecraft geometry, requiring a large amount of computer memory and computational time. These current limitations require parallelizing the charging model developed here.

Comparisons of Measurements

The results from the charging model developed here showed reasonable agreement with observation data ($\sim 5V$ to $10V$) for typical solar wind [75]. However, it is necessary to compare the numerical results under various solar wind conditions with measurements. Also, studies for detailed plasma dynamics and modification due to the sheath generated by spacecraft charging should be carried out and quantitatively compared with measurements. The sheath generated by spacecraft charging will modify ambient plasma incidence. For example, an ambient plasma detector on the charged spacecraft can not accurately measure due to modi-

fication by the sheath. Studies using full PIC simulations have been carried out to investigate the ambient plasma dynamics and reduce the surface potential by ejecting plasma from a satellite [85]. However, previous studies have been limited to a biased floating spacecraft potential, ignoring the time-dependant sheath effect and the floating potential self-consistently determined. Thus, the charging model can be applied to improve the limitations of the previous studies.

Wake Charging

In this dissertation, we only consider the waking charging effect in eclipse. However, the charging study should be performed in sunlight conditions. Also, in order to investigate comprehensively the wake charging, it is necessary to study the charging effect through different positions of a free flyer. Ion and electrons current will be changed along the distance from the front plate in the wake region. For instance, ion and electrons current will be reduced near the plate in the wake region, depending on the plasma temperature. Additionally, it is necessary to study the wake charging effect when a front plate and a small flyer are electrically connected. For instance, solar sail charging simplified as a thin plate showed that the charging effect is not severe. However, when we consider realistic solar sail configuration, it is significant to study the charging effect by the small body positioned in the wake region. Additionally, the charging effect for the small flyer attaching on the ram side will be studied.

Bibliography

[1] D. B. Beard and F. S. Johnson, Charge and magnetic field interaction with satellites, J. Geophys. Res.,65 1-7,1960.

[2] S. J. Beard, A program for the direct solution of Poisson's equation in complex gometries, Computer physics communications, 36, 25-57, 1985.

[3] I. B. Bernstein and Rabinowitz, Theory of electrostatic probes in a low-density plasma, Phys. Fluids, 2, 112-21,1959 .

[4] C. K. Birdsall, A. B. Langdon, Plasma physics via computer simulation, Hilger, New York, 1991.

[5] K. L. Cartwright, J. P. Verboncoeur, and C. K. Birdsall, Loading and injection of Maxwellian distributions in particle Simulations, Journal of Computational Physics 162, 483-513, 2000.

[6] W.Y. Chang, J.R. Dennison, Jason Kite and R.E. Davies, Effects of evloving surface contamination on spacecraft charging, AIAA conference, 2000.

[7] M. Cho, D. E. Hastings, Dielectric charging processes and arcing rates of high voltage solar arrays, Journal of Spacecraft and Rockets, Vol. 28, p.698, 1991.

[8] M. Cho, Arcing on high voltage solar arrays in low earth orbit: theory and computer simaultion, Ph.D dissertation, 1992.

[9] R. H.Comfort, T. E. Moore, P. D. Craven, C. J. Pollock, F. S. Mozer, W. S. Williamson, Spacecraft potential control by the plasma source instrument on the POLAR satellite, J. Spacecraft and Rockets, 35, 845, 1998.

[10] D. L. Cooke, Wake effects in spacecraft charging, space environment prevention of risks related to spacecraft charging, Cepadues Editions, Toulouse, France, pp 271-288, 1996.

[11] W. Daughton, J. Scudder, H. Karimabadi, Fully kinetic simualtions of undriven magnetic reconnection with open boundary conditions, Phys. Plasmas, Volume 13, Issue 7, pp. 072101-072101-15, 2006.

[12] A. H. Davis and Harris I., Rarefied Gas Dynanrics ed L Talbot (New York: Academic), pp691-9,1961.

[13] V. A. Davis, I. Katz, M. J. Mandell and B. M. Gardner, Spacecraft charging interactive handbook, 6th Spacecraft Charging Technology Conference, AFRL-VS-TR-20001578, 2000.

[14] V. A. Davis, M. J. Mandell, D. L. Cooke, and C. L. Enloe, High-voltage interactions in plasma wakes: Simulation and flight measurements from the Charge Hazards and Wake Studies (CHAWS) experiment, J. Geophys. Res., 104, A6, p. 12445,1999.

[15] S. E. Deforest, Spacecraft charging at synchronous orbit, J. Geophys. Res., vol. 77, no. 4, pp. 651.659, Feb. 1972.

[16] C. L. Enloe, D. L. Cooke, S.Meassick, C. Chan, and M. R. Tautz, Ion collection in a spacecraft wake: laboratory simulations, Journal of Geophysical Research, Vol. 98, No. 8, 1993, pp. 13635-13644.

[17] J. Forest, L. Eliasson, and A. Hilgers, A New spacecraft plasma simulation software, PicUp3D/Spis, 7th Spacecraft Charging and Technology Conference, p.515.520, ESA/SP-476, ESAESTEC, Noordwijk, The Netherlands, 23.27 April 2001.

[18] J. H. M. Fu, Surface potential of a photo emitting plate, J.Geophysical Res., 76, 2506-2509, 1971.

[19] H. E. Garrett, The charging of spacecraft surfaces, Reviews of Geophysics and Space Physics, 19, 577-616, 1981.

[20] H. Garret and A. Whittlesey., Spacecraft charging, an update. In AIAA- 96-0143, 1996.

[21] H. Garret., Future directions in spacecraft charging-2001 and beyond. In AIAA-2002-0624, 2002.

[22] H. Garrett and J. Wang, Simulations of solar wind plasma flow round a simple solar sail, Spacecraft Charging Technology Conference, Huntsville, AL, Oct. 2003.

[23] M. J. Geockner, J. Goree, and T. E. Sheridan, Measurments of ion velocity and denity in the plasma sheath, Phys. Fluids, pp. 1663-1670, 1992.

[24] J. Gosling, The Solar wind in encyclopedia of the solar system, Academic, San Deigo, 1999.

[25] R. J. L. Grard and J.K.E. Tunaley, Photoelectron sheath near a planar probe in interplanetary space, J. Geophysics. Res., 76, 2498-2505, 1971.

[26] R. J. L. Grard, Properties of the satellite photoelectron sheath derived from photoemission laboratory measurements, J. Geophysical Res., 78, 2885-2906, 1973.

[27] R. J. L. Grard, Photon and particle interactions with surfaces in space, D. Reidel, 1973.

[28] R. L. Guernsey and J. H. M. Fu, Potential distribution surrounging a photo-emitting plate in a dilute plasma, J.Geophysical Res., 75, 3193-3199, 1970.

[29] D. E. Hasting and H. Garrett, Spacecraft environment interaction. Cambridge, U.K.: Cambridge Univ. Press, 1996.

[30] M. R. Hestenes, and E. Stiefel, Methods of conjugate gradients for solving linear systems, J. Res. of the national bureau of standards, 49, 409, 1952.

[31] R. W. Hockney and J. W. Eastwood, Computer simulation using particles, McGraw-Hill, U.S.A., 1981.

[32] R. W. Hockney, POT4- a FACR algorithm atbitrary regions, computers fast ecllips solvers and application, Advance publications Ltd, London, pp. 141-169, 1978.

[33] A. Hilgers, J. Forest, and J. F. Roussel. (2002, Dec). SPIS, the spacecraft plasma interaction system. [Online]. Available: http://dev.spis.org/ projects/spine/home/spis.

[34] A. Hilgers, B. Thiebault, J.-F. Roussel, J. Forest, and E. Engwall, Tests and validation of a new spacecraft plasma interaction software, SPIS, in Proc. 9th Spacecraft Charging Technol. Conf., Tsukuba, Japan, 2005.

[35] A. Hilger, Interaction bwtween biased sulit electron collectors in an infinite-Debye-length magnetoplasma: Electron temperature thredhold effect, J. Geophys. Res., 100, 5705-5713.

[36] S. Hosoda, T. Muranaka, H. Ueda, K. Koga, T. Goka, H. Kuninaka, S. Hatta, J. Kim, N. Kurahara, M. Cho, Laboratory experiments for code validation of multi-utility spacecraft charging analysis tool (MUSCAT), Proc. 10th Spacecraft Charging Technology Conference, Biarritz, France, June 2007.

[37] L. Jolivet, and J. F. Roussel, Numerical simulation of plasma sheath phenomenon in presence of secondary electronic emission, submitted to IEEE Transactions on Plasma Science, 2001.

[38] I. Katz, M. J. Mandell, G. Jongeward, and M. S. Gussenhoven, The importance of accurate secondary electron yields in modeling spacecraft charging, J. Geophys. Res., vol. 91, no. A12, pp. 13739.13744, Dec. 1986.

[39] I. Katz, D. E. Parks, D. L. Cooke, M. J. Mandell, and A. J. Rubin, Polar orbit electrostatic charging of objects in shuttle wake, Spacecraft Environmental Interactions Technology 1983, NASA Lewis Research Center, pp. 229-234, 1985.

[40] I. Katz, M. J. Mandell, J. G. A. Jongeward, J. R. Lilley, W. N. Hall, and A. G. Rubin, Astronaut charging in the wake of a polar orbiting shuttle, AIAA Paper 85-7035, Nov. 1985.

[41] I. Katz and V. A. Davis, Mechanism for Spacecraft charging initiated destruction of solar arrays in GEO, AIAA Paper 98-1002, AIAA Aerospace Sciences Meeting and Exhibit, 36th, Reno, NV, Jan. 2000.

[42] I. Katz, V. A. Davis, M. J. Mandell, B. M. Gardner, J. M. Hilton, J. Minor A. R. Fredrickson, and D. L. Cooke, Spacecraft charging interactive handbook with integrated, updated spacecraft charging models, Aerospace Sciences Meeting, AIAA Paper 2000-0247, AIAA Aerospace Sciences Meeting and Exhibit, 38th, Reno, NV, Jan. 2000.

[43] I. Katz, V. A. Davis, M. J. Mandell, D. E. Parks, B. M. Gardner, J. M. Hilton, J. Minor, and D. L. Cooke, An auroral charging model in the spacecraft charging interactive handbook, AIAA Paper 2001-0956, AIAA Aerospace Sciences Meeting and Exhibit, 39th, Reno, NV, Jan. 2001.

[44] H. Jeong and J. Wang, Full particle PIC simulations of solar sail charging and plasma interactions, 10th Spacecraft Charging Technology Conference, France, 2007.

[45] J. G. Laframboise, and J. Luo, High-voltage polar-orbit and beam- induced charging of a dielectric spacecraft: A wake-induced barrier effect mechanism, Journal of Geophysical Research, Vol. 94, No. 7, pp. 9033-9048, 1989.

[46] S. T. Lai, High-level spacecraft charging at geosynchronous altitudes: A statistical study, in Proc. 8th Spacecraft Charging Technology Conf., NASA/CP-2004-21309, 2003.

[47] S. T. Lai and M. Tautz, High-level spacecraft charging in eclipse at geosynchronous altitudes: A statistical study, J. Geophys. Res., vol. 111, no. A9, p. A09201, doi:10.1029/2004JA010733, 2005.

[48] J. R. Lilley, Jr., D.L. Cooke, GA. Jongeward, and I. Katz, POLAR User's Manual GL-TR-89-0307, Oct. 1989.

[49] I. Langmuir and K. Blodgett, Currents limited by space charge between concentric spheres, Phys. Rev., vol. 24, no. 1, pp. 49.59, Jul. 1924.

[50] M. Leung and H. Kan. Laboratory study of the charging of spacecraft materials. Journal of Spacecraft and Rockets, 18, 1981.

[51] J. R. Lilley, D. L. Cooke, G. A. Jongeward, and Katz I, POLAR Users manual, Geophysics Laboratory, Hanscom, GL-TR-89-0307, October 1989.

[52] M. J. Mandell, I. Katz, and D. Cooke, Towards a more robust spacecraft charging algorithm, in Proc. 6th Spacecraft Charging Technol. Conf., pp. 251-255, 2000.

[53] M. J. Mandell et al. Nascap2k - spacecraft charging analysis code for the 21st century. In 39th Aerospace Sciences Meeting and Exhibit, AIAA 01.957, Reno, Nevada, January 2001.

[54] M. J. Mandell, I. Katz, J. M. Hilton, D. L. Cooke, and J. Minor, Nascap- 2K spacecraft charging models: Algorithms and applications, in Proc. 7th Spacecraft Charging Technol. Conf., pp. 23-27, 2001.

[55] M. J. Mandell et al. Modeling the charging of geosynchronous and interplanetary spacecraft using nascap-2k. Advances in Space Research, 36, 2005.

[56] M. J. Mandell , G. A. Jongeward, and D. L. Cooke, Spacecraft-plasma interaction codes: NASCAP/GEO, NASCAP/LEO, POLAR, DynaPAC, and EPSAT, Fifth Annual Workshop on Space Operations Applications and Research, Houston, Texas, July 9-11, pp 672-679, 1991.

[57] C. Marrese, J. Wang, K. Goodfellow, and A. Gallimore, 2000. Chapter 18: Space-charge limited emission from field emission array cathodes for electric propulsion and tether applications, micropropulsion for small spacecraft, progress in Aeronautics and Astronautics, V187, pp423-447, America Institute of Aeronautics and Astronautics. (M. Micci and A. Ketsdever eds.)

[58] D. A. McPherson, and W. R. Schober, Spacecraft charging in high altitude: The SCATHA satellite program, in Spacecraft Charging by Magnetospheric Plasmas, Prog, Astronaut. Aeronaut., vol. 47, pp.15-30, MIT Press, Cambridge, Mass, 1976.

[59] H. M. Mott-Smith and I. Langmuir, The theory of collectors in gaseous discharges, Phys. Rev., vol. 28, no. 4, pp. 727.763, Oct. 1926.

[60] T. Muranaka, S. Hosoda, S. Hatta, J. Kim, K. Ikeda, M. Cho, H. Ueda, K. Koga, T. Goka, Final version of Multi-Utility Spacecraft Charging Analysis Tool (MUSCAT), Proc. 10th Spacecraft Charging Technology Conference, Biarritz, France, June 2007.

[61] M. J. Mandell, and I. Katz, High voltage plasma interactions calculations using NASCAP/LEO, AIAA Paper AIAA-90-0725, 1990.

[62] M. J. Mandell, P. R. Stannard, and I. Katz, NASCAP programmer's reference manual, NASACR 191044, 1993.

[63] M. J. Mandell, T. Luu, J. Lilley, G Jongeward, and I. Katz, Analysis of dynamical plasma interactions with high voltage spacecraft, (2 volumes), Rep. PL-TR-92- 2258, Phillips Lab., Hanscom Air Force Base, MA, June 1992.

[64] M. J. Mandell, D. L. Cook, V. A. Davis, G Jongeward, B. M. Gardner, R. A. Hilmer, K.P. Ray, S. T. Lai, L. H. Krause, Modeling the charging of geosychronous and inter-planetary spacecraft using Nascap-2k, Advnaces in space research, 36, 2511-2515, 2005.

[65] A. R. Martin, A review of spacecraft/plasma interactions and effects on space systems, J. Br. Interplanet. Soc., vol. 47, no. 4, pp. 134.142, Apr. 1994.

[66] R. L. Morse, Multidimensional plasma simulations by particle-in-cell methods, in Computational Physics, edited by B. Alder, S. Fernbach and M. Rotenberg, pp. 213-239, Academic, San Diego, Calif., 1970.

[67] E. G. Mullen, M. S. Gussenhoven, D. A. Hardy, T. L. Aggson, B. G. Ledley, and E. Whipple, SCATHA survey of high-level spacecraft charging in sunlight J. Geophys. Res., vol. 91, no. A2, pp. 1474.1490, 1986.

[68] NASA, Charged particle effects on solar sails (Final Report), NASA Marshall Space Flight Center, ISPT-SS-06-101, 2006.

[69] T. Nitter, O. Havnes, and F. Melandso, Levitation and dynamics of charged dust in the photoelectron sheath above surfaces in space, J. Geophysical Res., 103, 6605-6620, 1998.

[70] R. C. Oslen, Modification of spacecraft potentials by plasma emission, Journal of Spacecraft and Rockets, vol.18, no.5, p.462-469, 1981

[71] L. W. Parker, and B. L. Murphy, Potential buildup on an electron emitting ionospheric satellite, Journal of Geophysical Research, Vol. 72, No 5, pp. 1631-1636, 1967.

[72] L. W. Parker, and E. C. Sullivan, Iterative methods for plasma-sheath calculations - application to spherical probe, Goddard Space Flight Center, MD, NASA TN D-7409, March 1974.

[73] L. W. Parker, Calculation of sheath and wake structure about a pillbox-shaped spacecraft in a flowing plasma, Proceedings of the Spacecraft Charging Technology Conference, AFGL-TR-77-0051, NASA TMX-73537, 1977.

[74] A. Pedersen, C. R. Chapell, K. Knott, and R. C. lsen, Methods for keeping a conductive spacecraft near the plasma potential, in spacecraft plasma interactions and their influence on field and particle measurements, Proceedings of the 17th ESLAB Symposium, ESA SP-198, p. 185, 1983.

[75] A. Pedersen, Solar wind and magnetosphere plasma diagnostics by spacecraft electrostatic potential measurements, Ann. Geophys., 13, 118, 1995.

[76] P.A. Robinson, Spacececraft charging: progress in the study of dielectrics and plasma, IEEE transactions on electrical insulation.

[77] A. Rosen., et al., GRA analysis; findings regarding correlation of satellite anomalies with magnetospheric substorms and laboratory test results, TRW System Group, Calif. 1972.

[78] J. F. Roussel, and J. J. Berthelier, Numerical simulation of the electrical charging of the ROSETTA orbiter, 7th Spacecraft Charging Technology Conference, Noordwijk, The Netherlands, April 23-27, 2001.

[79] J.F. Roussel, F. Rogier, D. Volpert, G. Rousseau, J. Forest, and A. Hilgers, Spacecraft plasma interaction software (SPIS): Numerical solvers.Methods and architecture, in Proc. 9th Spacecraft Charging Technol. Conf., 2005, Tsukuba, Japan.

[80] H. Schroder, Spherically symmetric model of the photoelectron sheath for moderately large plasma Debye lengths, Photon and particle interactions with surfaces in space, pp.51-58, 1973.

[81] N. Singh, and R. W. Schunk, Numerical calculations relevant to the initial expansion of the polar wind, J. Geophys. Res. 87, 9154, 1982.

[82] K. F. Stephens II, and C. A. Ordonez, Sheath and presheath potentials for anode, cathode and floating plasma-facing surfaces, J. Appl. Phys., Vol. 85, No 5, pp. 2522-2527, 1999.

[83] R. R. Shaw, J.E Nanevicz, and R. C. Adamo, Observations of electral discharges caused by differential satellite charging, in spacecraft charging by magnetospheric plasmas, Prog, Astronaut. Aeronaut. vol. 47, pp. 61-76, AIAA press, New York, 1976.

[84] S. F. Singer and E. H. Walker, Photoelectric screening of bodies in interplanetary space, Icarus, 1, 7-12, 1962a.

[85] N. Singh and W. C. Leung, Numerical model of the plasma sheath generated by the plasma source instrument abroad the polar satellite, J.Geophysical Res., 106, 19,179-19,192, 2001.

[86] B. Thiebault, A. Hilgers, E. Sasot, H. Laakso, P. Escoubet, V. Genot, and J. Forest, Potential barrier in the electrostatic sheath around a magnetospheric spacecraft, J. Geophys. Res., accepted, 2004.

[87] J. Troim, and B. N. Maehlum, Laboratory simulation studies on charging of spacecraft, Physics of Charged Bodies in Space Plasmas, edited by M. Dobrowolny and E. Sindoni, Varenna, Italy, pp. 305-313, 1991.

[88] H. Usui, Y. Miyake, M. Okada, Y. Omura, T. Sugiyama, K. T. Murata, D. Matsuoka, H. O. Ueda, Developement and application of geospace environment simulator for the anlysis of spacecraft-plasma interactions, IEEE Transactions on plasma science, Vol.34, no.5, pp 2094.2102, 2006.

[89] J. Wang and D.E. Hastings, Ionospheric plasma flow Over large high voltage space platforms I: Ion-plasma time Scale interactions on a plate at zero angle of attack, Phys. Fluids B, 4(6), 1597-1614, 1992a.

[90] J. Wang and D.E. Hastings, Ionospheric plasma flow over large high voltage space platforms II: the formation and structure of the plasma wake, Phys. Fluids B, 4(6), 1615- 1629, 1992b.

[91] J. Wang, and S. Lai, Virtual anodes in ion beam emissions in space: numerical simulations, J. Spacecraft Rockets, 34 (6), 829-836, 1997.

[92] J. Wang, D. Brinza, and M. Young, Three-dimensional particle simulations of ion propulsion plasma environment for deep space 1, J. Spacecraft Rockets, 38 (3), 433-440, 2001.

[93] J. Wang., P. Leung, H. Garret., and G. Murphy, Multibody-plasma interactions: charging in the wake, Journal of Spacecraft and Rockets (ISSN 0022-4650), vol. 31, no. 5, p. 889-894, 1994.

[94] E. C. Whipple, Obsevation of photoelectron and secondary electrons reflected from a potential barrier in the vicinity of ATS6, J. Geophysical Res., 81, 715-719, 1976.

[95] E. C. Whipple, Potentials of surfaces in space, Reports on Progress in Physics, 44:1197 -1250, 1981.

[96] E. C. Whipple Jr., Theory of the spherically symmetric photoelectron sheath . A thick sheath approximation and comparison with the ATS 6 observation of a potential barrier, J. Geophys. Res., 81, 4, 601, 1976.

[97] E. C. Whipple Jr., Modeling of spacecraft charging, In NASA. Lewis Res. Center Proc. of the Spacecraft Charging Technol. Conf. pp 225-235, 1977.

[98] H. Zhao, R. Schmit, and C. P. Escoubet, Self-consistent determination of the electrostatic potential barrier due to the photoelectron sheath near a spacecraft, J.Geophysical Res., 101, 15,653-15,659, 1996.

Appendix A

Sheath Theory for Stationary Maxwellian Electrons

A.1 Non-monotonic Sheath Profile: Type A

The theoretical model reviewed here follows the method suggested by Fu [28], [18] and extended by Nitter et al. [69]. The calculation was carried out for a large planar object. In this theory, two assumptions are applied: ambient plasma consists of cold and drifting ions and stationary Maxwellian electrons. When photoelectrons dominate, there can exist two types steady state solution of the potential profile in the photoelectron sheath, the monotonic profile and non-monotonic profile and the non-monotonic profile is a more stable solution [18]. Ion velocity can be obtained using energy conservation:

$$\frac{1}{2}mv_{\infty}^2 = \frac{1}{2}mv_i^2(x) - e\phi(x) \tag{A.1}$$

$$v_i(x) = \sqrt{v_{\infty}^2 - \frac{2e\phi(x)}{m}} \tag{A.2}$$

Then ion density can be obtained by a continuity equation:

$$n_i(x) = n_\infty \frac{v_\infty}{v_i(x)} = n_\infty (1 - \frac{2e\phi(x)}{v_\infty^2 m})^{-\frac{1}{2}} \tag{A.3}$$

$$f_j(x,v) = n_j (\frac{m}{2\pi k T_j})^{3/2} \exp(-\frac{m(v_x^2+v_y^2+v_z^2)}{2kT_j} + \frac{e(\phi(x)-\phi_j)}{kT_j}) \tag{A.4}$$

where $\phi_e = \phi_\infty$ corresponds to the potential at infinity for plasma electrons $j = e$ and $\phi_p = \phi_0$ is the surface floating potential of objects for photoelectrons $j = p$.

The density distribution of ambient electrons and photoelectrons can be obtained as

$$\begin{aligned} n_{j,f}(x) &= \int_{-\infty}^{\infty}\int_{-\infty}^{\infty}\int_{v_m}^{\infty} f_j(v) d^3v = \frac{n_j}{2}\exp(\frac{e(\phi(x)-\phi_j)}{kT_j})(1 - erf(\frac{v_m(x)}{v_t})) \\ &= \frac{n_j}{2}\exp(\frac{e(\phi(x)-\phi_j)}{kT_j})(1 - erf\sqrt{\frac{e(\phi(x)-\phi_m)}{kT_j}}) \end{aligned} \tag{A.5}$$

$$\begin{aligned} n_{j,c}(x) &= 2\int_{-\infty}^{\infty}\int_{-\infty}^{\infty}\int_{0}^{v_m} f_j(v) d^3v = n_j \exp(\frac{e(\phi(x)-\phi_j)}{kT_j})(erf(\frac{v_m(x)}{v_t})) \\ &= n_j \exp(\frac{e(\phi(x)-\phi_j)}{kT_j})(erf\sqrt{\frac{e(\phi(x)-\phi_m)}{kT_j}}) \end{aligned} \tag{A.6}$$

In this equation, $v_t = \frac{2m_e}{kT_j}$ and $v_m(x) = \sqrt{\frac{2e(\phi(x)-\phi_m)}{m_e}}$ are the thermal velocity and the minimum speed, respectively. When $x \leq x_m$, the reflected electrons $n_{e,r}$ does not exist because the low energy ambient electrons return by a potential barrier. Similarly, the photoelectrons relatively lower energy than minimum potential can not overcome the potential barrier. Therefore, captured photoelectrons are zero at $x \geq x_m$.

The Poisson's equation can be written as

$$\frac{d^2\phi}{dx^2} = -\frac{e}{\varepsilon_0}(n_i - n_{e,f} - n_{e,r} - n_{p,f} - n_{p,c}) \tag{A.7}$$

The Poisson's equation can be simplified by using mathematical technique as follows:

$$\frac{d}{dx}(\frac{d\hat{\phi}}{d\hat{x}})^2 = 2(\frac{d\hat{\phi}}{d\hat{x}})\frac{d^2\hat{\phi}}{d\hat{x}^2} \tag{A.8}$$

The electric field can be obtained by integrating (A.8) from $\phi = \hat{\phi_m}$ to $\hat{\phi_x}$. The equation can be written as

$$(\frac{d\hat{\phi}}{d\hat{x}})^2 = 2\int_{\hat{\phi_m}}^{\hat{\phi_x}}(\hat{n}_{e,f} + \hat{n}_{e,r} + \hat{n}_{p,f} + \hat{n}_{p,c} - \hat{n}_i)d\hat{\phi} \tag{A.9}$$

The electric field for electrons can be obtained as

$$\begin{aligned} E_{e,f} &= 2\int_{\hat{\phi_m}}^{\hat{\phi_x}} \hat{n}_{e,f}d\hat{\phi} = 2\int_{\hat{\phi_m}}^{\hat{\phi_x}} \frac{\hat{n}_{e,\infty}}{2}\exp(\frac{\hat{\phi}-\hat{\phi_\infty}}{\beta})[1 - erf(\sqrt{\frac{\hat{\phi}-\hat{\phi_m}}{\beta}})]d\hat{\phi} \qquad (A.10)\\ &= \hat{n}_{e,\infty}\beta\{\exp(\frac{\hat{\phi_x}-\hat{\phi_\infty}}{\beta})[1 - erf(\sqrt{\frac{\hat{\phi_x}-\hat{\phi_m}}{\beta}})] + \exp(\frac{\hat{\phi_m}-\hat{\phi_\infty}}{\beta})[\frac{2}{\sqrt{\pi}}\sqrt{\frac{\hat{\phi_x}-\hat{\phi_m}}{\beta}} - 1]\}\\ E_{e,r} &= 2\int_{\hat{\phi_m}}^{\hat{\phi_x}} \hat{n}_{e,r}d\hat{\phi} = 2\int_{\hat{\phi_m}}^{\hat{\phi_x}} \hat{n}_{e,\infty}\exp(\frac{\hat{\phi}-\hat{\phi_\infty}}{\beta})erf(\sqrt{\frac{\hat{\phi}-\hat{\phi_m}}{\beta}})d\hat{\phi} \qquad (A.11)\\ &= 2\hat{n}_{e,\infty}\beta\{\exp(\frac{\hat{\phi_x}-\hat{\phi_\infty}}{\beta})erf(\sqrt{\frac{\hat{\phi_x}-\hat{\phi_m}}{\beta}}) - \frac{2}{\sqrt{\pi}}\exp(\frac{\hat{\phi_m}-\hat{\phi_\infty}}{\beta})\sqrt{\frac{\hat{\phi_x}-\hat{\phi_m}}{\beta}}\} \end{aligned}$$

where $\hat{\phi_\infty} = 0$ at infinity.

The electric field for photoelectrons is

$$E_{p,f} = 2\int_{\hat{\phi_m}}^{\hat{\phi_x}} \hat{n}_{p,f}d\hat{\phi} = 2\int_{\hat{\phi_m}}^{\hat{\phi_x}} \frac{\hat{n}_{p,0}}{2}\exp(\hat{\phi}-\hat{\phi_m})[1 - erf(\sqrt{\hat{\phi}-\hat{\phi_m}})]d\hat{\phi} \tag{A.12}$$

$$
\begin{aligned}
&= \hat{n}_{p,0}\{\exp(\hat{\phi_x}-\hat{\phi_m})[1-erf(\sqrt{\hat{\phi_x}-\hat{\phi_m}})]+\exp(\hat{\phi_m}-\hat{\phi_m})[\frac{2}{\sqrt{\pi}}\sqrt{\hat{\phi_x}-\hat{\phi_m}}-1]\} \\
E_{p,c} &= 2\int_{\hat{\phi_m}}^{\hat{\phi_x}} \hat{n}_{p,c}d\hat{\phi} = 2\int_{\hat{\phi_m}}^{\hat{\phi_x}} \hat{n}_{p,0}\exp(\hat{\phi}-\hat{\phi_m})erf(\sqrt{\hat{\phi}-\hat{\phi_m}})d\hat{\phi} \qquad \text{(A.13)} \\
&= 2\hat{n}_{p,0}\{\exp(\hat{\phi_x}-\hat{\phi_m})erf(\sqrt{\hat{\phi_x}-\hat{\phi_m}})-\frac{2}{\sqrt{\pi}}\exp(\hat{\phi_m}-\hat{\phi_m})\sqrt{\hat{\phi_x}-\hat{\phi_m}}\}
\end{aligned}
$$

The electric field for ions is

$$E_i = -2\int_{\hat{\phi_m}}^{\hat{\phi_x}} n_i d\hat{\phi} = \frac{2\hat{n}_{i,\infty}}{n}\beta M^2[\sqrt{1-\frac{2\hat{\phi_x}}{\beta M^2}}-\sqrt{1-\frac{2\hat{\phi_m}}{\beta M^2}}] \qquad \text{(A.14)}$$

Then, the equation can be written as

$$\frac{d\hat{\phi}}{d\hat{x}} = \sqrt{E_{e,f}+E_{e,r}+E_{p,f}+E_{p,c}+E_i} = \sqrt{E_{tot}(\hat{\phi})} \qquad \text{(A.15)}$$

The non-monotonic sheath profile can be found by integrating from $\hat{\phi_0}$ to an arbitrary $\hat{\phi_x}$ when $\hat{x} \leq \hat{x_m}$. It is written by

$$\hat{x} = \int_{\hat{\phi_x}}^{\hat{\phi_0}} \frac{1}{\sqrt{E_{tot}(\hat{\phi})}}d\hat{\phi} \qquad \hat{x} \leq \hat{x_m} \qquad \text{(A.16)}$$

where $\hat{\phi_0} < \hat{\phi_x} \leq \hat{\phi_m}$

When $\hat{x} > \hat{x_m}$, the sheath profile can be obtained by

$$\hat{x} = \int_{\hat{\phi_x}}^{\hat{\phi_\infty}} \frac{1}{\sqrt{E_{tot}(\hat{\phi})}}d\hat{\phi} \qquad \hat{x} > \hat{x_m} \qquad \text{(A.17)}$$

where $\hat{\phi_m} < \hat{\phi_x} \leq \hat{\phi_\infty}$

The distance for minimum potential can be obtained by

$$\hat{x_m} = \int_0^{\hat{x_m}} d\hat{x} = \int_0^{\hat{x_m}} \frac{d\hat{x}}{d\hat{\phi}} \frac{d\hat{\phi}}{d\hat{x}} d\hat{x} = \int_{\hat{\phi_m}}^{\hat{\phi_0}} \frac{1}{\sqrt{E_{tot}(\hat{\phi})}} d\hat{\phi} \tag{A.18}$$

In order to determine ϕ_m, ϕ_0, and n_e, three conditions are imposed: 1) neutrality condition at infinity, 2) no electric field at infinity, and 3) zero total current at steady state. The neutrality condition at infinity can be obtained by equations (A.5) and (A.6):

$$\begin{aligned} n_e(\infty) + n_p(\infty) - n_i(\infty) = n_{e,f}(\infty) + n_{e,r}(\infty) + n_{p,f}(\infty) - n_i(\infty) \\ = \frac{n_{e,\infty}}{2}(1 + erf\sqrt{-\frac{\hat{\phi_m}}{\beta}}) + \frac{n_{p,0}}{2}\exp(-\hat{\phi_0})(1 - erf\sqrt{-\hat{\phi_m}}) - n_{i,\infty} = 0 \end{aligned} \tag{A.19}$$

It is assumed that the total current is zero at steady state where the captured photoelectrons and the reflected electrons do not contribute to the total current. The condition can be written as

$$\begin{aligned} J_{e,f}(\infty) + J_{p,f}(0) - J_i(\infty) = \int_{-\infty}^{\infty}\int_{-\infty}^{\infty}\int_{v_m(0)}^{\infty} v_x f_p(0,v) dv_x dv_y dv_z \\ + \int_{-\infty}^{\infty}\int_{-\infty}^{\infty}\int_{-\infty}^{-v_m(\infty)} v_x f_e(\infty,v) dv_x dv_y dv_z + n_i(\infty) v_i(\infty) = 0 \end{aligned} \tag{A.20}$$

where $v_m(x) = \sqrt{\frac{2e(\phi(x)-\phi_m)}{m_e}}$ is the minimum velocity.

Then it can be simplified by integration as follows:

$$n_{p,0}\exp(\hat{\phi_m} - \hat{\phi_0}) - n_{e,\infty}\sqrt{\beta}\exp(\frac{\hat{\phi_m}}{\beta}) + n_{i,\infty}\sqrt{2\pi\beta m_e/m_i}M = 0 \tag{A.21}$$

The total electric field is zero at infinity where the captured photoelectrons do not contribute:

$$E(\infty) = E_{e,f}(\infty) + E_{e,r}(\infty) + E_{p,f}(\infty) + E_i(\infty) = 0 \tag{A.22}$$

It can be simplified as

$$\begin{aligned} & n_{e,\infty}\beta[1 + erf(\sqrt{-\frac{\hat{\phi_m}}{\beta}}) - \exp(\frac{\hat{\phi_m}}{\beta})(1 + \frac{2}{\sqrt{\pi}}\sqrt{-\frac{\hat{\phi_m}}{\beta}})] \\ + \quad & n_{p,0}\exp(-\hat{\phi_0})[1 - erf(\sqrt{-\hat{\phi_m}})] + \exp(\hat{\phi_m} - \hat{\phi_0})[\frac{2}{\sqrt{\pi}}\sqrt{-\hat{\phi_m}} - 1] \\ + \quad & 2n_{i,\infty}\beta M^2(1 - \sqrt{1 - \frac{2\hat{\phi_x}}{\beta M^2}}) = 0 \end{aligned} \tag{A.23}$$

A.2 Monotonic Sheath Profile: Type B

In this section, type B potential profile is introduced. The sheath profile does not contain captured electrons in the calculation. The resulting the Poisson's equation can be written as

$$\frac{d^2\phi}{dx^2} = -\frac{e}{\varepsilon_0}(n_i - n_{e,f} - n_{p,f} - n_{p,c}) \tag{A.24}$$

Then, the Poisson's equation can be normalized as

$$(\frac{d\hat{\phi}}{d\hat{x}})^2 = 2\int_{\hat{\phi_m}}^{\hat{\phi_x}} (\hat{n}_{e,f} + \hat{n}_{e,r} + \hat{n}_{p,f} + \hat{n}_{p,c} - \hat{n}_i) d\hat{\phi} \tag{A.25}$$

The electric field for each species can be calculated with equations (A.10)-(A.14). In type B, the minimum potential $\hat{\phi_m}$ is zero. The monotonic sheath profile of positive surface potential can be obtained by integrating from $\hat{\phi_0}$ to an arbitrary $\hat{\phi_x}$ as follows:

$$\hat{x} = \int_{\hat{\phi}_x}^{\hat{\phi}_0} \frac{1}{\sqrt{E_{tot}(\hat{\phi})}} d\hat{\phi} \tag{A.26}$$

where $\hat{\phi}_0 < \hat{\phi}_x \leq \hat{\phi_\infty}$.

The unknown variables of $\hat{\phi}_0$ and n_e are simply obtained by two conditions: neutrality at infinity and zero total current at steady state.

Neutrality at infinity is expressed as

$$\begin{aligned} n_e(\infty) + n_p(\infty) - n_i(\infty) &= n_{e,f}(\infty) + n_{p,f}(\infty) - n_i(\infty) \\ &= \frac{n_{e,\infty}}{2} + \frac{n_{p,0}}{2} \exp(-\hat{\phi}_0) - n_{i,\infty} = 0 \end{aligned} \tag{A.27}$$

The zero total current at steady state can be obtained as follows:

$$n_{p,0} \exp(-\hat{\phi}_0) - n_{e,\infty}\sqrt{\beta} + n_{i,\infty}\sqrt{2\pi\beta m_e/m_i} M = 0 \tag{A.28}$$

A.3 Monotonic Sheath Profile: Type C

In this dissertation, the sheath profile of negative surface potential and increasing monotonically to infinity is defined as Type C. There are no captured photoelectrons in the type C sheath profile and $\hat{\phi_m} = \hat{\phi}_0$. To obtain the function of the potential distribution, the electric field is found by integrating the Poisson's equation from $\hat{\phi}_0 = 0$ to an arbitrary $\hat{\phi}_x$:

$$E_{e,f} = 2\int_0^{\hat{\phi}_x} \hat{n}_{e,f} d\hat{\phi} = 2\int_0^{\hat{\phi}_x} \frac{\hat{n}_{e,\infty}}{2} \exp(\frac{\hat{\phi} - \hat{\phi_\infty}}{\beta})[1 - erf(\sqrt{\frac{\hat{\phi} - \hat{\phi}_0}{\beta}})] d\hat{\phi} \tag{A.29}$$

$$= \hat{n}_{e,\infty}\beta\{\exp(\frac{\hat{\phi}_x}{\beta})[erfc(\sqrt{\frac{\hat{\phi}_x-\hat{\phi}_0}{\beta}})] - erfc(\sqrt{\frac{-\hat{\phi}_0}{\beta}}) + \frac{2}{\sqrt{\pi}}\exp(\frac{\hat{\phi}_0}{\beta})[\sqrt{\frac{\hat{\phi}_x-\hat{\phi}_0}{\beta}} - \sqrt{\frac{-\hat{\phi}_0}{\beta}}]\}$$

$$E_{e,r} = 2\int_0^{\hat{\phi_x}} \hat{n}_{e,r}d\hat{\phi} = 2\int_0^{\hat{\phi_x}} \hat{n}_{e,\infty}\exp(\frac{\hat{\phi}-\hat{\phi_\infty}}{\beta})erf(\sqrt{\frac{\hat{\phi}-\hat{\phi}_0}{\beta}})d\hat{\phi} \quad (A.30)$$

$$= 2\hat{n}_{e,\infty}\beta\{\exp(\frac{\hat{\phi}_x}{\beta})[erf(\sqrt{\frac{\hat{\phi}_x-\hat{\phi}_0}{\beta}})] - erf(\sqrt{\frac{-\hat{\phi}_0}{\beta}}) - \frac{2}{\sqrt{\pi}}\exp(\frac{\hat{\phi}_0}{\beta})[\sqrt{\frac{\hat{\phi}_x-\hat{\phi}_0}{\beta}} - \sqrt{\frac{-\hat{\phi}_0}{\beta}}]\}$$

$$E_{p,f} = 2\int_0^{\hat{\phi_x}} \hat{n}_{p,f}d\hat{\phi} = 2\int_0^{\hat{\phi_x}} \frac{\hat{n}_{p,0}}{2}\exp(\hat{\phi}-\hat{\phi_m})[1-erf(\sqrt{\hat{\phi}-\hat{\phi_m}})]d\hat{\phi} \quad (A.31)$$

$$= \hat{n}_{p,0}\exp(-\hat{\phi_m})\{\exp(\hat{\phi_x})[erfc(\sqrt{\hat{\phi}_x-\hat{\phi}_0})] - erfc(\sqrt{-\hat{\phi}_0}) + \frac{2}{\sqrt{\pi}}\exp(\hat{\phi}_0)[\sqrt{\hat{\phi}_x-\hat{\phi}_0} - \sqrt{-\hat{\phi}_0}]\}$$

$$E_i = -2\int_0^{\hat{\phi_x}} \hat{n}_i d\hat{\phi} = 2\hat{n}_{i,\infty}\beta M^2[\sqrt{1-\frac{2\hat{\phi_x}}{\beta M^2}} - 1] \quad (A.32)$$

Then, the sheath profile can be obtained by

$$\hat{x} = \int_{\hat{\phi_x}}^{\hat{\phi_\infty}} \frac{1}{\sqrt{E_{tot}(\hat{\phi})}}d\hat{\phi} \quad (A.33)$$

where $\hat{\phi}_0 < \hat{\phi_x} \leq \hat{\phi_\infty}$.

In the same way, the unknown variables of $\hat{\phi}_0$ and n_e are simply calculated by two conditions: neutrality at infinity and zero total current at steady state. The neutrality condition at infinity can be obtained by equations (A.5) and (A.6):

$$n_{e,f}(\infty) + n_{e,r}(\infty) + n_{p,f}(\infty) - n_i(\infty)$$

$$= \frac{n_{e,\infty}}{2}(1+erf\sqrt{-\frac{\hat{\phi_0}}{\beta}}) + \frac{n_{p,0}}{2}\exp(-\hat{\phi}_0)(1-erf\sqrt{-\hat{\phi}_0}) - n_{i,\infty} = 0 \quad (A.34)$$

The zero total current at steady state can be determined as follows:

$$n_{p,0} - n_{e,\infty}\sqrt{\beta}\exp(\frac{\hat{\phi}_0}{\beta}) + n_{i,\infty}\sqrt{2\pi\beta m_e/m_i}M = 0 \quad (A.35)$$